EUMETSAT ECMWF

EUMETSAT/ECMWF Fellowship Programme
Research Report

RR64

Improving Ocean Surface Temperature for NWP using All-Sky Microwave Imager Observations

Tracy Scanlon, Alan Geer, Niels Bormann, Philip Browne

August 2024

Contents

Executive Summary

In this report, we demonstrate the utility of information from low frequency Microwave (MW) channels for improving ocean surface temperature in a Numerical Weather Prediction (NWP) system. This is not only important for current instruments, but will also enhance the exploitation of upcoming sensors such as the Copernicus Imaging Microwave Radiometer (CIMR) from the European Space Agency (ESA) and the Microwave Imager / Ice Cloud Imager (MWI/ICI) from the European Organisation for the Exploitation of Meteorological Satellites (EUMETSAT).

Knowledge of the ocean surface Skin Temperature (SKT) is vital to the accurate use of satellite radiances in weather forecasting and it helps improve the quality of forecasts for the ocean and atmosphere. A primary source of the SKT information in this context is externally generated retrievals from satellite radiances. As we move to a full Earth system approach, the aim is to retrieve SKT and other surface information as an integrated part of the use of satellite radiances within the NWP system.

In the European Centre for Medium Range Weather Forecasts (ECMWF) Integrated Forecast System (IFS), the SKT used for assimilating satellite radiances is currently derived using an input Sea Surface Temperature (SST) from a combination of external sources. A cool skin and warm layer parameterization is then applied to transform this into a SKT valid at the time of the observation. However, the use of external SST products brings issues such as a complex and non-optimal use of the satellite radiances, and latency of up to 69 hours between the validity time of the SST observations and the time of its use in weather forecasting. This further motivates the direct retrieval of SKT within weather forecasting.

In the current work, a sink variable approach has been activated to allow the ocean SKT to update as part of the 4D variational assimilation (4D-Var). This method has been implemented for two MW imagers assimilated under all-sky conditions: Advanced Microwave Scanning Radiometer 2 (AMSR2) and the Global Precipitation Mission (GPM) Microwave Imager (GMI) which have been chosen as they include 6.9v/h and/or 10.65v/h GHz channels. These channels have much stronger sensitivity to SKT than the higher frequency MW channels currently being assimilated, and much greater coverage than IR channels, which can be strongly affected by cloud. The 6.9v/h and 10.65v/h GHz channels are being used for the first time over open ocean and the work is intended for operational use in cycle 50r1 of the ECMWF-IFS.

A series of new Quality Control (QC) methods have been implemented to allow the use of the 6.9v/h and 10.65v/h GHz channels: frequency dependent coastline screening, sun-glint screening and reflected Radio Frequency Interference (RFI) detection and screening from geostationary satellite sources. The inclusion of these channels has an overall neutral impact on the atmospheric forecast scores and associated departure statistics. However, there are slight improvements in the upper tropospheric humidity seen in both the forecast scores and independent observations (including IR) likely due to the improved representation of heavy rainfall.

The increments in SKT generated by the new approach indicate errors in the existing SKT, which is used as the background. These increments illustrate known deficiencies in the input data sources, for example, a large-scale cooling of Tropical Instability Waves (TIWs) in the Eastern Tropical Pacific (ETP) confirms a warm bias in this area in the existing SKT. The increments are generally larger and more wide spread during the day-time indicating a potential error either in the input SST used to grow the diurnal cycle, the SKT parameterization or both. The improved handling of the surface contribution to the microwave radiances also helps the atmosphere, for example some improvements in the vector winds, although overall the impact is small.

The next step in this work is to include the SKT increments into the coupled atmosphere-ocean system to improve the representation of the ocean surface in the ocean model and hence improve ocean and

atmosphere forecasts directly through the new SKT information. This approach also shares the SKT information derived from the low frequency MW across the data assimilation system so that it can improve the use of all observations with sensitivity to the surface including both MW and IR (e.g. AMSU-A, IASI, etc.). The use of the coupled system for MW SKT retrievals is a pathfinder for a fully integrated processing of SKT information from all satellite radiances from both current and future sensors.

Plain Language Summary

Accurate knowledge of the Sea Surface Temperature (SST) is an important part of weather forecasting as the ocean plays a key role in atmospheric processes as well as being important in the use of surface-sensitive satellite radiances. Currently, external data products are ingested at ECMWF for the SST but this can be many hours out of date at the time at which it is used. This work explores a method to allow the top-most layer of the ocean (the skin temperature) to vary along with the atmospheric variables in the data assimilation process for two microwave instruments. The instruments chosen have low frequency channels which allow for information about the surface to be exploited. The resultant increments made to the skin temperature show characteristics consistent with known issues in the external data products and are geophysically meaningful. Therefore, this method, including the activation of the low frequency channels, is intended to be included at the next upgrade to the ECMWF Integrated Forecast System.

1   Introduction

Knowledge of the ocean Skin Temperature (SKT) is vital for accurately simulating Top-of-Atmosphere (TOA) Brightness Temperatures (TBs) in the microwave (MW) range. Within the European Centre for Medium Range Weather Forecasts (ECMWF) Integrated Forecast System (IFS), the Radiative Transfer for TOVS (RTTOV) code for the MW range (RTTOV-SCATT) uses the SKT, along with forecast model fields, as an input to generate simulated TBs against which the MW observations are compared as part of the Data Assimilation (DA).

The SKT used in the simulation of TBs is calculated using external Sea Surface Temperature (SST) products, where the SKT is the temperature of the upper most layer of the ocean (microns thick) and is subject to diurnal heating and cooling and the SST, sometimes called the foundation SST, is free from the effects of the diurnal cycle. The initial SST used within the ECMWF-IFS for the atmospheric DA system is provided by the Operational Sea Surface Temperature and Ice Analysis (OSTIA) and OCEAN5 products.

OSTIA, generated by the UK Met Office, uses the Nucleus for European Modelling of the Ocean (NEMO) variational data assimilation code (NEMOVAR) (Mogensen and Balmaseda, 2012) with satellite and in-situ measurements with the aim of representing the foundation SST (Donlon *et al.*, 2012; Good *et al.*, 2020). In practice, due to the varying characteristics of the input data, OSTIA represents a variable depth. It is used as the SST in the ECMWF-IFS in the extra-tropics (latitudes polewards of 25°). Prior to ingestion into the atmospheric DA, the OSTIA product is re-sampled to the model grid, quality checked for realistic values and, for those grid cells where sea-ice is present, adjusted between the freezing temperature of salt water and the maximum SST in that grid-box based on a weighting function dependent on the sea-ice concentration and pre-determined constants (ECMWF, 2021).

OCEAN5 (Zuo *et al.*, 2019), a reanalysis product provided by ECMWF, is used in the tropics (latitudes less than 20°) and it represents a depth of 0.5 m (i.e. the middle of the topmost of the 75 model layers). This SST is also considered a foundation temperature as it is free of the diurnal cycle. The SST in the intermediate latitudes (between 20° and 25°) is a weighted mix of both products (ECMWF, 2021; Browne *et al.*, 2019) to allow a smooth blending between the latitude bands.

The SKT, which evolves with every model time-step, is grown from these foundation SST products. To do this, two time-varying effects need to be taken into account: the cool skin effect and the warm layer (with the impact of salinity being considered within these), each described in ECMWF (2023a). The cool skin is an approx. 1 mm thick layer where the long wave radiation heat losses to the atmosphere are not compensated for by molecular heat transfer within the water. The warm layer is caused by solar radiation heating the first few meters of the ocean.

At the time that the SST on which the SKT is based is used in the TOA TB simulations, they can be up to 69 hours old due to an unavoidable combination of product latency, processing windows and the length of the DA window (Browne *et al.*, 2019). In addition to this latency, OSTIA also uses a persistence assumption which means that where no data is available to update the product, the value is based on the previous temporal SST value until such time that a new observation is available (Good *et al.*, 2020).

In addition to this latency of the SST product from which the diurnal cycle is grown, there are a few other factors which influence the validity of the SKT at the time and location of each MW observation. These include the accuracy of the initial SST products, the accuracy of the parameterizations described above which convert the SST to the SKT and the methods used to convert the SKT from the model time-step and location to the time and location of the MW observation. In addition, no attempt is made to translate the representative depth of the SKT to the depth which the MW measurement represents.
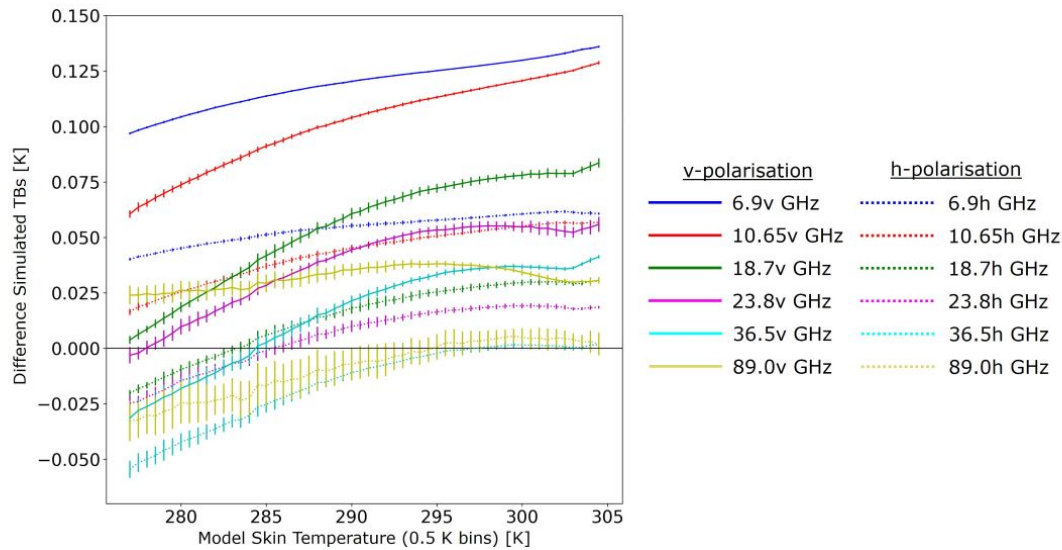
Figure 1: Mean change in the simulated TBs in RTTOV as a result of changing the input SKT by adding 0.2 K for the set of AMSR2 observations over ice-free ocean in the 2022-06-01 0Z cycle (21h to 09h) under clear sky conditions. The change is shown for each channel as a function of the original unaltered SKT. The vertical bars represent the standard deviation of the change.

To demonstrate the impact that SKT errors can have on the simulated TBs, a perturbation experiment, where the SKT has been increased by 0.2 K, has been undertaken and the results shown in Figure 1 for clear-sky conditions (with the split between clear and cloudy described in Geer and Bauer (2011)). This Figure shows that a change of 0.2 K results in small changes across all channels in the simulations (with a magnitude of up to about 0.125 K for the 6.9v GHz channel) and therefore any errors in the SKT have the potential to adversely affect the overall atmospheric forecast by aliasing into the atmosphere through the assimilation of surface-sensitive radiance observations (see also English, 2008).

With the aim of addressing the impact that any mis-match between the true and specified SKT have on the TOA TB simulations, this work uses a sink variable approach which produces SKT increments. This approach allows the SKT to vary per observation location in the 4D-var minimisation in addition to the current control variables: air temperature, pressure, relative humidity and wind vectors. Such an approach has previously been employed for the clear-sky radiances operationally in the ECMWF-IFS for many years, i.e. Infrared Atmospheric Sounding Interferometer (IASI), Cross-track Infrared Sounder (CrIS), Atmospheric Infrared Sounder (AIRS) and Advanced Technology Microwave Sounder (ATMS). More recent work has experimented with creating a 2D map of SKT increments applicable to multiple observation sets (Massart et al., 2021; Massart, 2023) but this is not yet operational and is not used in this work, partly due to the difficulty of following the rapid variation in SKT through the day, and partly due to the varying penetration depths of different sensors.

The ultimate aim for this work is to prepare for the use of these SKT increments in the coupled atmosphere-ocean system that is planned to become operational at ECMWF in the near future. These increments would no longer be sink variables (non-cycled information of which the system retains no memory) but rather used to correct the underlying 3D ocean state provided by the ECMWF ocean model, NEMO, and would be used to adjust the SST using a 3D-Var system (de Rosnay et al., 2022; Browne et al., 2019; ECMWF, 2019). Preliminary work has been undertaken to demonstrate this methodology for IR observations (McNally et al., 2022) which showed that the inclusion of SKT increments would result in
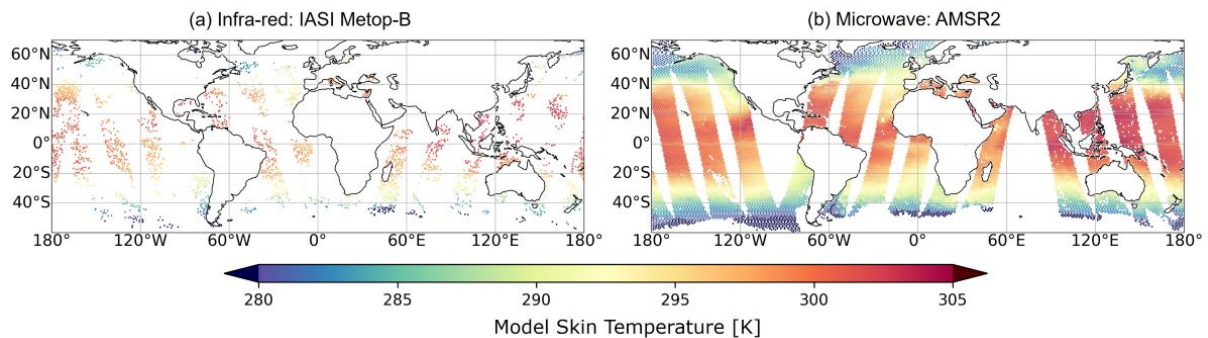
Figure 2: Background SKT values at locations of observations used in the atmospheric data assimilation for (a) IASI on-board MetOp-B channel number 921 and (b) AMSR2 18.7v GHz channel for the 2022-07-15 0Z cycle (21h to 09h).

improvements to both the ocean and atmospheric analysis.

The current work focuses on the MW instruments processed under all-sky conditions (clear and cloudy). It is well known that the MW range is sensitive to SST (e.g. CEOS (2020); Minnett *et al.* (2019) and others) and in addition, the MW range allows for a much greater spatial coverage compared to the IR, as shown in Figure 2, as it can be used under all-sky (clear and cloudy) conditions.

Surface sensitive channels are available on the MW imagers Advanced Microwave Scanning Radiometer 2 (AMSR2) (6.9v/h and 10.65v/h GHz) and GMI (10.65v/h GHz) however these channels have never been actively assimilated over open ocean into the ECMWF-IFS before. The initial part of this work implements the appropriate Quality Control (QC) measures for the v-polarisation channels (Section 2.2 and 2.3) and assesses their impact on the atmospheric forecast system without attempting to update the SKT (Section 2.5).

In terms of the SKT increments, the methodology is provided (Section 3.1) and then it is demonstrated that the use of 6.9v/h and 10.65v/h GHz provides valuable information about the surface as well as constraining the SKT sink variable so that signals from other factors, i.e. clouds, are not aliased into the variable (Section 3.2).

The configuration to be used in generating the SKT increments is considered (Section 3.3) in terms of the observation errors for 6.9v and 10.65v GHz, the SKT errors and the potential generation of SKT increments for observations which are thinned from the atmospheric DA. The SKT increments generated using the sink variable approach are then analysed with a focus on the difference between night-time and day-time observations which allows the consideration of the accuracy of the initial SST and cool skin and warm layer parameterization, with specific regions being analysed temporally (Section 3.4). It is then demonstrated that activating the SKT increments has a neutral impact on the atmospheric forecast (Section 3.5).

All of the experiments presented in this report were run over two seasons (2021-12-01 to 2022-02-28 and 2022-06-01 to 2022-08-31) at a model resolution of TCo399 (29 km) with a final incremental analysis resolution of T_L255 (80 km) and 137 vertical levels.

Table 1: MW Imager Channels / Polarisations Currently Actively Assimilated in the ECMWF-IFS operational system as of June 2024 with channel numbers shown in brackets. Note: MWRI was removed from the system in May 2023 (Scanlon *et al.*, 2023).

Freq. (GHz)	AMSR2		GMI		SSMIS	
	Used	Not Used	Used	Not Used	Used	Not Used
6.925	-	V(1) + H(2)	-	-	-	-
7.3	-	V(3) + H(4)	-	-	-	-
10.65	-	V(5) + H(6)	-	V(1) + H(2)	-	-
18.7 / 19.35	V(7) + H(8)	-	V(3) + H(4)	-	V(13) + H(12)	-
23.8 / 22.235	V(9) + H(10)	-	V(5)	-	V(14)	-
36.5 / 37.0	V(11)	H(12)	V(6)	H(7)	V(16)	H(15)
89.0 / 91.655	V(13)	H(14)	V(8)	H(9)	V(17)	H(18)

2 Adding the 6.9v and 10.65v GHz Channels from AMSR2 and GMI

2.1 Introduction

To date, only MW imager channels above 18.7v/h GHz have been exploited over open oceans (excluding sea-ice areas) in the ECMWF-IFS. Whilst there has been extensive recent work to use 10.65v/h GHz from MW imagers over sea-ice (Geer, 2024b,a), this and the 6.9v/h GHz channels have never been used over non-sea-ice contaminated ocean areas. This is primarily due to their sensitivity to the surface rather than the atmosphere. However, it is hoped that 10.65v/h GHz in particular can contribute to the analysis of tropical convection and heavy rain (Geer *et al.*, 2017). In the context of the current work, it is demonstrated in Section 3.2 that these channels are of interest when optimising the SKT using the sink variable approach and the importance of the 6.9v GHz channel is emphasised.

The 6.9v/h and/or 10.65v/h GHz channels are available on AMSR2 and GMI[1] (see Table 1). Further information on the impact of AMSR2 and GMI on the ECMWF-IFS can be found in Kazumori *et al.* (2014, 2016) and Lean *et al.* (2017) respectively.

Although 7.3v/h GHz is also available on AMSR2, this channel is focused primarily on Radio Frequency Interference (RFI) mitigation and is not considered for use in the atmospheric DA (see Section 2.2.3 for more information on RFI). Note that no attempt has been made to assimilate the 6.9h and 10.65h GHz channels on AMSR2 or GMI for this work due to their known increased sensitivity to the atmosphere, which is demonstrated in Figure 1 with the h-polarisation channels showing less response to the change in the SKT. These channels could provide benefit in future and have been excluded here mainly to simplify the initial work.

The background departures (the difference between the observation and the brightness temperature simulated from the background forecast) for 6.9v and 10.65v GHz channels without any channel specific QC in place can be seen in Figure 3 for AMSR2 (panels a to b) and GMI (panel c). The background departures shown here and in the remainder of the report include the bias correction generated by VarBC (Dee, 2004), which is discussed further in Section 2.3. Those for the newly introduced channels are shown in panels (a) to (c) and an example of a previously assimilated channel (18.7v GHz) from AMSR2 shown in panel (d). It is clear from these results that QC is required before these channels can be assimilated in the atmospheric system.

---

[1]Note that although 10.65v/h GHz is available on the Microwave Radiation Imager (MWRI), this was removed from operational use in May 2022 (Scanlon *et al.*, 2023)
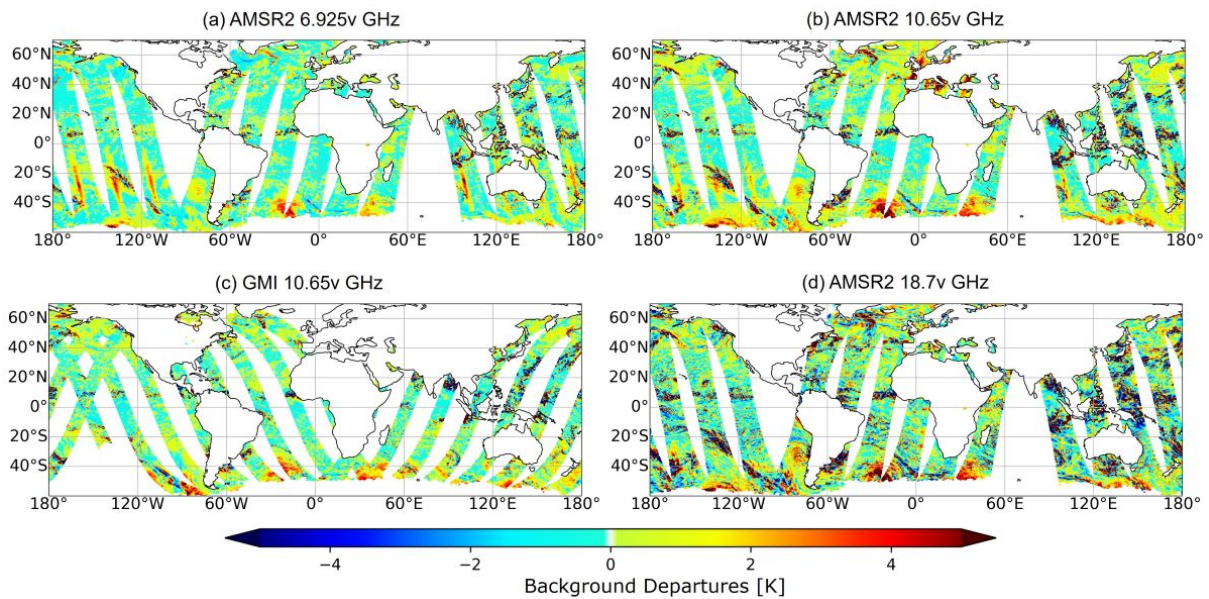
Figure 3: Background departures prior to any low-frequency specific QC being implemented for (a) AMSR2 6.25v GHz, (b) AMSR2 10.65v GHz, (c) GMI 10.65v GHz and (d) AMSR2 18.7v GHz for 2022-07-15T00.

Not visible in Figure 3, but shown more clearly in Figure 4, there are areas of high positive background departures around the coastlines for 6.9v GHz and this can be attributed to the presence of land in these observations (see Section 2.2.1). This is due to the larger footprint of the 6.9v GHz channel than that of the 10.65v GHz channel being used for the current land screening process. For both AMSR2 6.9v GHz (a) and 10.65v GHz (b), there are large positive background departures occurring to the western edge of each ascending swath in the Southern Hemisphere (SH), where ascending swaths are the parts of the orbit where the satellite is travelling broadly towards the northwest. These large positive background departures are attributed to sun-glint (see Section 2.2.2). Finally for the AMSR2 10.65v GHz channel there are large positive departures over Europe and these can be attributed to RFI from direct broadcast satellites (see Section 2.2.3). Note that these features are not present in the background departures for the 18.7v GHz channel and hence are unique to the lower frequency channels.

For the GMI 10.65v GHz channel (Figure 3(c)), these issues are not apparent: the coastlines are already screened using the 10.65v/h GHz footprint and RFI issues are not apparent. However, on closer inspection (shown later in Figure 7(d)) it is found that GMI suffers from the sun-glint issue at very high latitudes.

Note that in addition to the features described, Shibata (2013) states that the cold sky mirror can block the main reflector of AMSR2 at the rightmost scanning position and this can result in a temperature drop of 1.5 K over oceans for the 6.9v GHz channel. There has been no evidence of this seen in the background departures or the observations used at ECMWF, likely due to the observations being subjected to averaging (superobbing) which means the impact of this issue is much diminished and therefore no specific treatment of this artefact has been implemented here.

The work undertaken here is based on the 48R1 cycle which is currently operational (from June 2023 onwards ECMWF (2023b) which includes the advances relating to the processing of microwave observations described in Geer et al. (2022)) with the addition of various upgrades to the MW observation

processing intended for inclusion in the next operational cycle. The key changes relevant to the current work are the use of a machine learning based approach for estimating sea-ice (Geer, 2024b,a), the replacement of FASTEM-6 with the SURface Fast Emissivity Model for Ocean (SURFEM-ocean model) (Geer *et al.*, 2024; Kilic *et al.*, 2023) which is a fast implementation of Passive and Active Reference Microwave to Infrared Ocean (PARMIO) (Dinnat *et al.*, 2023) and the use of 40 km (instead of 80 km) superobbing.

The activation of the sea-ice sink variable means that the SKT increments are not calculated where the model SKT is below 277.0 K because these points are already used for sea-ice concentration estimation and the simultaneous estimation of SKT and sea-ice concentration is probably ill-posed.

Note that choices have been made within the SURFEM-ocean model (Kilic *et al.*, 2023) specifically to improve the performance at very low frequencies (i.e. 7 GHz and below) for example, the use of the Meissner and Wentz (2012) permittivity model. An assessment of the use of this model in comparison to the previously used FASTEM-6 model is presented in Geer *et al.* (2024). For the 6.9v/h and 7.3v/h GHz channels of AMSR2, moving from FASTEM-6 to SURFEM-ocean increases the Root Mean Squared Error (RMSE) of the bias correction against the baseline where FASTEM-6 is used but reduces the standard deviation of the background departures by around 0.1 % which is evidence that SURFEM-ocean does have slightly improved low frequency performance.

2.2 Quality Control

2.2.1 Coastline Screening

Each AMSR2 channel has a different footprint size, with that of the 6.9v/h and 7.3v/h GHz channels being substantially larger than those for the higher frequency channels (see Table 1 and Figure 2 of Maeda *et al.* (2016) for further details). For reference, Maeda *et al.* (2016) states that the footprint corresponding to a -3 dB beam width is 35 km by 62 km for the 6.9v/h GHz channel and 24 km by 42 km for the 10.65v/h GHz channel (cross-track by along track).

Currently, the land screening process is based on the footprint size of the 10.65v/h GHz channels as it was previously considered the "worst case" scenario. To allow the introduction of the 6.9v/h GHz channel, the coastline screening is adapted to screen based on the footprint of the 6.9v/h GHz channel for all channels below 10.65v/h GHz and on the 10.65v/h GHz channel for all channels above, including the 10.65v/h GHz channel itself (as is the current case).

The land screening process is based on the superob land fraction. To compute this, the spatial response (antenna pattern) of each raw observation is integrated over a high resolution land-sea mask to find the land fraction specific to that raw observation. Then the land fractions of the raw observations are averaged to find the land fraction of the superob, where a superob is the average of the raw observations whose centres fall into a roughly 40 by 40 km region of the Earth's surface. A superob land fraction greater than 0.01 results in rejection of the observation from the ocean pathway of the all-sky assimilation framework (although some higher frequency channels are used over land and coastal scenes in an alternative pathway, see Geer *et al.* (2022)).

The implementation of the additional land screening for 6.9v/h and 7.3v/h GHz channels has led to a reduction in the number of high background departures around coastlines for AMSR2. This is shown for the 6.9v GHz channel for a single cycle over Southern Europe in Figure 4(a) before, and (b) after the screening has been implemented and for a monthly average in (c) and (d). Particular areas in which the screening out of high background departures can be seen are north of Spain and in the Adriatic Sea,
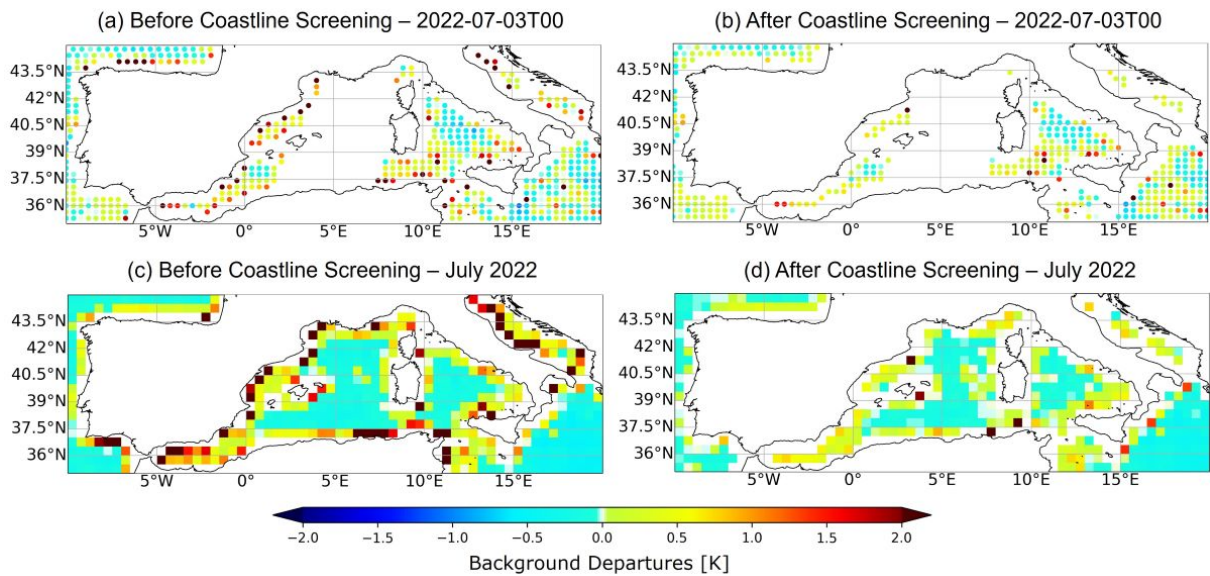
Figure 4: Background departures for the AMSR2 6.9v channel (a and c) before and (b and d) after screening for coastlines using the 6.9v GHz footprint size for (top) a single cycle (2022-07-03T00) and (bottom) averaged over a month (2022-07-01T00 to 2022-07-31T12).

as well as along the coast of north Africa. In addition, the implementation of the screening results in a 1 % improvement in the fit to observations (in terms of the global standard deviation of background departures) for the 6.9v GHz channel (not shown). There remains a slight halo of order 0.1 K in coastal areas in Figure 4(d), even after coastal screening. This likely caused by a combination of trace FOV sensitivities outside of the spatial response function used for the masking and the the land fraction limit used (0.01). Future testing may consider a more stringent threshold for the land screening.

In addition to the coastline screening being updated for the 6.9v/h GHz channels of AMSR2, this work was an opportunity to apply the broader method of calculating the FOV within the 10.65 GHz 3 dB footprint to MWRI on-board Fengyun-3D (FY-3D) for the first time. The footprint size used for the 10.65v/h GHz channel of this sensor was taken from Lawrence *et al.* (2017). The improved coastal screening resulted in 3.5% more data being used from this sensor, similar to earlier unreported results for GMI and AMSR2. Although this sensor is not used after May 2022 (see Scanlon *et al.*, 2023), this implementation brings it in line with the other MW imagers and makes the method available for any future versions of the MWRI sensor.

2.2.2 Sun-Glint Screening

Sun-glint, where radiation from the sun is reflected directly from the surface into the sensor, is known to affect AMSR2 observations at the lower frequencies (10.65v/h GHz and below) leading to artificially inflated observed TBs (Kazumori *et al.*, 2014). The effect is not currently included in RTTOV and therefore, evidence of sun-glint is apparent in the background departures without the QC implemented in Figure 3(a and b) for these channels; the biases are in the range of 3 to 6 K as has been previously seen for AMSR2 (Kazumori *et al.*, 2014) and GMI (Xue and Guan, 2019).

At higher frequencies, the effect of sun-glint is known to be minimal (Kazumori *et al.*, 2014), for example see the departures for AMSR2 18.7v GHz in Figure 3(d). A possible explanation as to why these
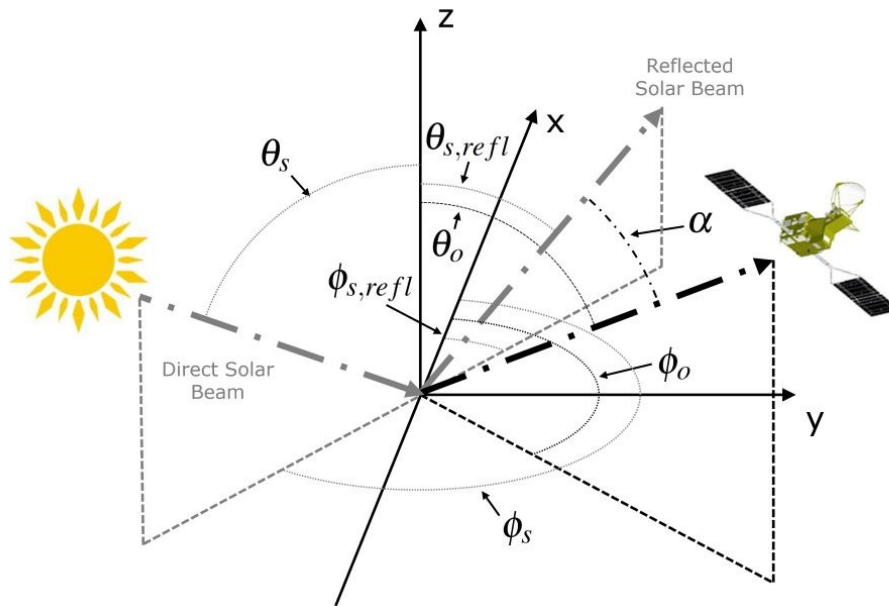
Figure 5: The sun-satellite geometry and angles used in the calculation of the glint angle.

artefacts are present at these lower frequencies is that the output of the sun in the microwave range can be significantly larger than at the higher frequencies, with the magnitude depending on the activity level of the sun, as shown in Figure 3 of Ho *et al.* (2008). The time period shown in Figure 3 is July 2022, which is in a period of heightened solar activity (with the last 11-year minima being in January 2020) likely making the sun-glint particularly strong at 6.9v/h and 10.65v.h GHz on these dates.

The geometry of sun-glint is shown in Figure 5 with the quantities relating to those provided in Eq. 1. The x- and y-axes represent North and East respectively and the z-axis is perpendicular to the Earth's surface. Eq. 1 is already used for sun-glint calculations in the ECMWF-IFS and has been proven in other applications (e.g. Moderate Resolution Imaging Spectroradiometer (MODIS) (Levy *et al.*, 2013) and Sea-viewing Wide Field-of-view Sensor (SeaWiFS) (Wang and Bailey, 2001)). The glint equation is as follows:

$$\cos \alpha = \cos \theta_o \cos \theta_s - \sin \theta_o \sin \theta_s \cos (\phi_o - \phi_s) \tag{1}$$

Where α is the glint angle, θ represents zenith angles and ϕ represents azimuth angles with respect to north and the subscripts o and s denote the observation (sensor) and sun respectively (as shown in Figure 5). The glint angle is the angle between the observation beam and the reflected solar beam, which is described by $\theta_{s,refl} = \theta_s$ and $\phi_{s,refl} = \phi_s - \pi$ (assuming specular reflection from a horizontal surface). However, Eq. 1 is more conveniently expressed in terms of the solar position θ_s, ϕ_s.

To screen the data within the ECMWF-IFS, a glint angle threshold needs to be set, under which the observations will be screened out. For this work, the 6.9v and 10.65v GHz channels on-board AMSR2 and GMI are specifically targeted. Figure 6 shows the response of the background departures to the sun-glint angle for both sensors and channels. From these plots it can be seen that the background departures start to level-off at about 25° and therefore, the threshold is set at 25° for all affected channels. This is also in line with the conclusions of Kazumori *et al.* (2014) and Yang *et al.* (2016) for AMSR2. For GMI, Xue and Guan (2019) suggested a threshold angle of 20° for the 10.65v GHz channel for GMI, however,
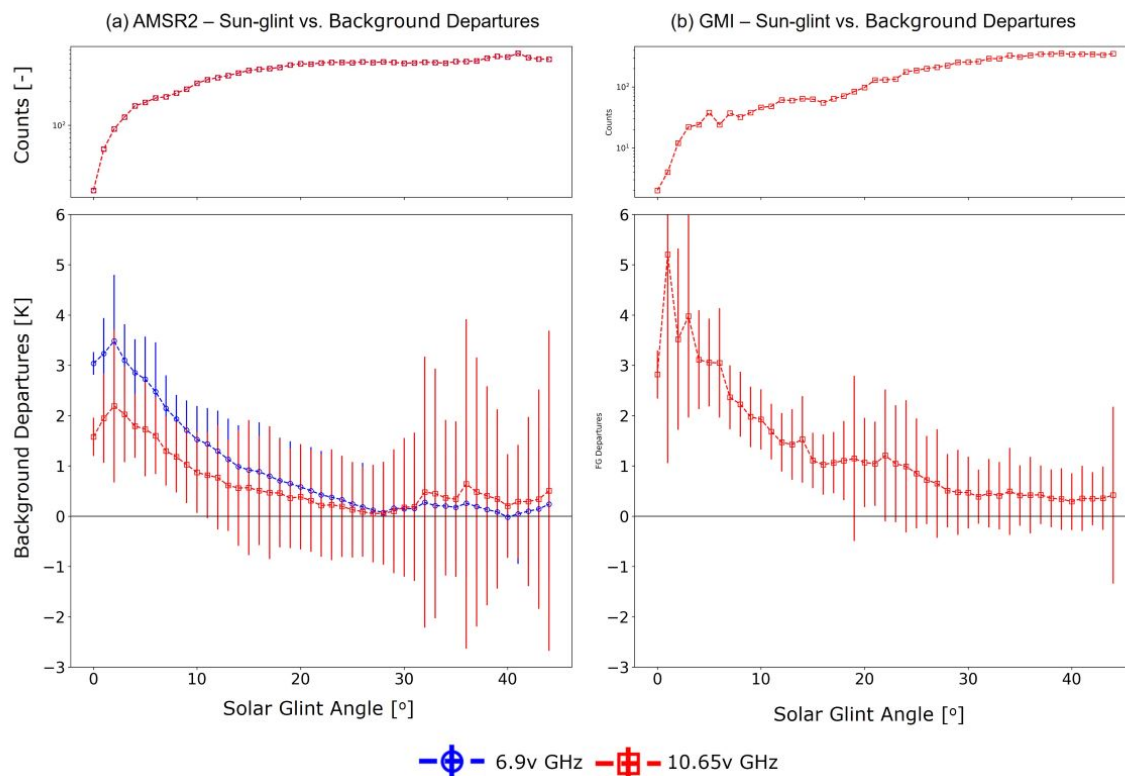
Figure 6: Sun-glint angle vs. background departures for the period 2022-06-02T00 to 2022-06-12T12 for (a) AMSR2 6.9v and 10.65v GHz and (b) GMI 10.65v GHz for all data (i.e. that prior to thinning and screening but after superobbing).

Figure 6 suggests the threshold should be higher in this case.

Figure 7 shows the background departures before (a and d) and after (c and f) the implementation of the sun-glint screening, with the sun-glint angles shown in (b and e) for different regions for AMSR2 and GMI. It can be seen that although the $25°$ results in a large area being screened out, this is necessary to fully capture the area effected by the sun-glint. Modelling of the sun-glint effect has been considered within RTTOV and this may become possible in the future, potentially allowing the inclusion of some of these affected observations.

2.2.3   Radio Frequency Interference Screening

RFI is when the signal of interest is affected by external ground- or satellite-based man-made sources (such as TV broadcasts, radar, phone and internet communications) resulting in the natural signal being masked. For MW imagers, it is generally manifested as much higher TBs than expected, however, it also varies depending on the characteristics of the sensor (Le Vine, 2017). In general, the more significant RFI signals are seen over land (Wu et al., 2019), impacting various applications (for example, soil moisture (Bai et al., 2022)). Due to this, the majority of RFI mitigation strategies focus on land surfaces (e.g. (Draper and de Matthaeis, 2018; Bai et al., 2022; Shen et al., 2022; Wu et al., 2019; de Nijs et al., 2015)).

The work presented here, however, relates only to RFI signals over the ocean, as the 6.9v and 10.65v GHz
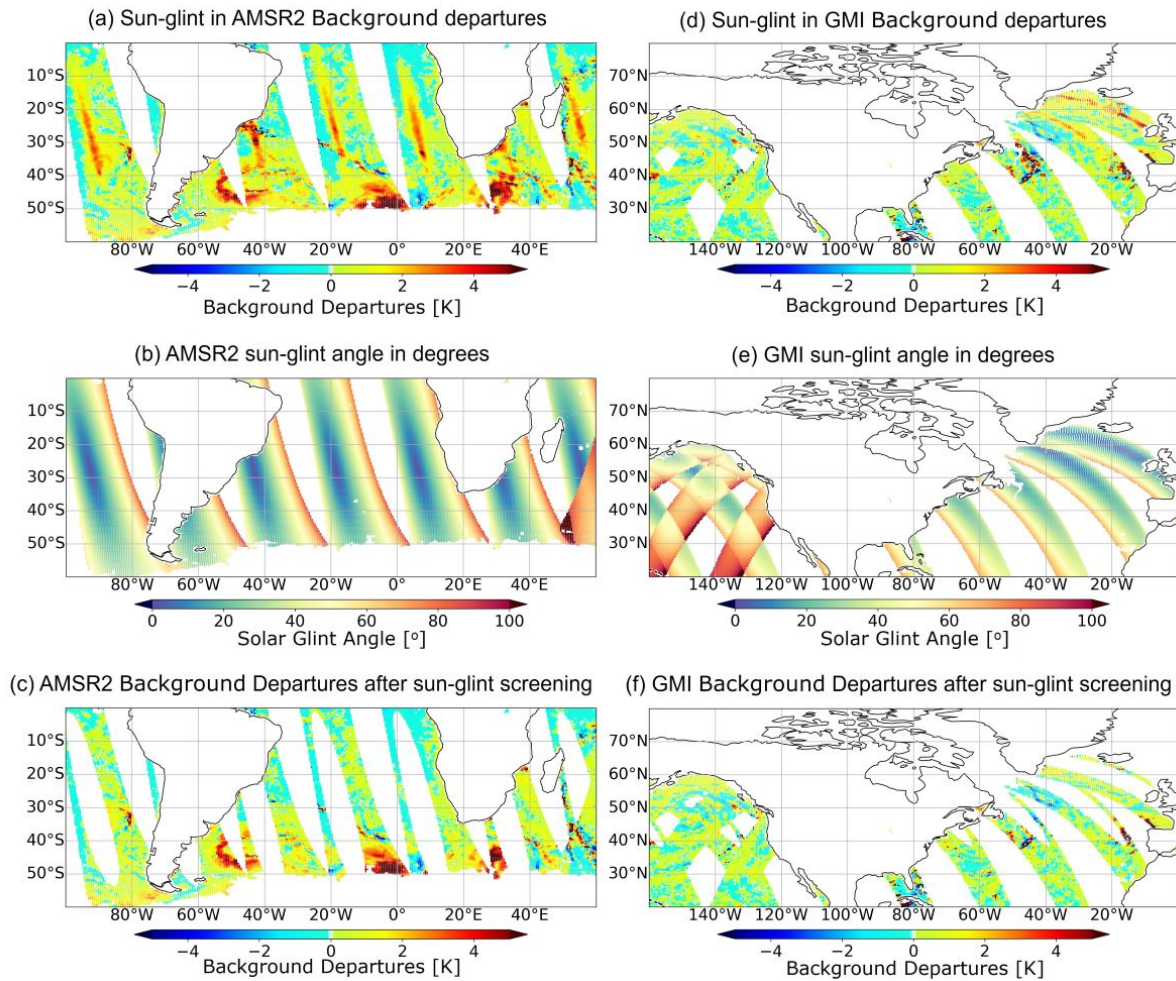
Figure 7: Maps for 2022-06-01T12 showing (top) background departures before any screening is applied, (middle) the calculated sun-glint angle and (bottom) the background departures after screening for a sun-glint angle of less than $25°$ for (a to c) the AMSR2 6.9v GHz channel and (d to f) the GMI 10.65v GHz channel. Note that although not shown here, the 10.65v GHz channel from AMSR2 is also subject to sun-glint screening.
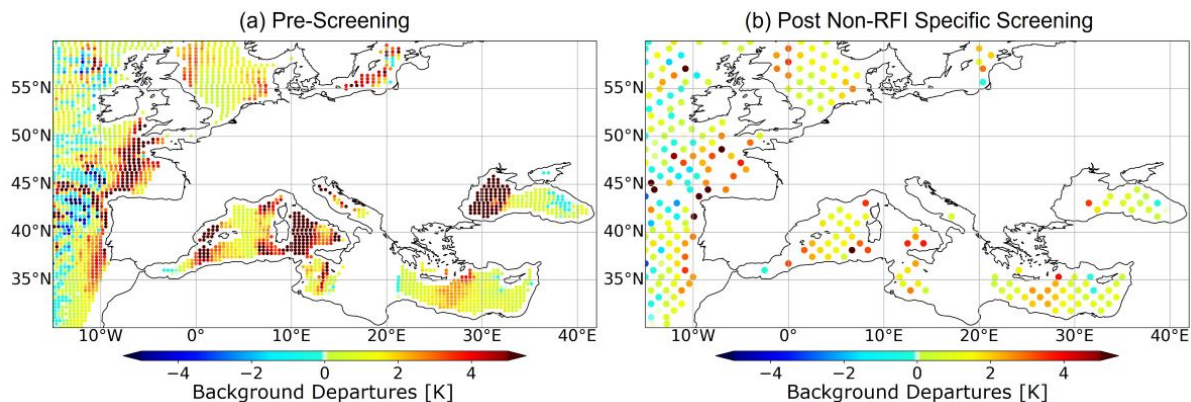
Figure 8: Background departures for the AMSR2 10.65v GHz channel for 2022-06-02T00 (a) before and (b) after the implementation of the previously used, non-RFI specific, screening process.

channels are being activated due to the interest in the ocean SKT. In particular, RFI as a result of direct broadcast geostationary satellites is considered where the signal is reflected off the ocean surface and into the observation sensor (i.e. AMSR2 or GMI). This seems to cause the majority of the RFI glint seen at these lower frequencies.

A clear example of such RFI is the signal seen in the 10.65v GHz channel of AMSR2 over Europe (see Figure 8(a)). The 10.69 GHz band is protected with a bandwidth of 100 MHz (NTIA, 2016) but is immediately adjacent to a band allocated for space-to-earth transmission (Draper and Newell, 2015; NTIA, 2016). In this case, there is significant RFI contamination, manifested as large scar marks in the descending overpass, where descending swaths are the parts of the orbit where the satellite is travelling southwards. Figure 8(b) shows that after thinning and the current screening process (Var-QC) is implemented, remnants of these large background departures remain and therefore bespoke screening is required to address such signals[2]. Note, all of the examples shown here for AMSR2 are for the 10.65v GHz channel, however, similar patterns are also seen in the 10.65h GHz channel.

There are some studies which have focused on the detection of RFI over oceans. Draper and de Matthaeis (2018) and Draper (2016) use a generalised RFI index which derives a fit between the channel of interest and a linear combination of other channels. Zabolotskikh et al. (2015) uses spectral differences to identify RFI with different thresholds applied to different band combinations; this work concludes that the method, although simple, suffers from inaccuracy under certain conditions including intense rainfall. Wu et al. (2020) proposed a new generalised method (similar to that used in Draper and de Matthaeis (2018) and Draper (2016)) and validated this using a double principle component method although it is noted that this method is sensitive to the presence of ice. Finally, Draper and Newell (2015) used a spectral difference method to find instances of RFI and part of this work included determining the likely position of the geostationary satellite causing the identified signals. Methods where spectral differences play a role benefit from the availability of the 7.3v/h GHz channels on-board AMSR2 which is used to detect RFI in the 6.9v/h GHz channels (Kazumori et al., 2016).

Using these methods, Draper (2016) and Draper and Newell (2015) identified RFI for GMI at 18.7v GHz around the continental USA and both Draper and de Matthaeis (2018) and Wu et al. (2020) see similar RFI for the corresponding 18.7v GHz channel of AMSR2. In terms of the signal over Europe at 10.65v/h GHz for AMSR2, Wu et al. (2020), Zabolotskikh et al. (2015) and Draper and de Matthaeis

---

[2]Note that although RFI flags are available in Level 1B AMSR2 data (Murata et al., 2022), these are not propagated into the data stream used at ECMWF.

(2018) identified areas of RFI and in Wu *et al.* (2020) it is shown that these patterns are similar to those in Figure 8(a).

Here, the issue is approached by considering the geometry of direct broadcast satellites with the observation satellite. Equation 2 (based on Equation 1 and the quantities shown in Figure 5 given in Section 2.2.2) is used with the zenith and azimuth of the geostationary satellite (relative to the observation location) to determine the glint angle between the directly reflected broadcast signal and the observation beam, as follows:

$$\cos \alpha = \cos \theta_o \cos \theta_b - \sin \theta_o \sin \theta_b \cos (\phi_o - \phi_b) \tag{2}$$

Here, the subscript b denotes that the quantity relates to the broadcast satellite (replacing the solar angles denoted by s in Figure 5 and Eq. 1). The zenith and azimuth of the broadcast satellites, θ_b and ϕ_b respectively, are calculated using routines already present in the ECMWF-IFS which are not described further here.

Using the assumption that the broadcast satellite is in geostationary orbit and is hence positioned over the equator, the only unknown becomes the associated sub-satellite longitude (hereafter referred to as the longitude). To identify the likely longitude of the satellites causing the suspected RFI signal, a theoretical study has been performed in which 360 satellites have been placed around the globe at the equator with a 1° longitudinal spacing, at the altitude of a geostationary orbit which is 35786 km, i.e. 42164 km from the centre of the Earth.

The glint angle between these satellites and the sensor of interest (in this case AMSR2 or GMI) is calculated for each observation location. For all observations where the glint angle is under 3°, a series of metrics are calculated for the background departures: the mean, the standard deviation and the 95th percentile. The threshold of 3° is chosen to pick out the most central of the glint features. In addition, for those observations where the glint angles are under 10°, the correlation between the glint angle and the background departures are calculated. From the combination of this information, it is possible to determine if the RFI is likely to be caused by a broadcast satellite positioned at a particular longitude. For example, where the mean, standard deviation and 95th percentile are high and the correlation is highly negative, it is likely that RFI from direct broadcast satellites is present. In addition, this can be compared to other channels and maps of the background departures and associated observations to confirm the presence of RFI.

It is noted that the method may not be robust under the following conditions: 1) where there is an area of high background departures caused by other factors around the region of the RFI glint, thereby diluting the signal; 2) where the effect of the RFI is reduced due to increased scattering from the surface (e.g. where high wind conditions have increased the surface roughness) or where there is strong extinction in the atmosphere (e.g. where heavy rain is present); and 3) where the transmission beam is purposefully directed only over certain areas (as is most often the case). To account for these potential issues, the method is applied under clear-sky conditions only and over pre-selected small areas of the globe where RFI is suspected.

Figure 9 shows the results of this method over Europe (the area shown in Figure 8) for a 10 day period in June 2022; for simplicity only the mean and the correlation metrics are shown here. Note that the data on which this is based has already been subject to coast and sun-glint screening, as described in Sections 2.2.1 and 2.2.2 to minimise the inclusion of any high background departure signals unrelated to RFI.

From Figure 9, it can be seen that there are likely broadcast satellites at three longitudes causing the
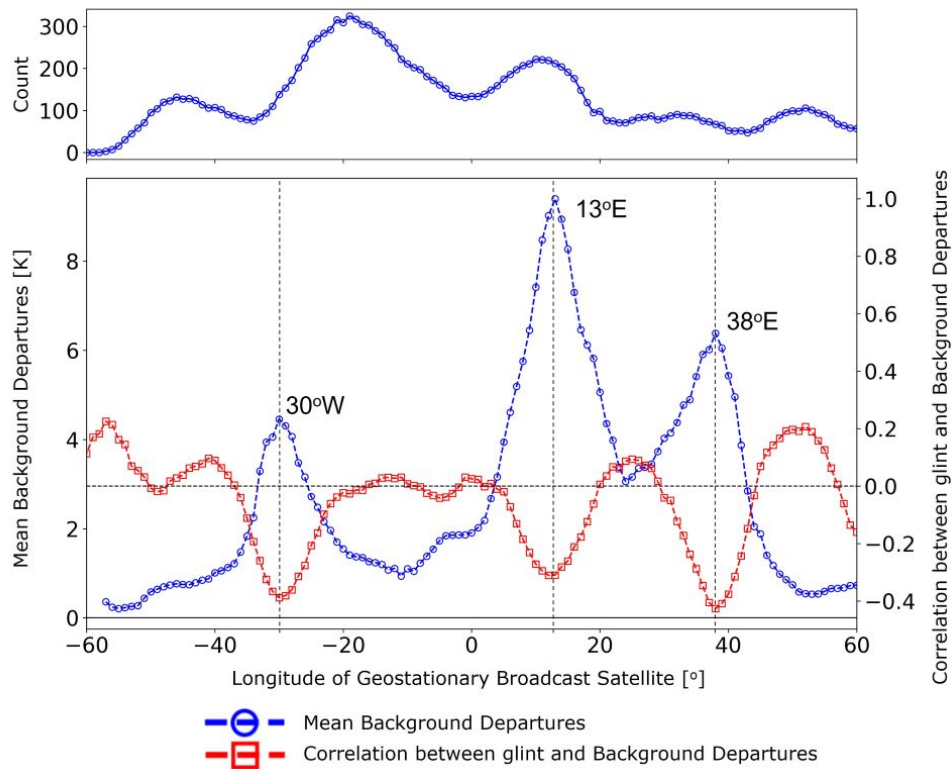
Figure 9: With geostationary satellites placed at 1° longitude spacings (at the equator), the mean of the background departures over Europe is calculated for the locations where the corresponding glint angle is less than or equal to 3° (blue line) and the correlation is that between the background departures and the glint angle for all locations where the glint angle is less than or equal to 10° (red line).

glint patterns seen over Europe: 30°W, 13°E and 38°E, with the signal at 13°E being the strongest. In each case it can be seen that as the mean of the background departure increases, the correlation between the glint angle and the background departures becomes strongly negative, indicating that the increase in departures is related to the glint angles that would be achieved with a broadcast satellite at the relevant longitude. In each of these cases, the local maximum of the mean background departures and the minimum of the correlation align to within 1°, with small changes being possible due to other effects such as model biases or the impact of the superobbing process; where there is a conflict between the two, the peak of the mean background departures has been chosen as the longitude.

The glint patterns from each of the identified broadcast satellites correspond to different parts of the high background departures seen over Europe. Figure 10 shows the background departures with the glint angles for when the broadcast satellite is positioned at the longitudes identified from Figure 9; only those glint angles below 20° are provided to show the areas that are screened out with this threshold. This threshold could be reduced on a per-source basis, however, this is a bounding case valid at all times of the year to remove the large errors created by these sources. In the future, it may be refined and could depend on a variety of factors including the surface roughness. From this Figure, it is clear that the satellite at 13°E causes the largest of the high background departure scar patterns: both that going through the UK and down to Spain and across Italy and through the Black Sea, while the smaller pattern to the East of Spain is caused by the satellite from 30°W. Finally, the satellite at 38°E contributes to the patterns seen to the north of the Netherlands and the south-east of Italy.
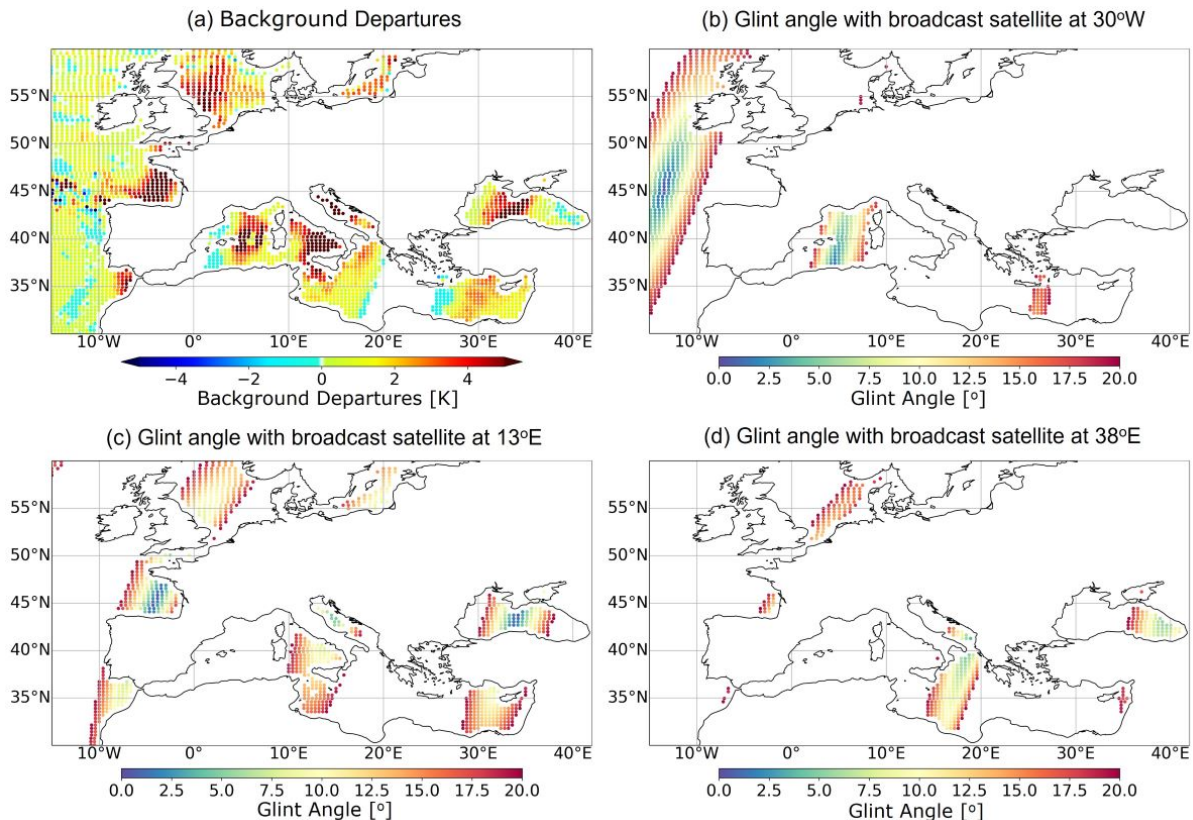
Figure 10: Maps for 2022-07-15T00 for (a) background departures due to RFI contamination and the glint angles of the observations with geostationary satellites placed at (b) 30°W, (b) 13°E and (c) 38°E. The glint angles have a cut off threshold of 20° thereby indicating the area that is screened out by the RFI screening process.

At each of the identified longitudes (or very close to them for the case of 38°E) there are satellites broadcasting over the affected parts of Europe in frequencies close to 10.65v/h GHz (for further information see SatBeams (2024) and SatExPat (2024)). In each of these cases, the closer broadcast channel is a h-polarisation channel, with the v-polarisation generally being a few MHz higher. The analysis shown here is for the v-polarisation, however similar patterns are noted in the 10.65h GHz channel from AMSR2. It is noted there is potential for the polarisation of the radiation to change when interacting with water, taking into account the likely inclined angles of the surface due to wave patterns, hence each channel could be affected by the satellite signal of the opposite polarisation.

The analysis presented here has been applied to different areas of the globe and for the 6.9v/h, 10.65v/h and 18.7v/h GHz channels of AMSR2 and the 10.65v/h and 18.7v/h GHz channels of GMI. From this, the areas identified as being affected by this type of ocean reflected RFI are those over Europe in the 10.65v/h GHz channels of AMSR2 (with the v-polarisation shown above) and an additional signal in the 18.7v/h GHz channels of AMSR2 (see Figure 11) over the continental United States which had been previously recognised in Kazumori *et al.* (2016) and Kazumori *et al.* (2014).

Although not part of the work to activate 6.9v and 10.65v GHz in the ECMWF-IFS, the RFI signal in 18.7v GHz for AMSR2 requires some discussion as the coastal waters around the continental United
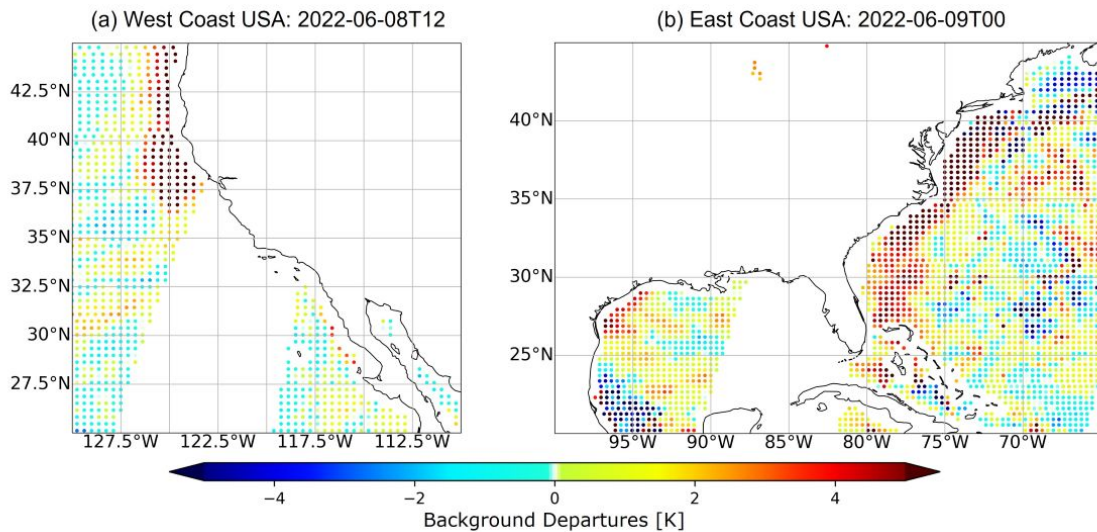
Figure 11: Background departure for the (a) west and (b) east coasts of the United States for the dates indicated.

States are key in the context of SST analysis[3]. Figure 11 shows examples of the ocean reflected RFI off the east and west coasts of the United States in June 2022 for the 18.7v GHz channel from AMSR2. It is found that these signals are most likely caused by a geostationary satellite at 102°W which has previously been identified as a potential candidate for causing this type of RFI signal in Draper and Newell (2015), giving confidence that this method correctly identifies this type of signal.

As discussed above, the literature (e.g. Draper and Newell (2015)) identifies several areas of RFI contamination in the GMI radiances. An extensive study was undertaken to find such RFI sources using the tools described here, however, no instances of RFI were identified. This may be either because the RFI sources are not a result of direct broadcast satellites, the signal in the background departures is weak in comparison to the surrounding data points and / or there are no instances of the RFI signal in the time period studied (2022-06-02 to 2022-07-31) for GMI. Due to this, no screening for RFI from direct broadcast satellites is applied to GMI.

2.3 Error Model and Variational Bias Correction

Figure 12 shows the error model (following the symmetric cloud predictor method described in Geer and Bauer (2011)) for the 6.9v and 10.65v GHz channels from AMSR2 (from Kazumori *et al.* (2016)) and the 10.65v GHz channel from GMI (from Lean *et al.* (2017)) after the implementation of the QC described in the previous sections for two seasons. Because these observation error models were fitted some years ago, before the QC described in this report was implemented, the resulting model is relatively cautious as the standard deviation of the background departures is always significantly below the error model limit (i.e. solid lines are below the dashed lines). Typically, error models for microwave imagers are fitted a little closer to the standard deviations, but these error models were considered acceptable for the initial testing of these channels. However, Section 3.3 investigates tightening up these error models in the context of obtaining larger SKT increments.

---

[3]Note that the results shown for the inclusion of 6.9v and 10.65v GHz do not include the screening of the 18.7v GHz channel.
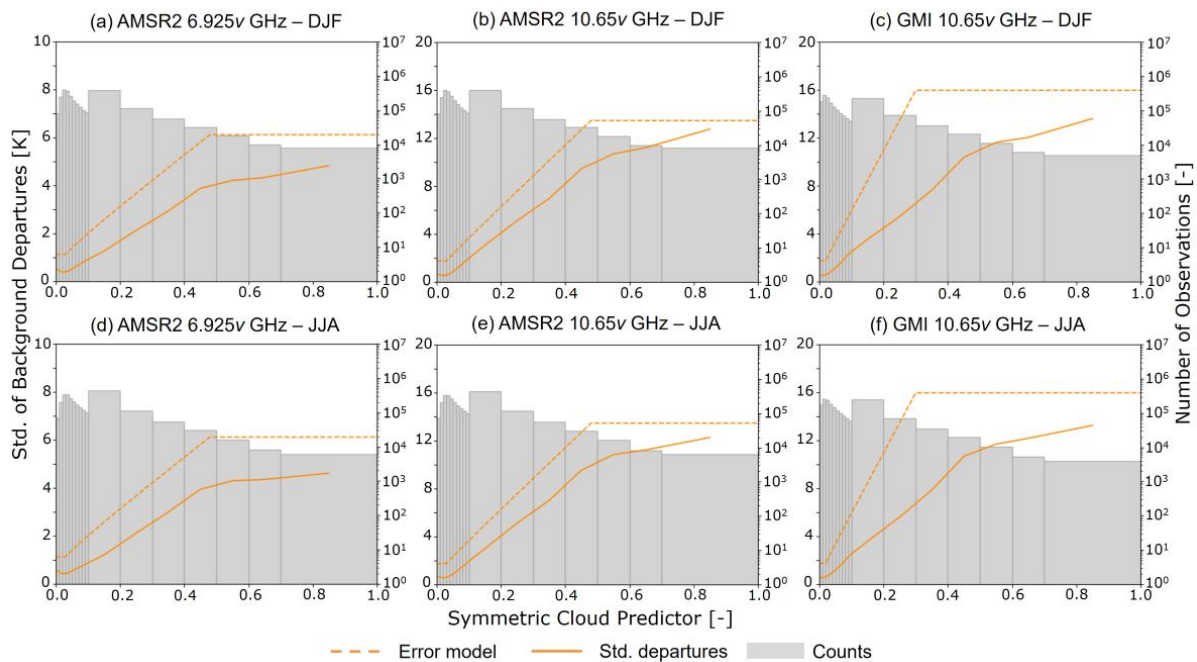
Figure 12: The error model (dashed line) and the standard deviation of background departures, for used observations associated with (a and b) AMSR2 6.9v and 10.65v GHz (c) GMI 10.65v GHz for 2021-12-07T00 to 2022-02-28T12, and the same (d, e, and f) for 2022-06-07T00 to 2022-08-31T12. Counts are shown in gray. The cloud proxy used is the normalised polarisation difference between the two polarisations of the 37 GHz channel, as described in Geer and Bauer (2011).

During this work, the bias predictors used in VarBC (Dee, 2004) for these channels have not been altered from those used for higher frequency channels (18.7v/h GHz and 23.8v/h GHz). The following set of predictors are used: a constant of 1, the model SKT, total column water vapour, the nadir view angle (to the power of 1, 2, 3 and 4), sea ice concentration and the wind speed multiplied by 1 minus the land fraction (meaning that the wind speed dependence is over ocean only).

2.4 Examining the Background Departures

Single cycle plots of the background departures of the 6.9v and 10.65v GHz channels from AMSR2 and the 10.65v GHz channel from GMI are shown in Figure 13 for a date in January (a to c) and July (d to f). Some loss of data due to the QC can be seen in these plots, with areas of missing data in both the southern oceans (due to sun-glint screening, see Section 2.2.2) and over Europe (due to RFI screening, see Section 2.2.3). However, when comparing to Figure 3 showing the July date before screening, it is clear that the QC is necessary.

A prominent feature over all channels and both seasons are the large positive background departures found polewards of 30° (northwards in January and southwards in July), shown in detail for the AMSR2 10.65v GHz channel in Figure 14(a and e). It is thought that these features are primarily the residual effects of Cold Air Outbreaks (CAOs) (as they match known spatial patterns, for example those shown in Kolstad et al. (2009)) and where the emissivity assigned is lower than it should be. Observations affected by CAOs are not currently used within the ECMWF-IFS for MW imagers as they are not well captured in the model with insufficient cloud liquid water being present in the model compared to reality, due to a
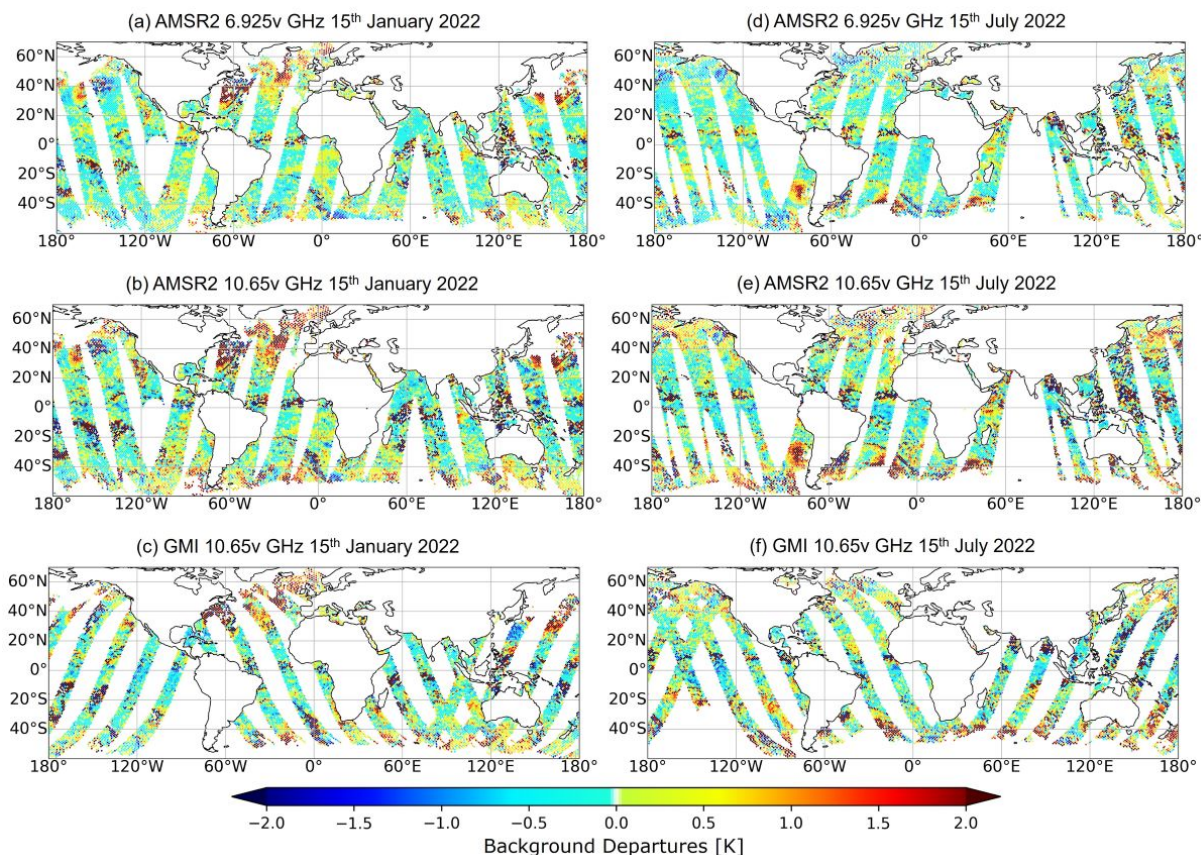
Figure 13: Global background departures for (a and d) AMSR2 6.9v GHz, (b and e) AMSR2 10.65v GHz and (c and f) GMI 10.65v GHz for the dates indicated after the implementation of the QC.

lack of water clouds being generated in unstable areas (Lonitz and Geer, 2015).

In Figure 14 the typical characteristics of CAOs can be seen in a small region to the south of Greenland (for January - a to d) and in the southern ocean between South America and Africa (for July - e to h). Large positive departures are seen coinciding with (b and f) areas of high wind-speed which are downwind from areas already screened out due to CAOs as well as (c and g) a negative difference between the air and sea temperature (i.e. the sea is warmer than the air). Such features have been noted before as affecting higher frequency channels of AMSR2 (Kazumori *et al.*, 2014) and a screening method is implemented for all channels in Lonitz and Geer (2015) which takes into account Total Column Water Vapour (TCWV), the Lower Tropspheric Stability (LTS) and the portion of the liquid and ice cloud water path that can be attributed to liquid. However, the results for the 6.9v and 10.65v GHz channels show that this screening may need further expansion to capture the edges of these features for these channels.

Note that these features are not seen to such a large extent in other channels; the 36.5v GHz channel is shown as an example in Figure 14(d and h). Given that the lower channels are most strongly affected the problem may come from an inadequacy in the surface emissivity model resulting in too low emissivities being assigned in areas of high wind-speeds (i.e. above 10 m/s); this could also be a result of insufficiently high surface wind speeds in the IFS. These possibilities are discussed further in Geer *et al.* (2024).

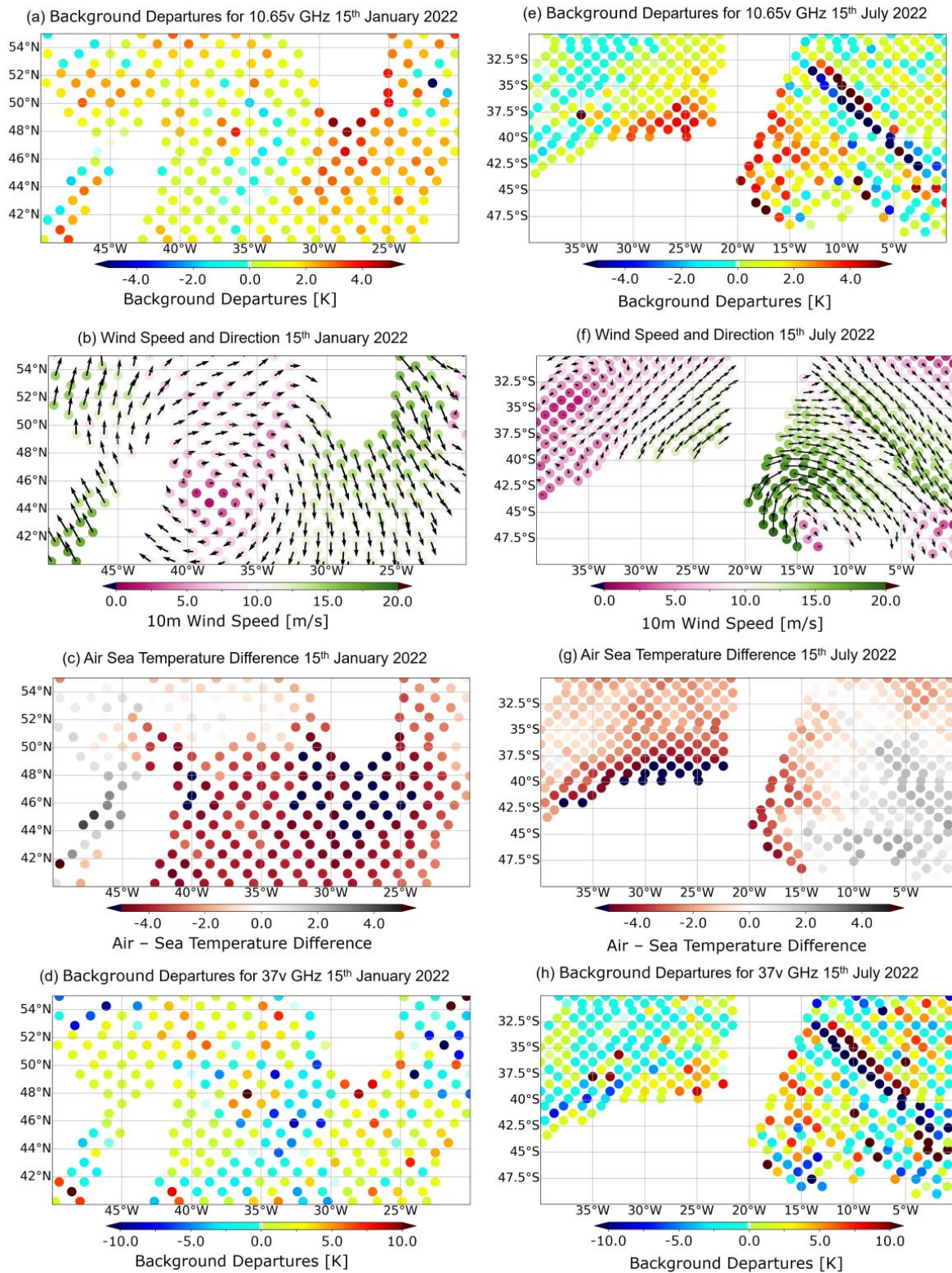Key to the later consideration of the SKT increments, it should be noted that large positive departures are

Figure 14: Regions potentially affected by residual CAOs at 10.65v GHz in (a to d) the Northern Hemisphere in January and (e to h) the Southern Hemisphere in July for the variables indicated.

seen in the Gulf Stream, particularly in the NH winter months, as illustrated in Figure 13(a-c). It is well-known that the Gulf Stream presents challenges in terms of modelling due to the steep, small scale SST gradients in the region and high variability (Roberts *et al.*, 2021; Deser *et al.*, 2010). This area can cause multiple issues in the simulations of MW imager radiances at any frequency, which is demonstrated by similar highly positive departures occurring in all AMSR2 channels (not shown). No further discussion is provided here as this will be considered in the SKT characterisation section below (see Section 3.4).

In addition to high positive departures, there are a few regions where highly negative departures can be seen. The most relevant of these to the later SKT increment discussion is those in the region of the equatorial currents (just south of the equator and most prominent in the 10.65v GHz channels). These are likely to be a result of errors in the SKT at these locations. Large negative departures are also apparent in the 6.9v GHz channel in July (Figure 13(a)) at about 50°N to the west of Canada and at 60°N to the east of Canada. In January for GMI (Figure 13(d)) large negative departures to the south of Japan can be seen. Currently, there is no proposed theory to explain these particular negative departures, however, they may be random errors in the model forecast potentially related to the over-estimation of the SKT or excessive rainfall.

Figure 15 shows the background departures for each newly added channel with the QC implemented for the months of January 2022 (a to c) and July 2022 (d to f). In these maps, we see both the CAO features as well as the SKT errors discussed for the single cycle maps shown in Figure 13. Those suspected to be related to errors in the input SKT are very similar to the SKT increments discussed later in Section 3.4, demonstrating the sensitivity of these channels to the SKT.

2.5 Impact on the Atmospheric Forecast system

The impact of introducing 6.9v and 10.65v GHz on other AMSR2 and GMI channels is shown in Figure 16. Here it can be seen that the mean of the departures (solid line) reduces for all channels previously assimilated over oceans (i.e. those above 10 GHz), however, the bias correction also changes (dashed line) and therefore it is not clear if this is an improvement. However, it is likely that these changes are attributable to changes in the relative humidity which has reduced in the mid-latitudes (30°N to 60°N and 30°S to 60°S) due to the inclusion of the 6.9v and 10.65v GHz channels (shown in Figure 17).

Note that the exact data sample used in the generation of Figure 16 varies slightly between the experiment where 6.9v and 10.65v GHz is active and that used as the reference which could impact the interpretation of these results. However, for the channels above 18.7v GHz, the number of observations is very similar between the experiments, which suggests that any change in the data used in the DA system is minimal.

For the 10.65v/h GHz channels an increase in the mean of the background departures is seen; this may be due to changes in the weighting given to observations in VarBC (Dee, 2004) due to changes in the assigned observation error. Now all observations over ocean are being actively assimilated in these channels with realistic observation errors, whereas previously only points over sea-ice were used with realistic observation errors, and the observation error in open ocean points was set to 50 K. Because VarBC minimises the observation-error weighted mean, rather than the unweighted mean that is shown in Figure 16, such apparent contradictions are possible. Most likely the bias correction is now less tightly constraining the sea-ice areas (where biases and observation errors are now both relatively large) and more appropriately constraining the open ocean (where biases were already small).

A small improvement due to the inclusion of the 6.9v and 10.65v GHz channels is the slight (but only just statistically significant) improvement in the upper tropospheric humidity channels, shown in Figure 18 for (a) ATMS and (b) CrIS for the Northern Hemisphere (NH). This could be due to real improvements
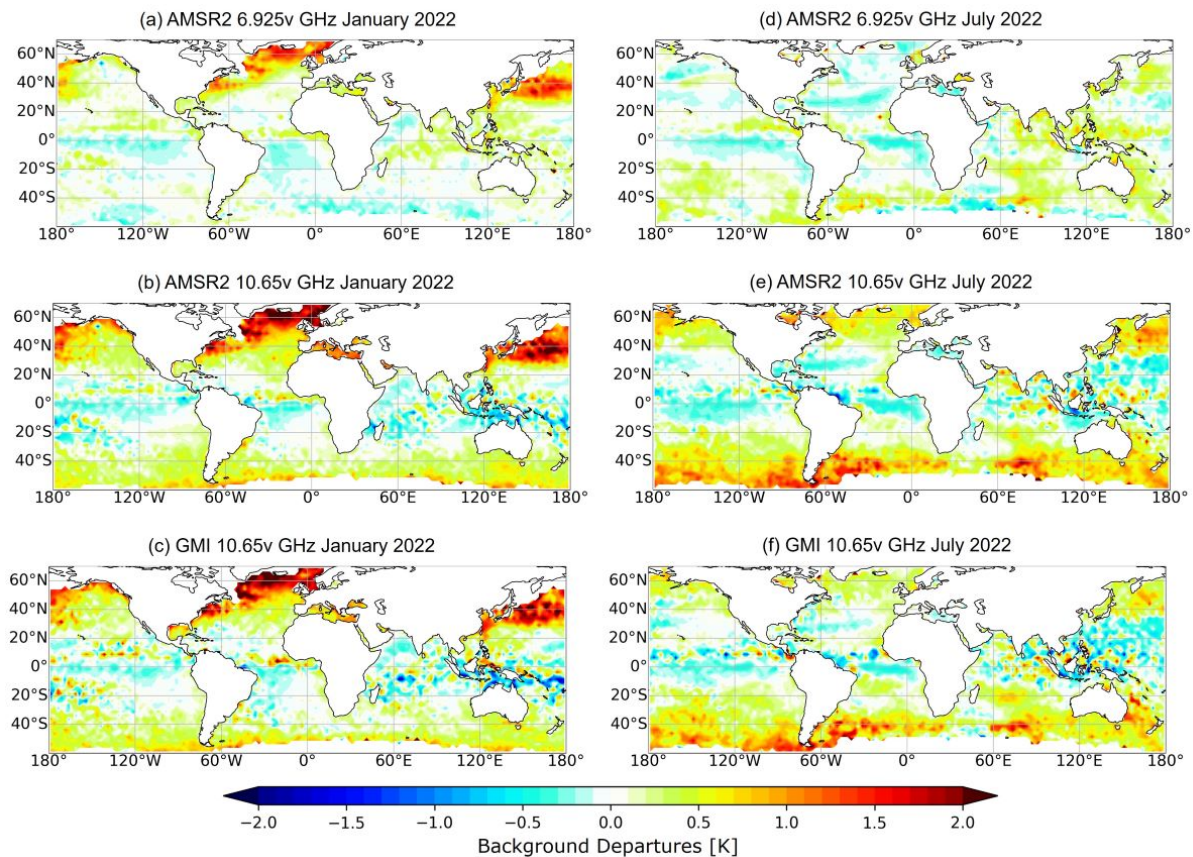
Figure 15: Global background departures for (a and d) AMSR2 6.9v GHz, (b and e) AMSR2 10.65v GHz and (c and f) GMI 10.65v GHz for the months indicated after the implementation of the QC.

in the representation of rain (due to the sensitivity of channels around 10 GHz to heavy rain) in this area.

The overall impact of adding 6.9v and 10.65v GHz to the atmospheric forecast system, both in terms of forecast scores and the background departures of independent observations, is neutral (with the exception described above). This firstly demonstrates that these highly surface sensitive channels are mostly decoupled from the atmospheric analysis and secondly that the lack of priority given to these channels up to now was justified in the context of an atmospheric forecast system.

3 Skin Temperature Increments

3.1 The Sink Variable Approach

The sink variable approach, referred to at ECMWF as the TOVS Control Variable (TOVSCV), has been used for many years to optimise the SKT associated with all observations processed under the clear sky route (currently all IR radiances plus the MW sounder ATMS) (ECMWF, 2021). Recent work has also offered the possibility of a 2D multi-sensor extended control variable (XCV) for SKT (Massart *et al.*, 2021, 2020; Massart, 2023). However, as discussed in the introduction (Section 1) neither TOVSCV nor XCV has yet before been activated for observations processed under the all-sky (clear and cloudy) route which covers most MW sounders and all of the MW imagers. Further, the XCV approach provides SKT
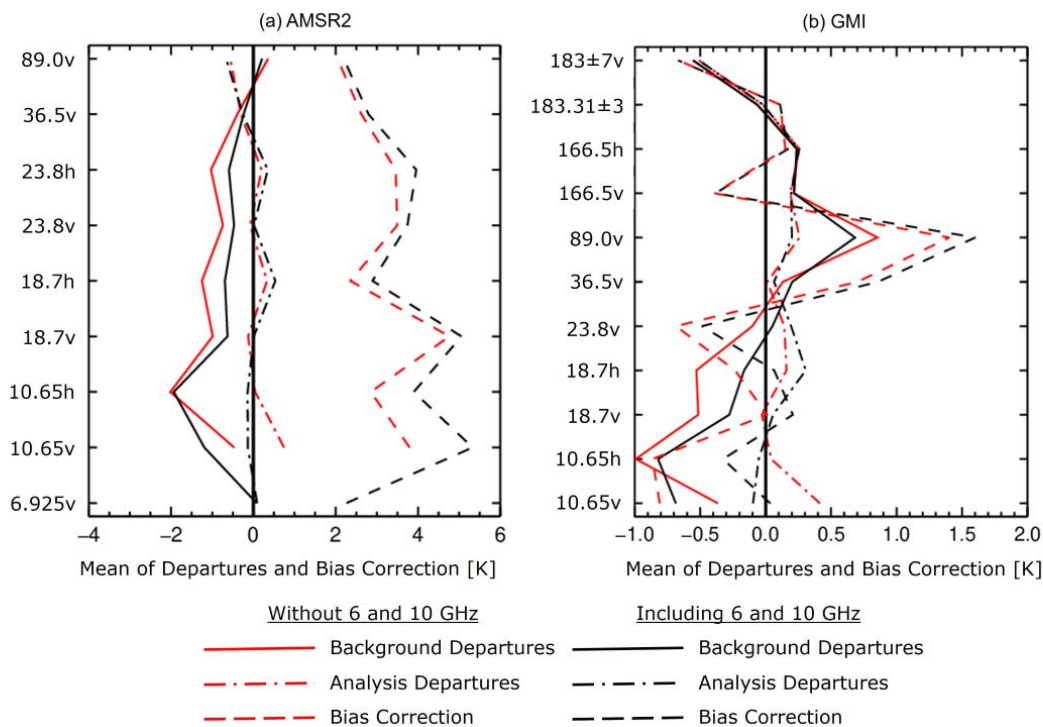
Figure 16: Mean background departures, analysis departures and bias correction globally per channel for (a) AMSR2 and (b) GMI with and without the 6.9v and 10.65v GHz channels activated for the periods 2021-12-07T00 to 2022-02-28T12 and 2022-06-07T00 to 2022-08-31T12. Note, these plots contain all actively used in the DA system for each experiment and hence the experiment where 6.9v and 10.65v GHz is activated and the reference may contain a different sample of data.

information on an hourly basis (Massart *et al.*, 2020), whereas the approach followed here allows for SKT increments to be made at the time of the observation; as SKT changes rapidly due to the cool skin effect, hourly information may not be sufficient.

The TOVSCV can be summarised as adding the SKT (in observation space) to the control vector to allow the SKT to be optimised along with the atmospheric model fields. As per the model fields, the SKT is adjusted to provide the optimal estimate for that field of view (i.e. across all channels for a sensor) taking into account the assigned SKT background errors, which are set to 1.0 K over ocean (ECMWF, 2021) (note, varying this value is tested in Section 3.3.2). Unlike the increments for the atmospheric variables, the SKT increments are dismissed at the end of each cycle and the SKT is reinitialised from the SST provided by external data products. Section 2.2 of Massart *et al.* (2020) provides a complete mathematical description of the TOVSCV and should be referred to for further details. On the technical level, the code for allowing a TOVSCV for all-sky microwave radiances was added through the sea-ice sink variable work (Geer, 2024a) and then extended to allow SKT estimation. The choice of SKT or sea-ice estimation is mutually exclusive, with SKT estimation taking place only for SKT ≥ 277 K and sea-ice where SKT < 277 K.

For this work, all MW imagers and sounders used in the ECMWF-IFS were initially considered, however preliminary work found that the sink variable approach for SKT is most promising if there is a 6.9v or 10.65v GHz channel available on the sensor (see Section 3.2). Therefore, the work shown here is limited to the application of the SKT sink variable to the AMSR2 and GMI MW imagers where these
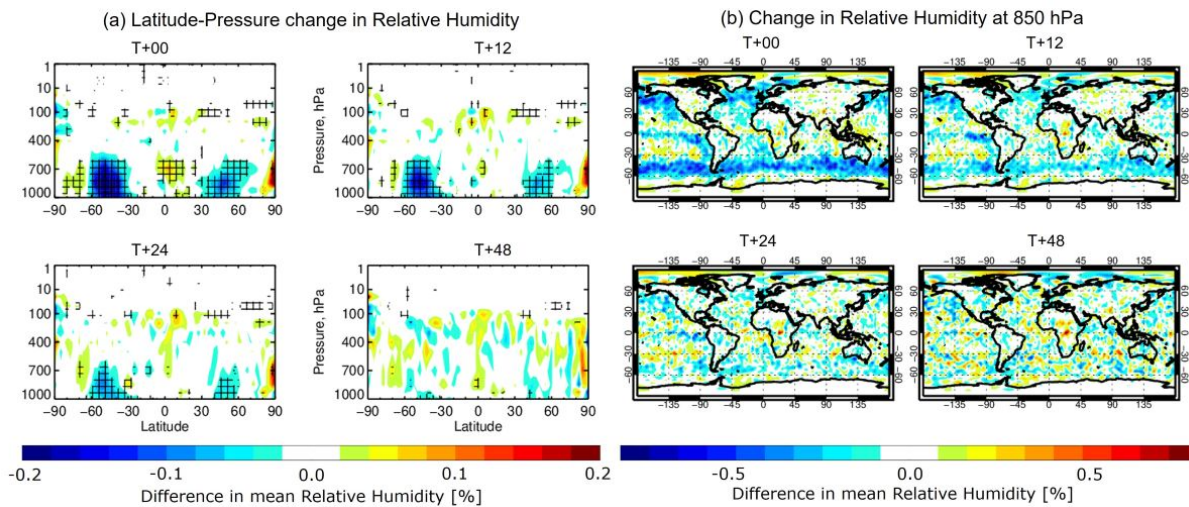
Figure 17: Change in relative humidity due to the introduction of the 6.9v and 10.65v GHz channels for (a) averaged by latitude and pressure and (b) averaged geographically for at 850 hPa. Data from the periods 2021-12-07T00 to 2022-02-28T12 and 2022-06-07T00 to 2022-08-31T12. Note that the cross-hatching in (a) indicates point statistical significance as described in Geer (2016), however such testing is not applied to (b).

channels are available. Note, MWRI is not included as it is not currently operationally in the ECMWF-IFS (Scanlon *et al.*, 2023).

3.2   Sensitivity of MW Channels to Skin Temperature

The use of passive MW radiometers for SST retrievals has been ongoing since the launch of the Scanning Multi-channel Microwave Radiometer (SMMR) in 1978, with the first global SST product being produced from Advanced Microwave Scanning Radiometer for EOS (AMSR-E) in the early 2000s (Nielsen-Englyst *et al.*, 2021; Minnett *et al.*, 2019). Over the years, various combinations of frequencies have been used for these retrievals depending on the channels available on the sensors, i.e. the SST retrieval algorithms for AMSR-E (Wentz *et al.*, 2005) and AMSR2 (Shibata, 2013; Alsweiss *et al.*, 2017) have included 6.9v GHz while those for Tropical Rainfall Measuring Mission (TRMM) Microwave Imager (TMI) and GMI have included 10.65v GHz as their lowest frequency. Recently, Nielsen-Englyst *et al.* (2021) demonstrated that the best 3-channel combination for SST retrieval is 6, 10 and 18 GHz (in the context of the upcoming Copernicus Imaging Microwave Radiometer (CIMR) mission (Donlon *et al.*, 2023)) and Pearson *et al.* (2018) showed that the 6.9v and 7.3v GHz channels of AMSR2 provided the most information content for SST. In each of these studies, higher frequencies are used to mitigate for other effects, including ocean surface roughness, i.e. waves (10 and 18 GHz) and atmospheric water vapour (23 and 37 GHz) (Le Vine, 2017).

In addition to the various SST products which include 6.9v/h or 10.65v/h GHz channels, a recent study by Kilic *et al.* (2021) demonstrated that the frequency sensitivity to SKT (referred to in the paper as SST) varies depending on the conditions under which the observations are being made (see Figure 3 of Kilic *et al.* (2021)), with the peak sensitivity to SKT at frequencies ranging between 2 and 4 GHz (in the Arctic ocean) and 5 and 7 GHz (in the tropics). It is also generally accepted that channels in this
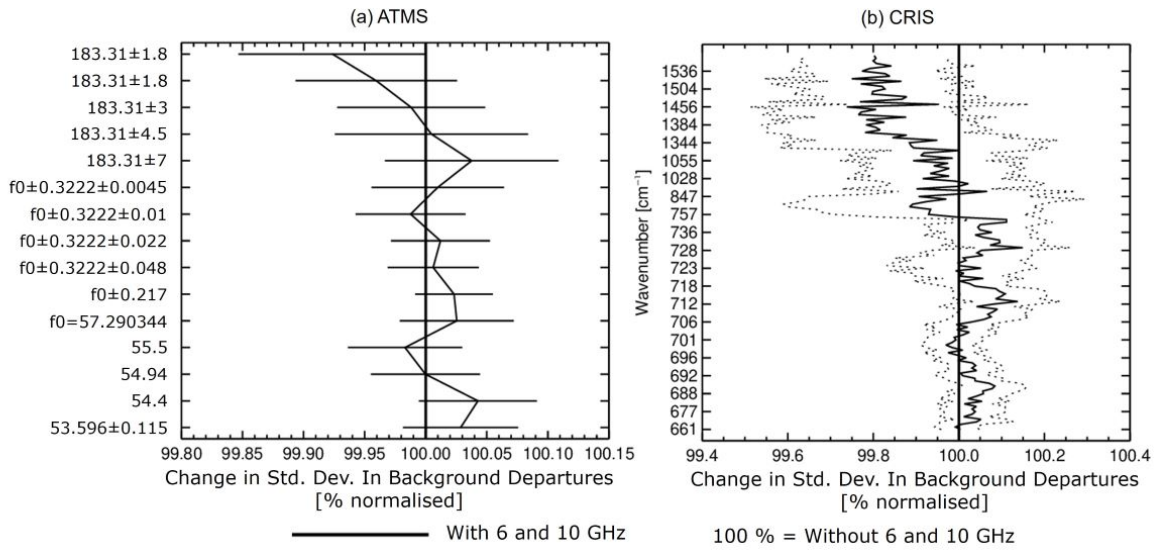
Figure 18: Relative change in the standard deviation of the background departures due to activating the 6.9v and 10.65v GHz channels for (a) ATMS and (b) CrIS for the periods 2021-12-07T00 to 2022-02-28T12 and 2022-06-07T00 to 2022-08-31T12 over the Northern Hemisphere.

frequency range are required for the accurate retrieval of SST (CEOS, 2020)[4].

For the 6.9v/h and 10.65v/h GHz channels on AMSR2 and GMI, both v- and h-polarisations are available, however, here only the v-polarisation is used as h-polarised channels are more sensitive to the atmosphere (e.g. Kilic *et al.* (2023)) and to changes in emissivity. Progress towards improving the modelling of low frequency h-polarisation channels is underway and it is noted that the performance improves for 10.65h GHz on GMI for the new SURFEM-ocean radiative transfer model when compared to the previously used FASTEM-6 model (Geer *et al.*, 2024). It is also noted that while no explicit discussion of the usage of h-polarised channels for SST retrievals has been found in the literature, it has not been used in the operational generation of the AMSR2 SST product (Shibata, 2013). It is hoped to test the use of h-polarised channels in the future in the context of the generation of SKT increments.

Within the framework of the ECMWF-IFS, an analysis has been undertaken to determine the sensitivity of the observed TBs (up-welling from the earth) to the input SKT under clear-sky conditions at different frequencies. Figure 19(a) shows a scatter plot of the observed TBs from v-polarised channels between 6.9v and 89.0v GHz against the input (background) SKT generated from the input SST products and interpolated to the date and time of the observations. Figure 19(b) shows the modelled emissivity against the initial SKT for the same channels. The following equations are aimed at explaining some of the key features seen in these plots.

In the MW range, ignoring scattering, assuming specular reflection at the surface and representing radiances as TBs assuming linear dependence of the two, the TBs at TOA (T_b) can be described as follows:

$$T_b = T_{\text{top}}^{\uparrow} + \tau\varepsilon(T_s)T_s + \tau(1-\varepsilon(T_s))T_{\text{bot}}^{\downarrow} \qquad (3)$$

---

[4]Note that there has been some discussion in the literature on the sensitivity of L-band radiometers to SST (Li *et al.*, 2019), however this is not considered further here as there are currently no L-band radiometer radiances assimilated into the ECMWF-IFS.
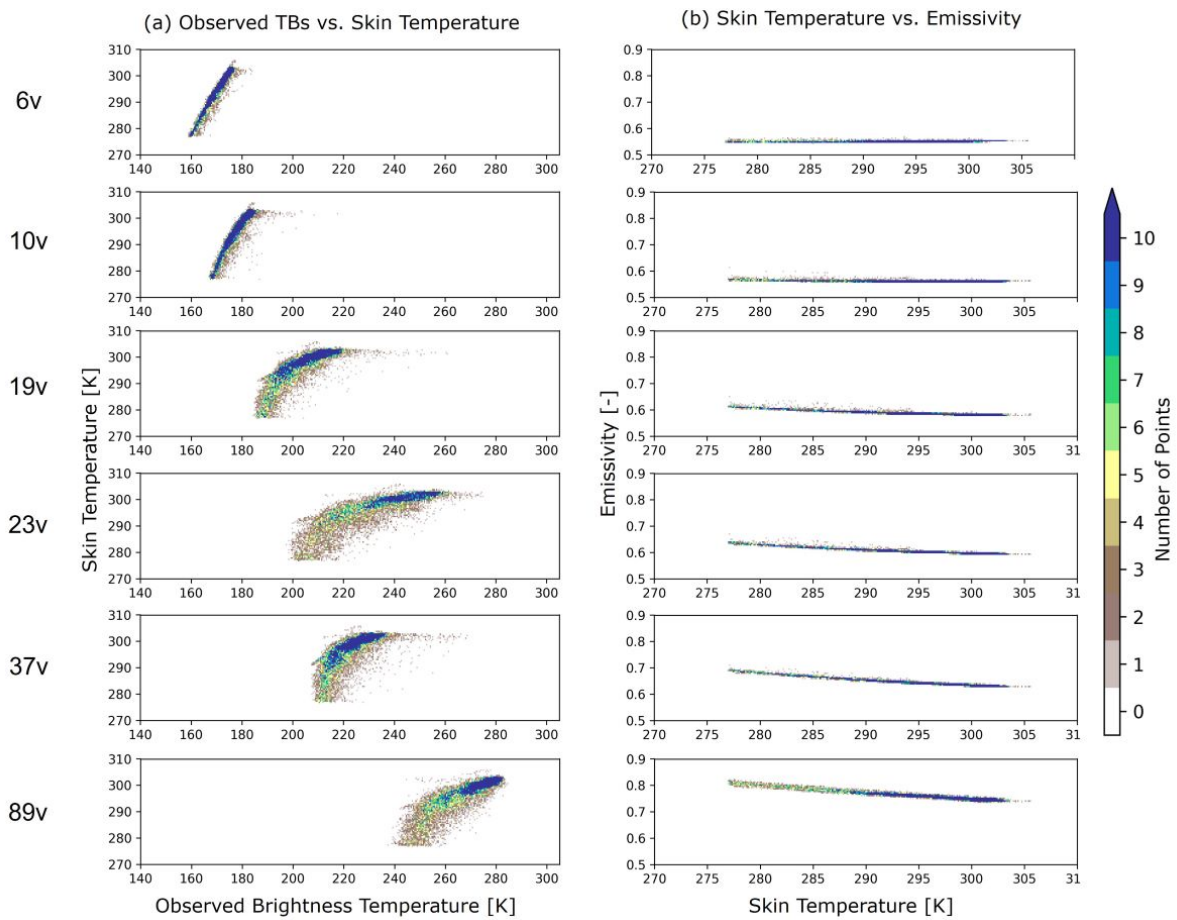
Figure 19: Relationship between SKT and (a) observed TBs from AMSR2 (frequencies and polarisation indicated) and (b) emissivity for one cycle (2022-06-01T12) under clear-sky conditions.

The first term, $T_{\text{top}}^{\uparrow}$ is the up-welling radiation which has not interacted with the surface. The second term describes the radiation emitted by the surface with an emissivity of $\varepsilon(T_s)$ and a temperature of T_s, noting that the emissivity is itself temperature dependent as illustrated in Fig. 19. This surface emission is attenuated by the atmosphere according to the surface-to-space transmittance, τ. Finally the third term is the radiation reflected from the surface (where the fraction reflected is dependent on the emissivity following Kirchhoff's law, $(1 - \varepsilon(T_s))$ where the downwelling TB at the bottom of the atmosphere is $T_{\text{bot}}^{\downarrow}$ and the surface-reflected radiation is again attenuated by the atmosphere with a surface-to-space transmittance of τ.

It can be seen in Figure 19(a) that for 6.9v and 10.65v GHz, the dependence of the observed TBs on SKT is mostly linear and there is little dependence of the emissivity on the SKT. Note that a similar finding for 6.9v and 10.65v GHz is presented in Gentemann *et al.* (2010) but showing a slightly non-linear response at very low SSTs which is not apparent in our results. In the case that emissivity is constant, we can substitute $\varepsilon((T_s) \simeq \varepsilon$ into Eq. 3. Further, if the atmospheric absorption is weak, as is generally the case at low frequencies, $\tau \simeq 1$. The derivative of Eq. 3 with respect to T_s is then simply:

$$\frac{\delta T_b}{\delta T_s} \simeq \varepsilon. \tag{4}$$

For the higher frequencies a more complicated picture is apparent: for SKTs under 290 K there is little to no response of the observed TBs to the SKT, however, as the SKT increases, a linear response starts to emerge. In the cases where the SKT is higher, this is often associated with higher TCWV (not shown) as these represent areas such as the tropics and subtropics. This results in stronger absorption of radiation in the atmosphere and hence a lower surface-to-space transmittance, τ. This then leads to stronger absorption and emission in the atmosphere and hence higher TBs in these areas (both $T_{\text{top}}^{\uparrow}$ and $T_{\text{bot}}^{\downarrow}$ increase due to higher water vapour and temperature in the lower troposphere, semi-independently of the SKT). This means that some of the relation between high SKTs and high TBs is an indirect effect, i.e. a correlation through high TCWV.

In terms of the SKT increments, Figure 19 demonstrates that although SKT information could be gained, directly or indirectly, from those channels affected strongly by the atmosphere (18.7 GHz and above), the most direct information is obtained when the 6.9v and 10.65v GHz channels are used. Figure 20 gives an example of instantaneous SKT increments for the tropical and sub-tropical region of the Atlantic between Africa and South America for the case where (a) only the 18.7v/h GHz and above channels are used and (b) where 6.9v and 10.65v GHz are included for AMSR2. To make these plots comparable and ensure that the difference in signal is only from the use of 6.9v and 10.65v GHz channels, the experiment including these channels has been initialised from the background of that in Figure 20(a) using a variational bias correction which has been spun-up including 6.9v and 10.65v GHz. Here it can be seen that for the case of the higher frequencies only (panel a) the increments are much smaller than those for the case where the lower frequency channels are included (panel b). Although there are many increment patterns in common, it is only when the lower frequencies are used that a discernible pattern can be seen relating the south equatorial current, which is not seen when these channels are not used.

One of the main concerns of activating the SKT sink variable is that it brings the potential for atmospheric information, or sensor biases such as those for MWRI shown in Scanlon *et al.* (2023), to be aliased into the SKT increments. Where the SKT error is adequately constrained (discussed further in Section 3.3.2), the potential for this effect should be minimised. Figure 20 also shows that the inclusion of 6.9v and 10.65v GHz helps to minimise the impact of such effects and demonstrates that with these channels included, the SKT increments can be more easily related to features at the surface.
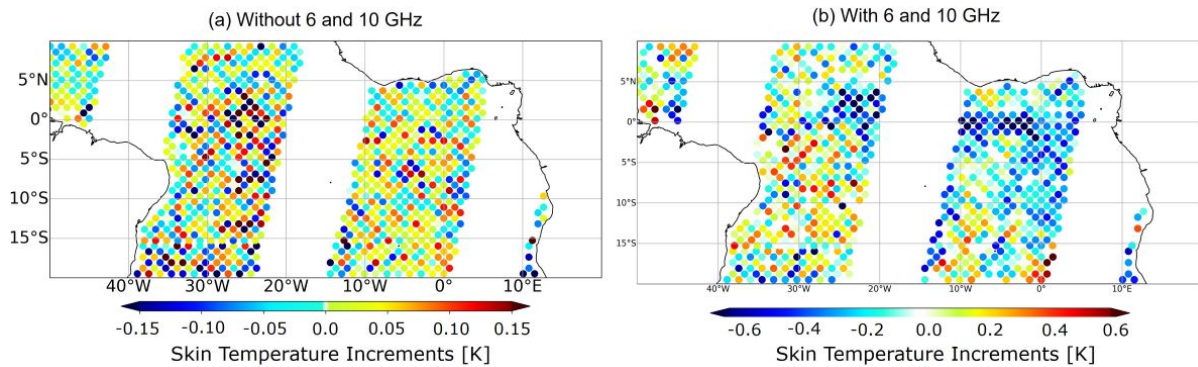
Figure 20: SKT increments generated for the 2022-06-02 0Z cycle (21h to 09h) for AMSR2 when using (a) only those channels above 18.7 GHz and (b) including the 6.9v and 10.65v Ghz channels in addition to those above 18.7 GHz. The experiment shown in (b) has been initialised from the background of the experiment in (a) to ensure comparability.

3.3 Configuration of the Skin Temperature Experiments

3.3.1 Changing the 6.9v and 10.65v GHz Observation Errors

As discussed in Section 2.3, the actual errors for the 6.9v and 10.65v GHz channels are well below the error model used by default for these channels. Particularly as the aim is to only use these channels for the generation of SKT increments, it is possible to more closely fit the error model to the actual standard deviation of the background departures.

The proposed error model is shown for both seasons in Figure 21 (dashed line) with data from experiments where these errors have been implemented (solid line and histogram). It can be seen that the standard deviation of the background departures fit the proposed model closely (as intended), however, it is noted that for the NH winter months (December, January, February, i.e. DJF) (d to f) for AMSR2 10.65v GHz, the fit is extremely close for the last bin (0.7 to 1.0). This is considered acceptable as there are very few observations in this region compared to lower cloud values.

The use of these smaller observation errors results in much larger SKT increments, as can be seen in the histograms in Figure 22 for (a) AMSR2 and (b) GMI in the NH summer (June, July, August, i.e. JJA). The SKT increments from the new observation error models (shown in red) have a much larger magnitude and spread for both AMSR2 and GMI. This brings the magnitude of the SKT increments in line with those seen for the infra-red observations which are currently generated operationally. Full analysis of the SKT increments is provided later in Section 3.4.

The use of the new observation errors has very little impact on the atmospheric forecast scores (not shown) which is as expected as these observations are primarily sensitive to the surface. It is difficult to assess the change in the fit of AMSR2 and GMI observations in the context of the SKT sink variable as the majority of the differences, if not all, will be related to how the change in the errors affects the use of the 6.9v and 10.65v GHz and not the impact in terms of the change to the SKT increments. Therefore, no further assessment of these new observation errors can be made here. However, it is noted that these larger SKT increments may result in a more significant impact within the coupled DA system and this will be further tested in that context.
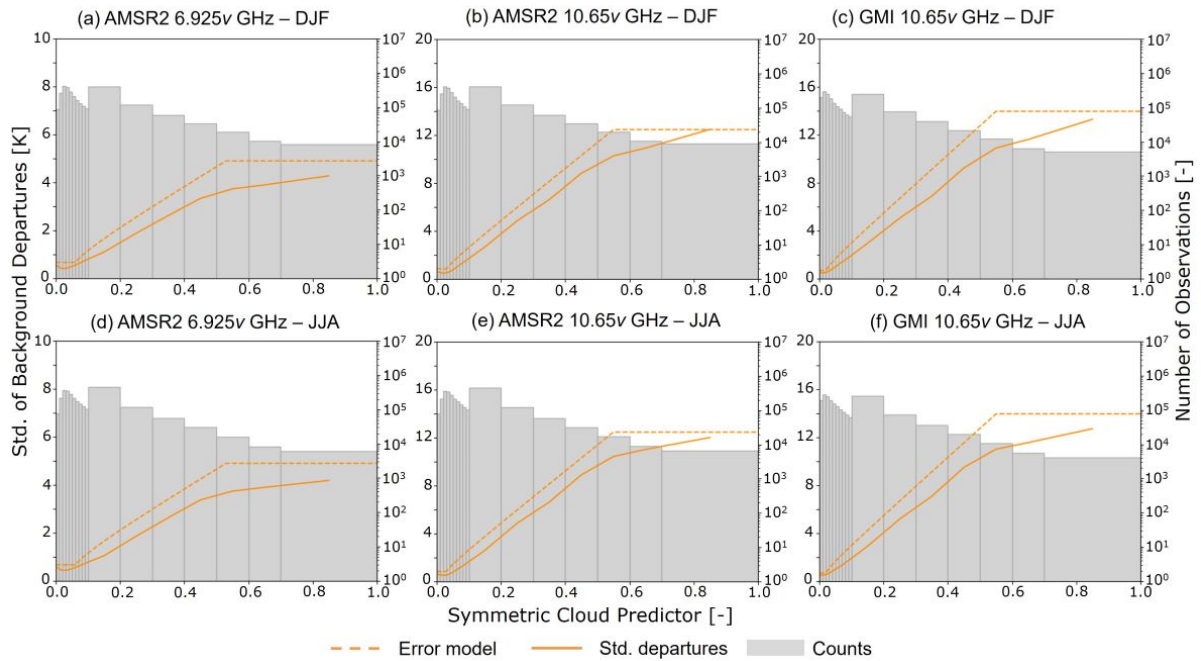
Figure 21: The updated error model (dashed line) and the standard deviation of background departures (solid line) associated with (a and b) AMSR2 6.9v and 10.65v GHz (c) GMI 10.65v GHz for 2021-12-07T00 to 2022-02-28T12, and the same (d, e, and f) for 2022-06-07T00 to 2022-08-31T12. Counts are shown in gray, with the histogram widths indicating the bin width used. The cloud proxy used is based on the difference between the two polarisations of the 37 GHz channel.
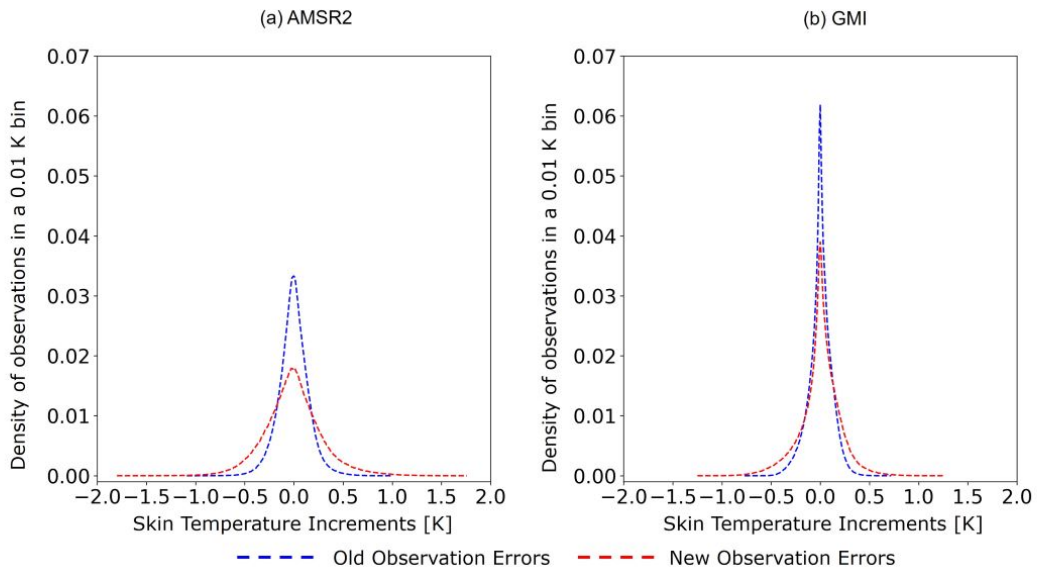

Figure 22: Distribution of SKT increments using different observation errors for 6.9v and 10.65v Ghz for (a) AMSR2 and (b) GMI for the period 2022-06-07 to 2022-08-31 binned into 0.01 K bins.
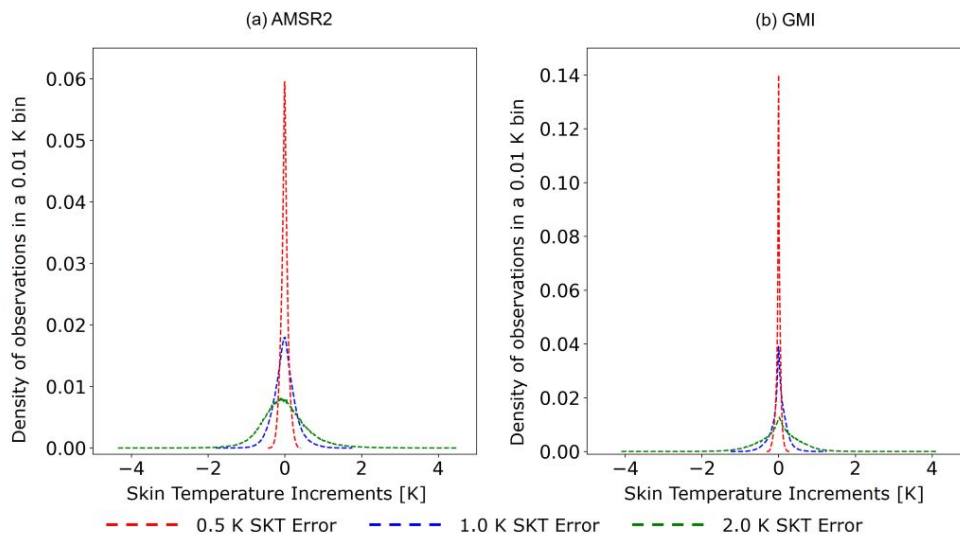
Figure 23: Distribution of SKT increments using different fixed SKT background errors (0.5 K, 1.0 K and 2.0 K) for (a) AMSR2 and (b) GMI for the period 2022-06-07 to 2022-08-31 binned into 0.01 K bins.

3.3.2   Changing the Background Skin Temperature Error

The baseline configuration of the SKT experiments uses a background SKT error of 1.0 K at all times and locations (and this is what has been used in all Figures relating to the SKT increments presented up to now). There has been some work undertaken to use SKT errors derived from the Ensemble Data Assimilation (EDA) spread of the SKT as described in Massart *et al.* (2020) which stated that the EDA spread over oceans is 0.27 K $\pm$ 0.1K. Whilst this method allows for a spatially and temporally varying error, Massart *et al.* (2020) concludes that the method requires more tuning prior to use for their work and the same approach is taken here, with only fixed errors considered in the testing.

Three options have been used for the SKT error: 0.5 K, 1.0 K and 2.0 K; these are tested using the new observation errors for 6.9v and 10.65v GHz discussed in Section 3.3.1. The distributions of the resulting SKT increments are shown in Figure 23. As expected, a much wider distribution with higher values is seen when the SKT increments are allowed to vary the most using the 2.0 K SKT background error, with the smallest values of SKT increments resulting from the lowest SKT background error (0.5 K).

Figure 24 shows the impact on the analysis departures of using the different SKT error values against a baseline of the SKT increments not being active. It can be seen that turning on the SKT increments improves the analysis departures for the surface sensitive channels in both 6.9v and 10.65v GHz, which is expected as the analysis departures are the only departures in which the updated SKT is used. For AMSR2 the atmospherically sensitive channels do not change, however, for GMI, the 18.7v/h, 23.8v and 36.5v GHz channels degrade by up to 1% (statistically significant). It is not thought this is a strong atmospheric impact as there is little change in the skill of the atmospheric forecast between the SKT options and the control experiments (not shown). Potentially, this difference in the response of these higher frequency channels between AMSR2 and GMI is related to the absence of the 6.9v GHz on GMI. This plot also demonstrates that there is not much sensitivity to the SKT above 18.7v/h GHz as the response of these channels is very similar with each SKT error option.

For both AMSR2 and GMI, Figure 24 shows the 2.0 K SKT error achieves the best fit in terms of the
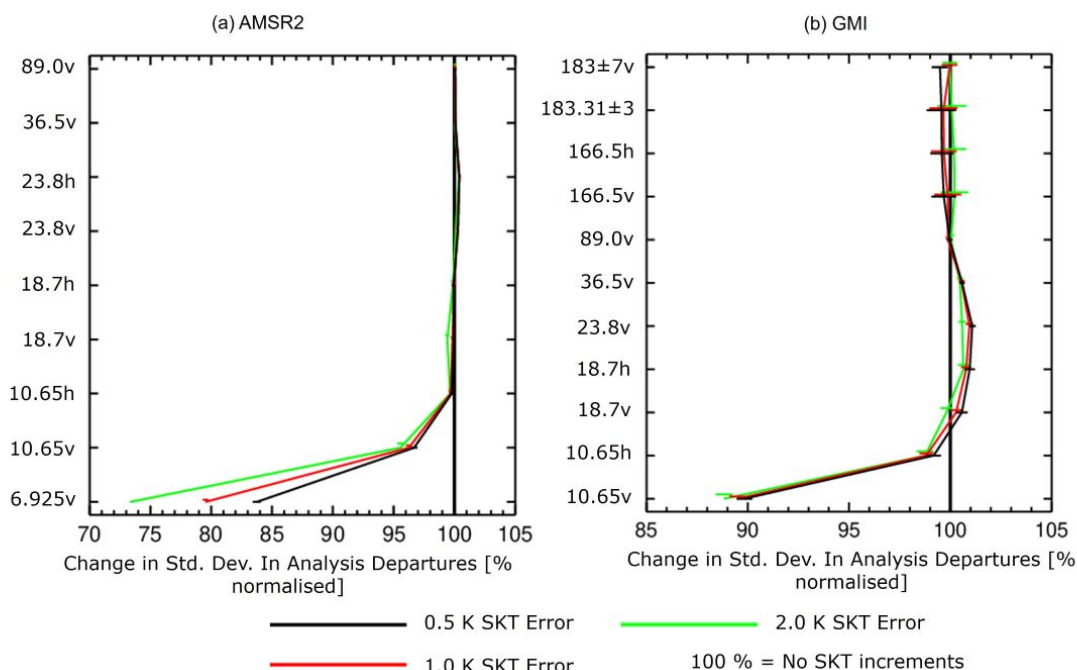
Figure 24: Relative change in the standard deviation of the background departures when using the different fixed SKT errors indicated (0.5, 1.0 and 2.0 K) for for (a) AMSR2 and (b) GMI for the periods 2021-12-07T00 to 2022-02-28T12 and 2022-06-07T00 to 2022-08-31T12.

analysis, however, the increments provided by this error are large and perhaps somewhat unrealistic. Figure 25 shows the increments averaged over July 2022 for each error option for the Eastern Tropical Pacific (ETP) and polewards. This area contains Tropical Instability Waves (TIWs) with a wavelength of approximately 1000 km; these are discussed further in the context of the SKT increments in Section 3.4. The SKT increments in this area are generally negative, as the SKT sink variable tries to cool the ocean surface to ensure the TIWs are located in the right place for the exact time of the MW observations. Hence, for the different error options, it is expected that some large scale cooling is present in these areas.

In Figure 25, the main difference between the error options is the magnitude of the SKT increments (note the colour bar ranges), as per Figure 23. For the spatial patterns, the SKT increments in the TIWs are persistent between each SKT error option, providing confidence that these are a real signal. For the area to the south of these waves (10° S and below) large scale warming of the oceans can be seen which is partially consistent between the plots, except for the 2.0 K SKT error where the increments appear much larger in contrast to the cooling of the TIWs when compared to the 0.5 K and 1.0 K SKT error. For this reason, it is thought that the 2.0 K SKT error provides too much freedom to the system and the increments produced are not considered meaningful, hence the 1.0 K error will be used. Further justification for the SKT background and observation error choices will come in future as part of coupled DA system developments.

3.3.3   Using Surface-Only Observations

As the aim of this work is to improve the SKT and not the atmospheric analysis, there is a possibility to generate SKT increments at all locations on the 40 km superobbing grid, rather than just those currently
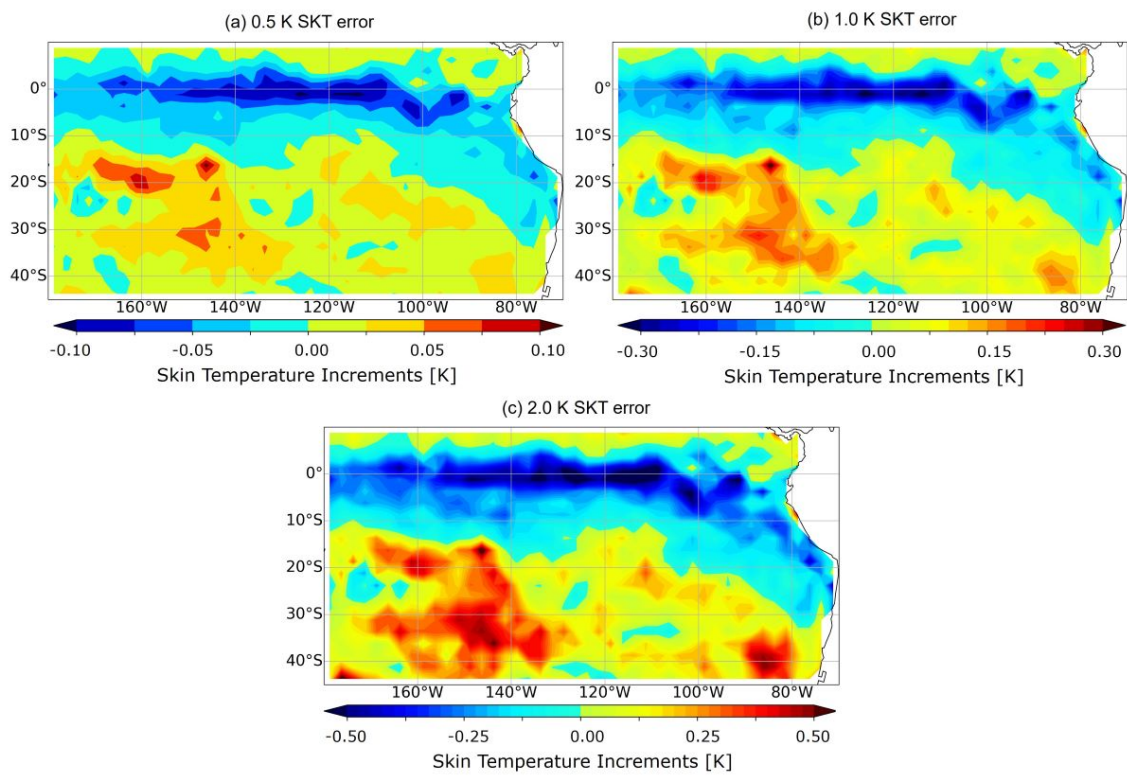
Figure 25: Skin temperature increments for the east tropical pacific region and polewards using different background SKT errors: (a) 0.5 K, (b) 1.0 K and (c) 2.0 K. Data is averaged over 2022-07-01 to 2022-07-31 and gridded in 2.5° boxes. Note the colour bar scale changes between each plot.
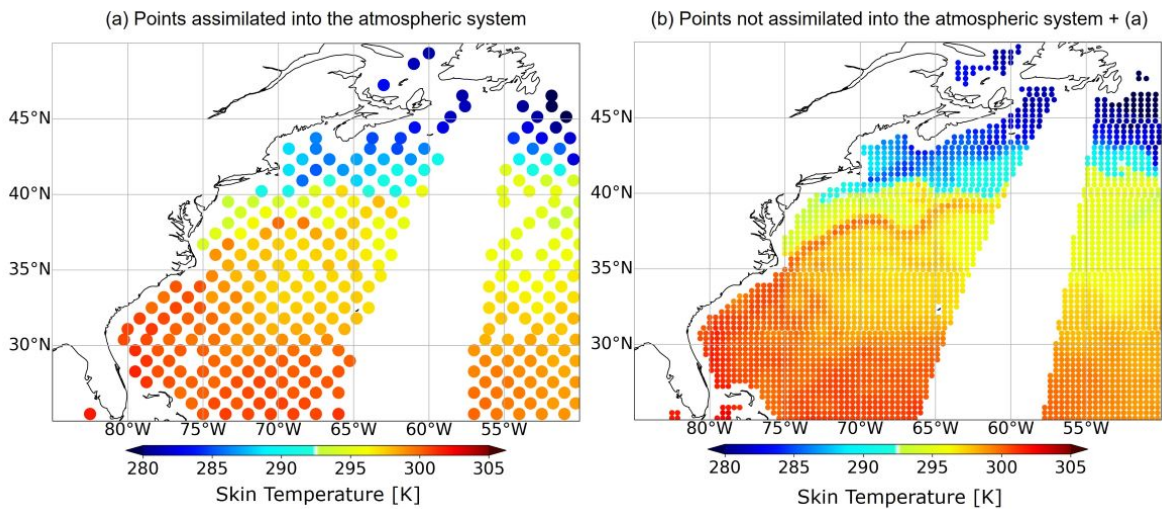
Figure 26: Modelled SKT where (a) only those points used in the atmospheric assimilation are shown and (b) all points are shown, even if they are not used in the atmospheric DA for the 2022-06-16 0Z cycle (21h to 09h).

used in the atmospheric analysis. Currently, due to suspected error correlations (Bormann *et al.*, 2011), only 1 in every 8 superobs is actively assimilated into the atmospheric DA system. In the recent sea-ice work, Geer (2024a), an approach was taken where the sea-ice concentration is estimated at all 8 superob locations and therefore the same approach is trialled here. For clarity, here the 7 of 8 superob locations not used in the atmospheric DA are referred to as 'surface-only' points.

The increase in the spatial density and the ability to discern small scale patterns when using these 'surface-only' superob locations is demonstrated for SKT in Figure 26 for the case of the Gulf Stream. Panel (a) show the points used in the atmospheric data analysis (1 in 8 of the superob locations) and (b) shows these points plus those that would also be available if the other 7 superob locations were used (i.e. the 'surface-only' points). The extra information provided by these observations allows a much clearer picture of the the positioning of the gulf stream as well as an indication of the gulf stream 'rings' which are large scale (100 - 300 km) eddies of cool water which form to the sides of the main current. This comparison demonstrates the clear utility of these 'surface-only' superob locations and the propagation of these additional observations into the ocean model as part of the coupled DA system would likely be beneficial.

An experiment was conducted to determine if SKT increments could be derived from these 'surface-only' observations. In theory, the use of these superob locations should not have any effect on the atmospheric analysis, however, it was found that they caused degradation in the upper tropospheric humidity, with the fits to both geostationary satellites and CrIS becoming worse (see Figure 27). In addition, the inclusion of these surface only points results in a significant and unrealistic improvement to the relative humidity and geopotential height (when using own-analysis verification) (not shown). It is thought that these issues are due to the extreme volume of extra data coming from only two instruments: for AMSR2 there is 250% more data for channels at 10.65v/h GHz and above and almost 800% more data for the 6.9v/h GHz channels; for GMI the use of surface only observations results in 300% more data for 10.65v/h - 89.0v/h GHz and between 500% and 700% for channels above this. This additional data is thought to have resulted in the DA system becoming unbalanced and over-fitting the model to the information provided by these two instruments (consistent with this explanation, on average, 29.6 iterations are required, over the three
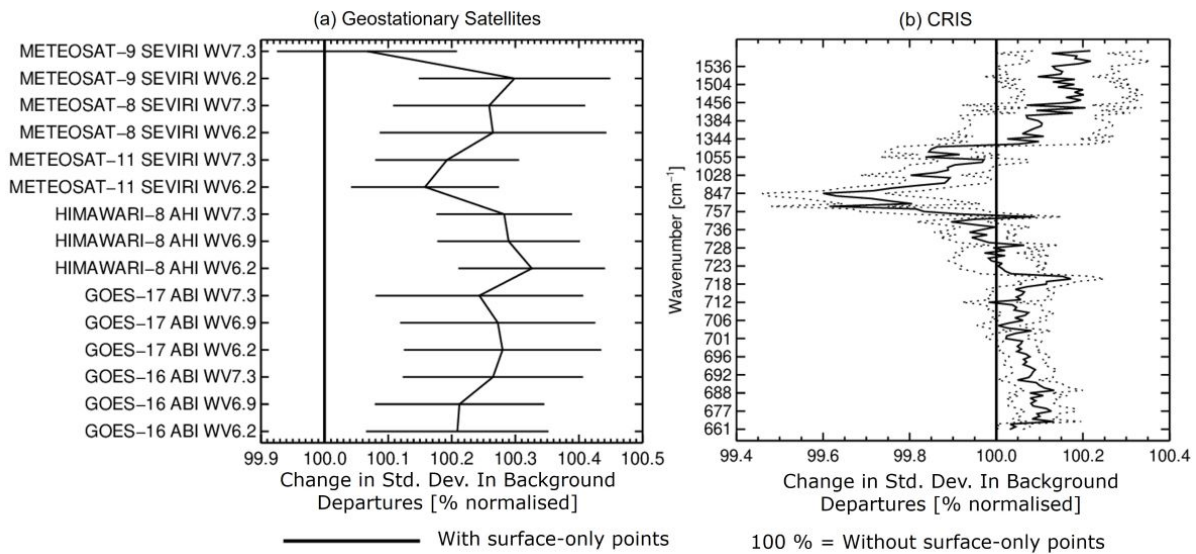
Figure 27: Relative change in the standard deviation of the background departures due to activating the SKT increments with surface-only observations for (a) geostationary satellites and (b) CrIS for the periods 2021-12-07T00 to 2022-02-28T12 and 2022-06-07T00 to 2022-08-31T12.

minimisations, to reach a solution compared to 28.0 when the 'surface-only' observations are not used).

Taking these issues into account, these surface-only points are only used in this work to provide confidence that the SKT analysis is working as intended (through visual inspection of small scale oceanic structures, as shown in Figure 26) and are not used in the full atmospheric forecast experiments nor recommended for inclusion in the operational system at this time. Re-tuning the DA system to be able to handle such large amounts of data from one sensor could be considered in the future to address this issue, for example when considering the use of such data in the coupled DA system.

3.4 Characterisation of the Skin Temperature Increments

3.4.1 Introduction

As previously discussed, the key factors influencing the accuracy of the SKT at the time and location of a particular MW measurement are: the timeliness and accuracy of the SST used to grow the diurnal cycle, the mismatch between the representative depth of the measurement and the modelled SKT, the accuracy of the cool skin and warm layer parameterizations used to model the SKT and finally the impact of any environmental factors not taken into account as part of the model including wind speed, heavy precipitation and sea surface salinity (see Shibata, 2013, for a discussion of such factors). The magnitude and spatial patterns of the increments generated by the DA system can be influenced by each of these factors as well as the sensitivity of the MW observation operator (RTTOV-SCATT, Bauer et al. (2006)) to the SKT (as discussed in Section 1).

Keeping this in mind, the spatial and temporal patterns of the SKT increments are discussed in the following section, noting that it is not possible to disentangle the effects of each of these factors. The results presented here are generated using a 1.0 K SKT error and the updated observation errors for 6.9v and 10.65v GHz, without the surface only SKT increments active, as per Section 3.3.
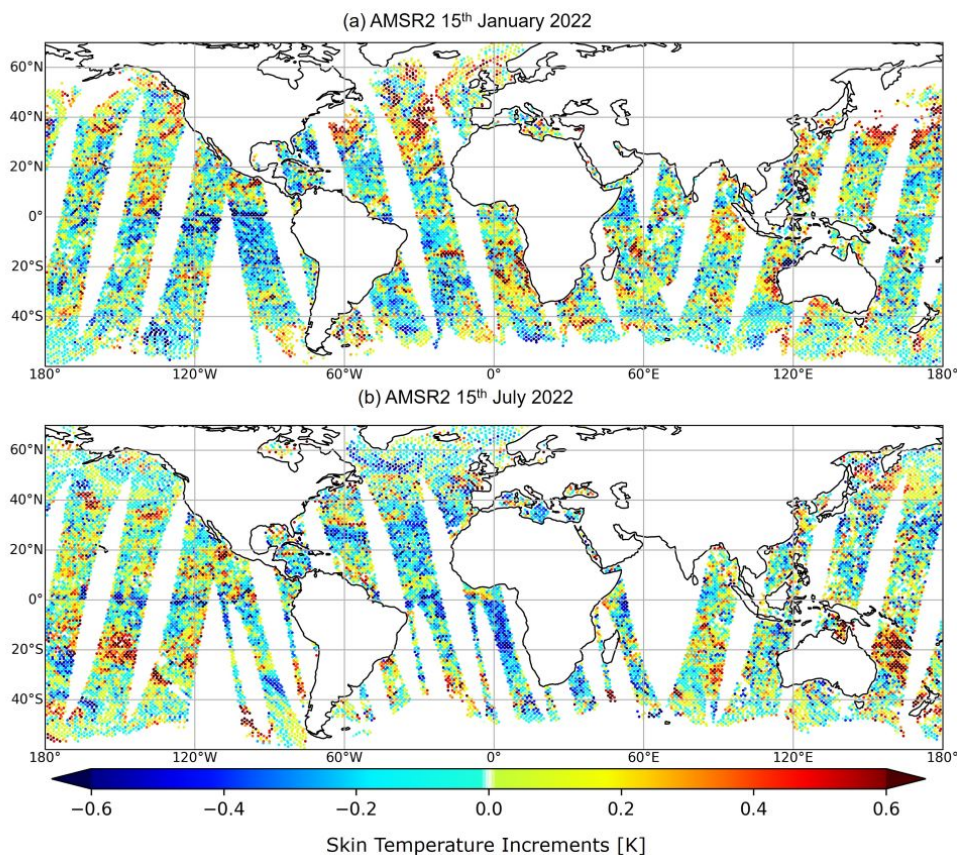
Figure 28: Skin temperature increments for a single cycle for AMSR2 for (a) 2022-01-15T12 and (b) 2022-07-15T12. The increments shown are only those which include the use of the 6.9v GHz channel. Note the data loss in the SH is a result of the sun-glint screening implemented to support the activation of the 6.9v and 10.65v GHz channels.

3.4.2   Spatial Patterns

SKT increments for a single cycle of AMSR2 are shown in Figure 28 for two dates and for monthly averages split by day-time and night-time using the solar zenith angle (where night-time is taken as an observation where the solar zenith angle is below 0°) are shown in Figure 29. The monthly means will be discussed further later in this section in the context of the differences between day and night-time observations and seasonal differences; for now they are used to confirm the persistence of patterns seen in the single cycle maps.

The most striking feature which is consistent between the dates in the single cycle maps is the large scale cooling at the equator in a meandering pattern that is reminiscent of TIWs that form along the equatorial cold tongue (e.g. Wentz *et al.*, 2000) in the ETP. This is a known area of high variability on short (tens of days) to long ($\geq$ 5 years) timescales (Bulgin *et al.*, 2020; Deser *et al.*, 2010). The long term persistence of the cooling patterns across seasons is highlighted by the monthly maps in Figure 29. The representation of the Peru eastern boundary current and its equatorial extension is a known deficit of the OCEAN5 product which is used as the input SST in this region; see Figure 18 of Zuo *et al.* (2019) which shows a warm bias of about 0.2 K in this area when compared to the European Space Agency (ESA) Climate Change Initiative (CCI) SST product. Therefore this is a key indicator that the SKT
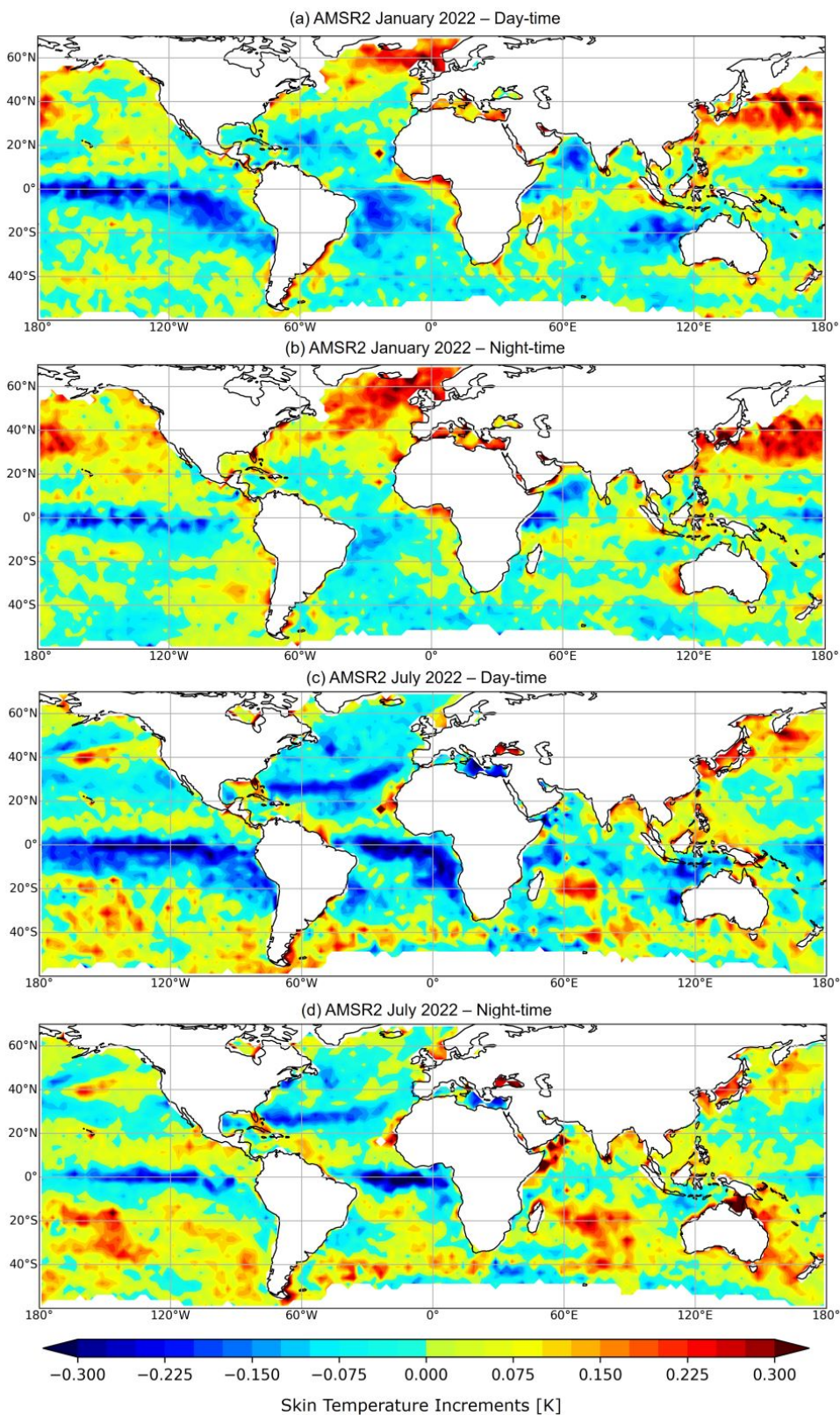
Figure 29: Monthly average of SKT increments for AMSR2 for (a) January 2022 day-time only observations, (b) January 2022 night-time only observations, (c) July 2022 day-time only observations and (d) July 2022 night-time only observations.

increments are working as expected to correct issues with the input SST products by exposing it to up-to-date observations of the surface. It is also noted that Wentz *et al.* (2000) demonstrated that these large TIWs can be detected using lower frequency MW channels which strengthens the case for the inclusion of 6.9v and 10.65v GHz for the SKT increments work. The signal in this region is further explored in the temporal analysis (Section 3.4.3).

A similar cooling pattern is also seen in the Eastern (Benguela) boundary current in the tropical Atlantic and extending along the equator, where also OCEAN5 appears to have a small positive bias (see Figure 18 of Zuo *et al.*, 2019). There is also a cooling pattern in the north Atlantic between Spain and Florida in July. Both of these features are much weaker (and the latter non-existent) in January. Note that the latter feature is not thought to be associated with the main ocean currents and is also explored further in the temporal analysis (Section 3.4.3).

In addition to the cooling features, the single cycle maps for AMSR2 show large scale warming in January in the North Atlantic and the North West Pacific and in July in the South Atlantic which is thought to be a residual signal from the previously discussed CAOs and emissivity issue when including in 6.9v and 10.65v GHz (see Section 2.5 for a discussion of CAOs and Section 3.4.3 for a discussion of how these impact the SKT increments over time). Again, these patterns are also seen in the monthly means in Figure 29 and have a wide-spread impact. This highlights the importance of addressing these signals prior to inclusion of the data into the coupled DA system to inform the ocean model.

Another feature of interest is the high magnitude warming seen in the South Pacific Convergence Zone (SPCZ) to the east of Australia. This warming signal is seen sporadically and will often last for several days at a time, for example the one shown here lasts between 2022-07-13 and 2022-07-16. The signal appears only in the night-time overpasses which is confirmed by the large scale warming seen in this area for the monthly average of July at night. The appearance of this signal only in night-time observations indicates that it is likely related to a deficiency in the input SST product or in the characterisation of the SKT close to the minima of the daily cycle. The origin of this signal is yet to be confirmed and will be further investigated in the context of the coupled DA system where the impact on the SST of these increments can be compared to in-situ measurements.

In addition to the signals seen in the single cycle maps, the monthly means (Figure 29) offer the opportunity to study the persistent signals as well as the average signal from day-time and night-time overpasses (the solar zenith angle has been used to split the data). The local solar time of the AMSR2 overpass is around 13:30 ascending, meaning that the day-time signals correspond to measurements taken around that local solar time ($\pm$ 2 hours approximately) with the night-time signals corresponding to measurements taken at around 01:30 ($\pm$ 2 hours approximately). Whilst neither group of measurements are likely to represent the maxima or minima of the diurnal cycle (usually around 15:00 and 06:30 local time), it can be broadly assumed that the SKT increments in the day-time averages are most closely related to the diurnal cycle imposed through the SKT parameterization and those in the night-time averages are more closely linked to the input foundation SST products.

The SKT increments seen in the day-time observations, in general, are of higher magnitude and have a larger spatial extent. The key features relating to the eastern boundary currents and their equatorial extension are clearly seen at both day and night-time indicating that these are a deficiency in the input product (as described above) but also there is some issue with the representation of the diurnal cycle in these areas which is either to do with the SKT parameterization itself, or could be due to the parameterization having an incorrect starting point from the input SST product. The large scale TIW cooling seen in the ETP remains persistent between seasons, however, the cooling in the tropical Atlantic lessens and becomes wider spread in January when compared to July.

The large scale warming which has been attributed to CAOs and emissivity issues is very prominent in these monthly maps, showing in the NH for January and the SH in July. There is little difference in the SKT increments between the day and night-time observations in these areas, with the exception of the southwards extent in January, which gives further confidence that these increments are likely unrelated to the input SST product or the SKT parameterization. There are parts of this signal which could be real SKT increments which should be taken into account when addressing this problem, for example the Leeuwin current (west of Australia) in January night-time which is likely caused by errors in the input SST, however, there are also unexplained parts of the signal, for example that to the east of Australia (the east Australian current) in July at night.

The standard deviation of the SKT increments is shown for AMSR2 in Figure 30. It can be seen that the standard deviation of the SKT increments are large in the areas of the suspected CAO issue (NH for January, SH for July) in both the day-time and night-time observations (0.5 K compared with a global average of 0.32). In the NH, the standard deviation is large in the Pacific, however, in the Atlantic (where the example of CAOs is shown in Figure 14), the standard deviation appears to be an extension of the high variability associated with the Gulf Stream. The difference between the standard deviation of the SKT increments in the NH and SH could be due to the transitory nature of these CAO signals; these will be further investigated as part of additional later work to identify the areas affected by CAOs and screen them out.

As discussed in Section 2.2.3, significant RFI glint from geostationary satellites was affecting the signal over Europe in the background departures and without screening, this also impacted the SKT increments resulting in an artificial warming prior to the implementation of the RFI screening process (not shown). With the RFI screening implemented, Figure 29 over Europe shows warming SKT increments in January and cooling in July which is present for both AMSR2 and GMI (see later). As GMI was not impacted by the RFI glint (due to different orbit and sensor characteristics) it is clear that the SKT increments are no longer impacted by this erroneous signal. The difference between the seasons may be related to the diurnal cycle of the Mediterranean between seasons (see Pisano *et al.*, 2022, for further details), indicating that the SKT parameterization may require further attention in this area.

There are several signals in these maps which are not yet fully understood, but it is hoped these will become clearer when the SKT increments are used in the coupled DA system where the resultant SST can be compared to in-situ measurements. These include a cooling in January (day and night) and July (day) off the coast of Somalia close to the horn of Africa and a warming signal off the South East of Argentina (most prominent in the day-time in July). In both cases, these increments are close to areas of high standard deviation (see Figure 30). For the signal close to Somalia, this is in an area of strong upwelling events resulting in low SSTs (Mafimbo and Reason, 2010). For the signal near Argentina, it is also in a region where the uncertainty in the OSTIA product is high (Good *et al.*, 2020). In addition, there is a strong warming signal in July to the north of Australia (both during the day-time and night-time) for which there is currently no explanation but it is also associated with a slightly higher standard deviation than the surrounding areas.

The SKT increments generated for GMI are shown for the monthly averages split by day and night-time in Figure 31. Whilst the day/night split is achieved through use of the solar zenith angle (as is the case for AMSR2), unlike AMSR2 the observations here cannot be linked to specific times of the day; due to the inclined orbit of GMI, the observations will be from a range of times throughout the day. GMI does not host a 6.9v/h GHz channel, and instead the lowest frequency is 10.65v/h GHz. Whilst it was shown earlier (Section 3.2) that 6.9v GHz provides the best sensitivity to the surface, there is still significant information contained in the 10.65v GHz channel. In addition, due to the different orbits of AMSR2 and GMI (AMSR2 is in a polar orbit with a 13:30 ascending equatorial crossing time and GPM is in an 65°
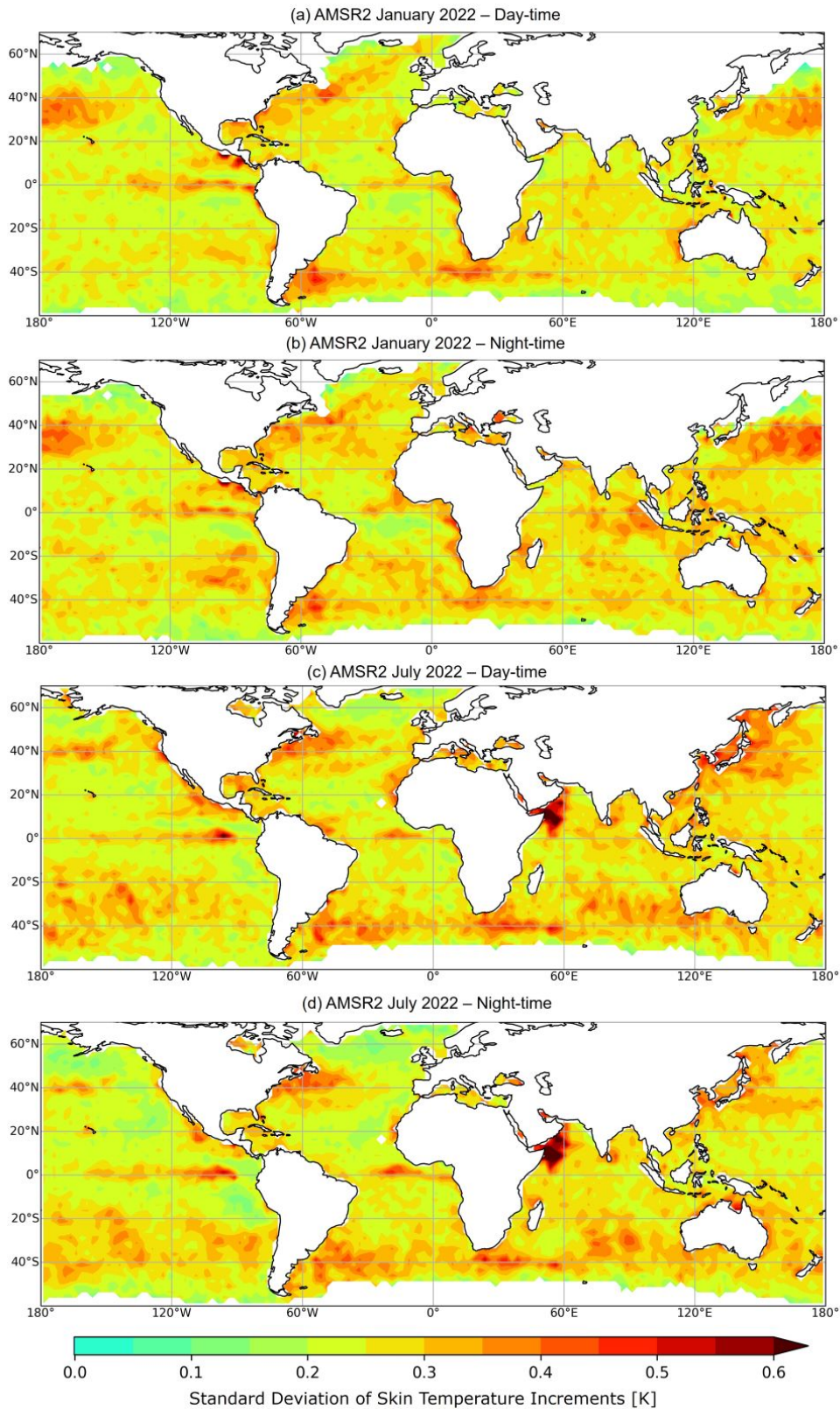
Figure 30: Monthly standard deviation of SKT increments for AMSR2 for (a) January 2022 day-time only observations, (b) January 2022 night-time only observations, (c) July 2022 day-time only observations and (d) July 2022 night-time only observations.
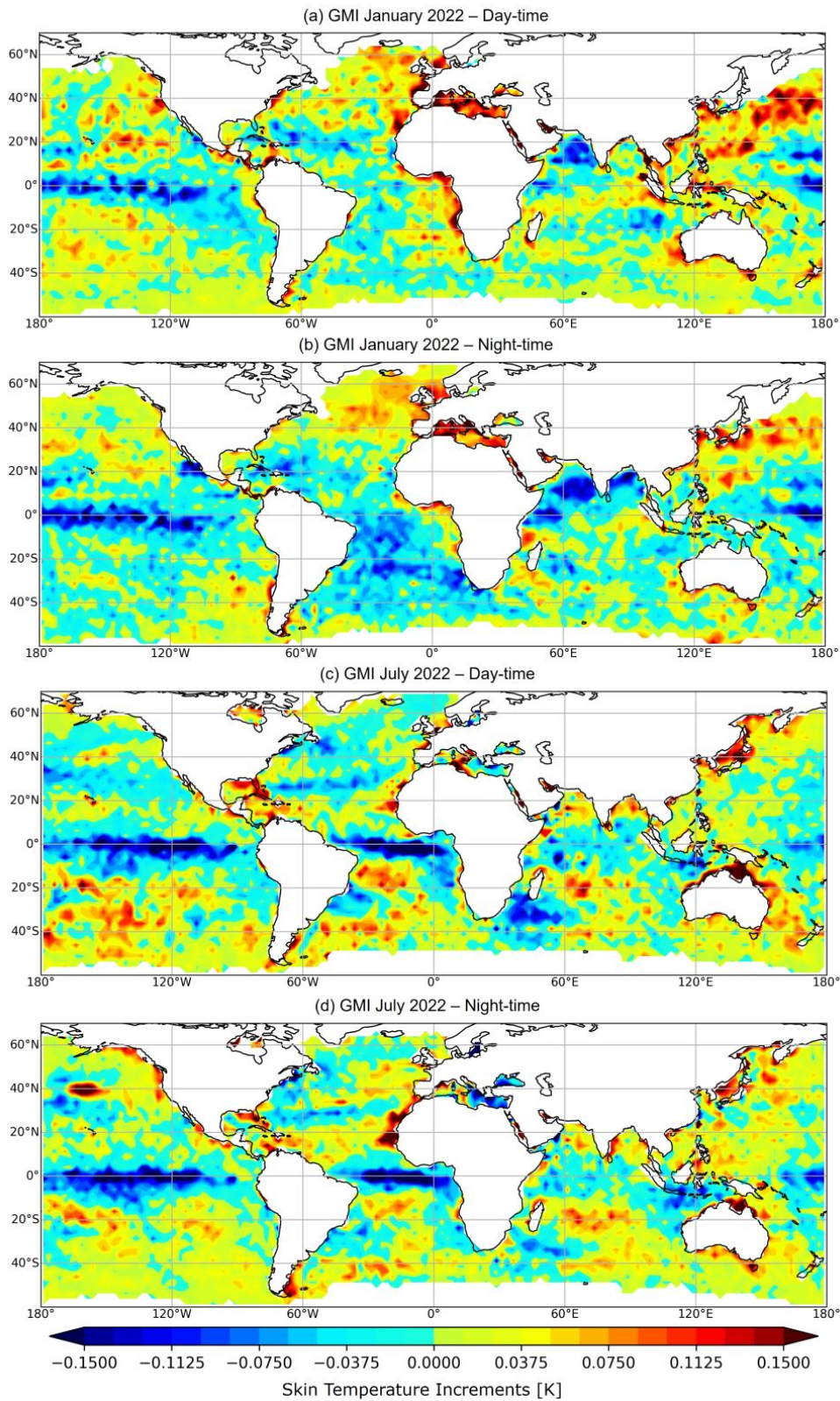
Figure 31: Monthly average of SKT increments for GMI for (a) January 2022 day-time only observations, (b) January 2022 night-time only observations, (c) July 2022 day-time only observations and (d) July 2022 night-time only observations.
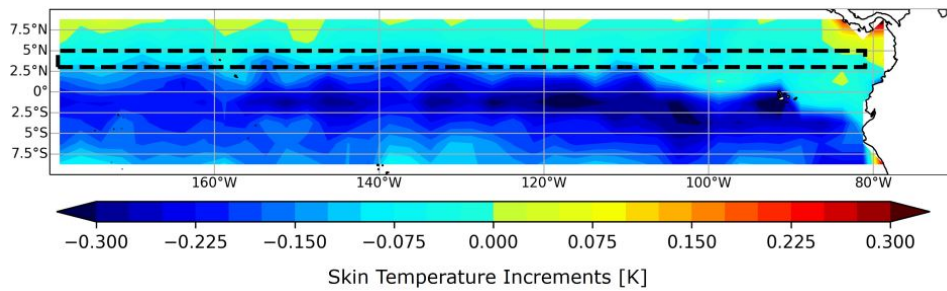
Figure 32: SKT increments for day-time from 2022-06-07 to 2022-08-31 from AMSR2, showing the area (black, dashed box) over which data is taken for Figures 33 and 34.

inclined orbit), GMI can sample a wider range of the diurnal cycle and therefore provides a wealth of information about the SKT increments which is not available from AMSR2.

In general, the patterns shown for GMI are very similar to those for AMSR2, albeit with a lower magnitude (note the maximum of the scale bar is half that shown for AMSR2). The key features discussed above for AMSR2 can be seen including the cooling the boundary currents, the impact of the suspected CAOs and emissivity issues, the cooling in the north Atlantic and the patterns in the Mediterranean. There are, however a couple of other features that are more prominent in the GMI SKT increments: a heating signal off the coast of west Africa particularly in July and a strong cooling in the Pacific off the coast of Baja California in the night-time observations in January.

It is also important to note the features which are not present in these mean SKT increment maps. Both the Gulf Stream and Tropical Warm Pool show no biases which accumulate over the long term. As the Gulf stream is an area of high variability, this is expected, and instead high standard deviations of SKT increments can be seen in the area across seasons, both day and night (see Figure 30). The tropical warm pool is an area of high annual SST with relatively calm winds but has the potential for very large diurnal warming events. Zhang *et al.* (2018) assessed several diurnal variation models in this area and determined that the Zeng and Beljaars (2005) model best captures the diurnal cycle under most conditions; as this is the model used at ECMWF in the SKT parameterization (ECMWF, 2023a), it may explain why little variation can be seen in this area.

3.4.3 Temporal Analysis

The Figures discussed thus far are either instantaneous (single cycle) maps or maps averaged over a period of a month. This section considers how the increments develop over the long term for specific features seen in these monthly maps (specifically for AMSR2 in Figure 29).

Firstly, we consider the development over time of the SKT increments in the region of the TIWs in the ETP. TIWs are waves of cool water with a wavelength of approximately 1000 km travelling west-wards at a speed of approximately 0.5 m/s (Tanaka and Hibiya, 2019). Figure 32 shows the area of these increments and the black dashed box shows the very top of these large scale waves which are examined further in Figures 33 and 34.

Figure 33 shows the (a) the initial SKT, (b) the final SKT and (c) the SKT increments for a box covering the northern most part of the TIWs in the ETP (from 180°W to 80°W longitude and 3°N to 5°N latitude shown in Figure 32) with the aim of highlighting the wave structure at the very top of these waves. It can be seen that the use of the SKT sink variable allows further structure to be added to these TIWs, with
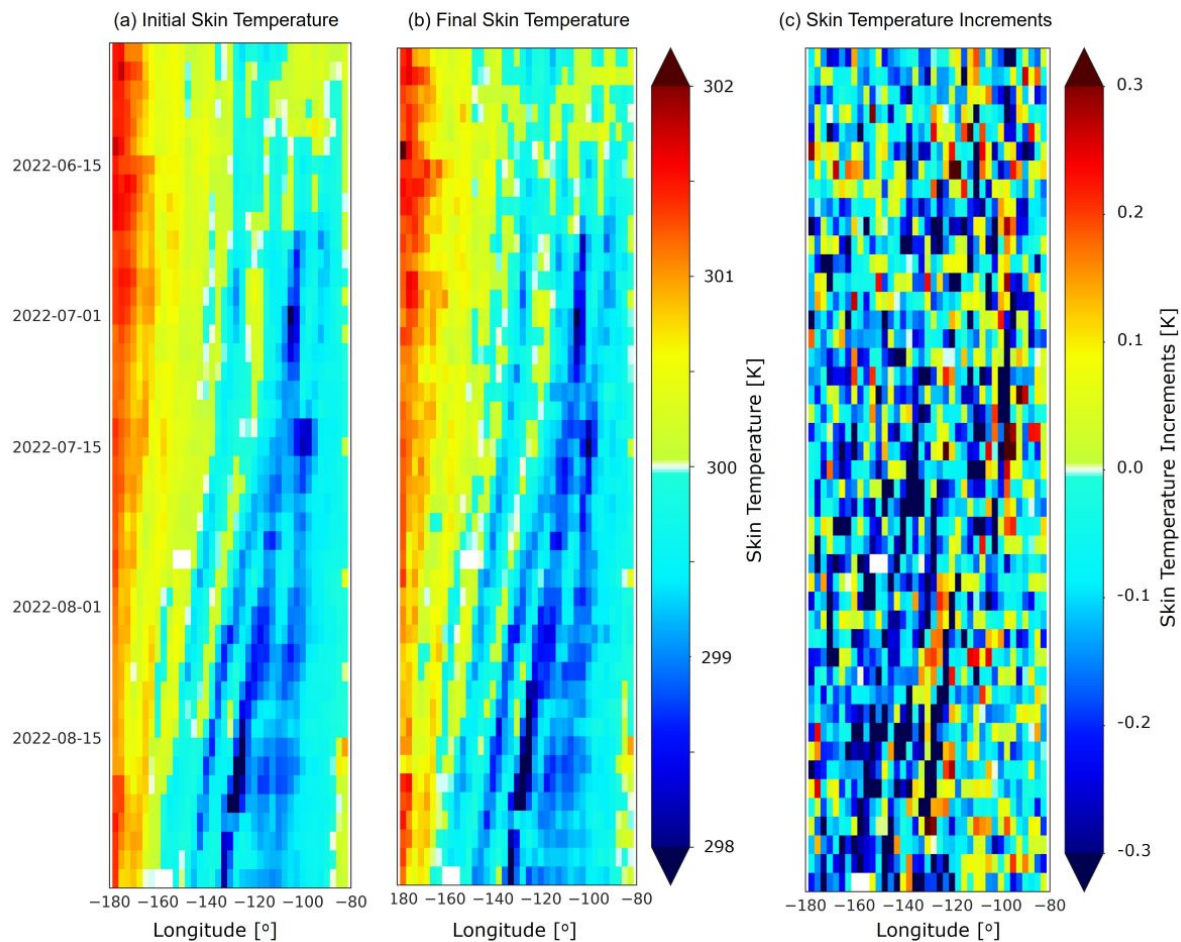
Figure 33: Development of (a and b) SKT features over time and (c) the associated SKT increments, averaged per longitude for the north-most part of the ETP region (to capture the very top of the waves, as shown in Figure 32) in the period 2022-06-07T00 to 2022-08-31T12 for day-time observations. The data is averaged on a 2.5° grid and per every 2 days (rather than per cycle). White areas denote missing data.

cooling occurring between the initial and final SKT. In particular, this feature can be seen between 2022-07-15 and 2022-08-05 (approximately). This figure also shows that these waves are travelling from east to west over time, as expected. Over the months, the peaks of these waves move further to the south-west, resulting in the very top of the peaks not being captured in the bounding box being considered.

Figure 34 shows the same data as Figure 33 except the longitudes of observations after the first cycle have been shifted to align the wave crest indicated by the red dashed line down the Figure. This "wave-centric" view of the data highlights how the positioning and the spread of the waves change over time. This Figure shows that the exposure of the background SKT to the observations results in a slight shift of the waves from east to west (the direction they are travelling in) which serves as evidence that the sink variable approach allows the SKT to be updated to the time of the observation (i.e. the aim of the sink variable approach).

To further support this, we can examine by how much individual wave tops are moving between the background and final SKT on a cycle-by-cycle basis; an example of this is shown in Figure 35 with the
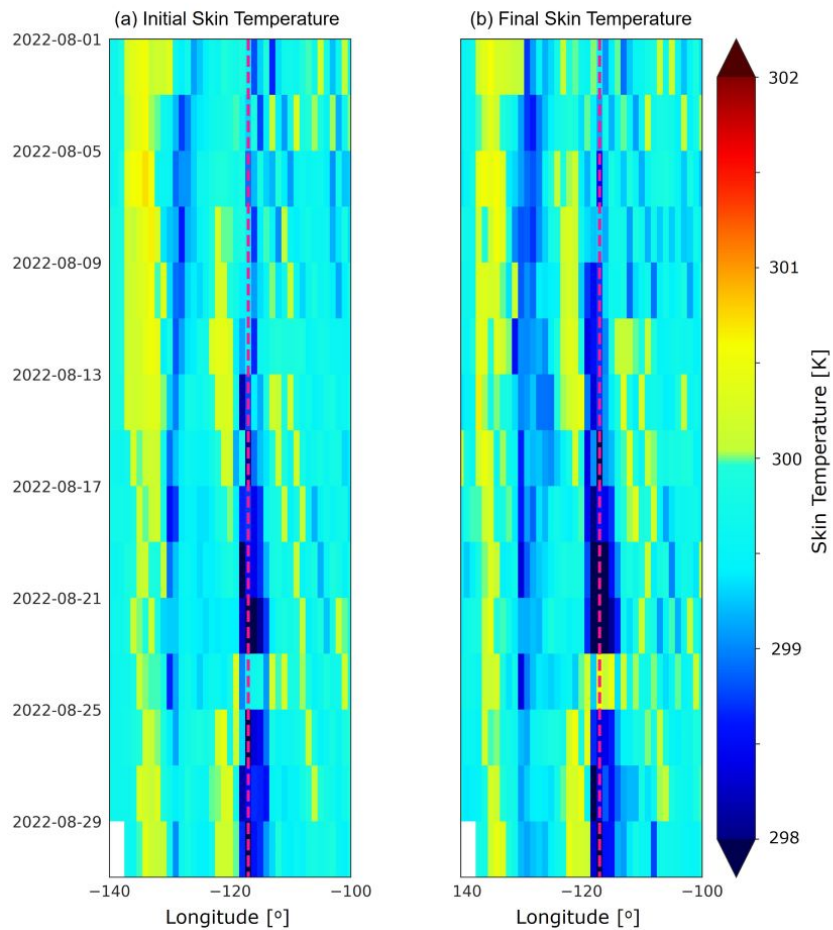
Figure 34: Development of SKT features over time, averaged per longitude for the north-most part of the Eastern Tropical Pacific Region in the period 2022-08-01T00 to 2022-08-31T12 for day-time observations. The data is averaged on a 1.0° grid and per every 2 days (rather than per cycle). The longitude of each observation is shifted after the first cycle to align one wave crest indicated by the red dashed line down the plot. White areas denote missing data.
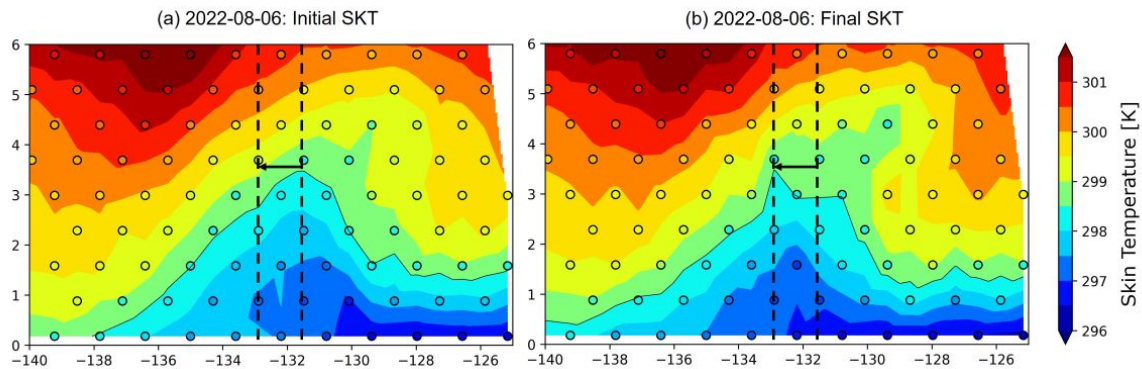
Figure 35: For a single cycle (2022-08-06T00) for AMSR2 the (a) initial and (b) final SKT from the sink variable process linearly interpolated in the specified area of the ETP with the observation SKT values shown in circles with a black outline. Marked in black dashed lines are the peak of the waves defined as the highest latitude of the 298.5 K contour line, showing the initial and final positions of this peak on both panels with an arrow indicating the direction of the shift of the wave.

movement in the wave top marked. Based on 12 dates where the movement is clear and measurable, the average longitudinal movement of these wave tops (defined as the highest latitude at which 298.5 K is present in this area in a continuous SKT field interpolated from the observations) is -0.75°. However, the result of this method varies significantly depending on which temperature contour is chosen. Therefore, to support this calculation, in Figure 36 we can see the movement between the initial and final SKT in the average temperature binned by longitude for the data shown in Figure 34 (i.e. a period of one month) where the crest of the wave is shifted in longitude to align over long periods i.e. the "wave-centric" view discussed above. From Figure 36, we can see that the average movement of the waves between the initial and final SKT is approximately -0.8°, in reasonable agreement with the method used for Figure 35.

The shift calculated from the previous two plots (Figures 35 and 36) are supported by the data shown in Figure 33, which shows a movement of the wave crest position of about 20° over 54 days, i.e. 0.37° / day (equivalently 0.48 m/s). This is highly consistent with the known speed of these waves at approximately 0.5 m/s (Tanaka and Hibiya, 2019). The shift of -0.75° or -0.8° would then be almost exactly consistent with a delay in the input SST of 2 days, similar to the typical latency of the SST products used in the generation of the SKT (21 h to 69 h, median time 45 h). This feature will be further examined within the coupled DA system where in-situ observations are available.

Further insight into the temporal variability of this feature would be gained through experimentation over a full year and when considering the case in the coupled DA system where further ocean parameters are available.

Secondly, we consider the temporal development of features in the tropical and sub-tropical Atlantic during JJA in the day-time and the north Atlantic DJF in the day-time. The areas of interest are shown outlined by a black dashed line in Figure 37.

Figure 38(a) shows the case of the sub-tropical cooling increments that are seen for AMSR2 during JJA day-time in Figure 29(c) (between 80°W and 10°W and 20°N and 40°N) as shown in Figure 37. The Figure shows that the feature moves northwards and southwards over time, with a higher intensity of increments in July (which is the case shown in Figure 29(c)) with the feature fading into August. As discussed above, it is unclear of the origin of this feature, although it is noted that the area in which it is present generally has a high salinity although it does not significantly vary over the course of one
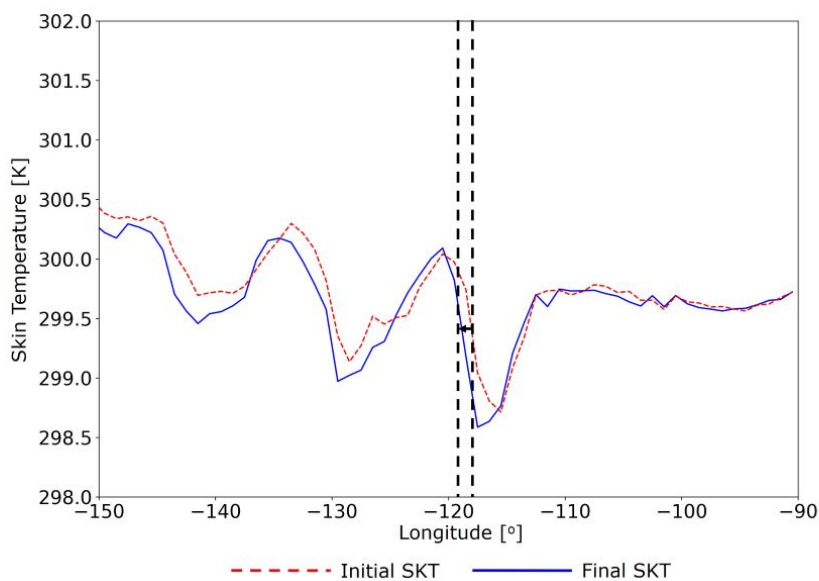
Figure 36: The average SKT at each longitude for the wave crests aligned in the "wave-centric" view shown in Figure 34 for all cycles between 2022-08-01T00 to 2022-08-31T12 for AMSR2 for the initial and final SKT.

year (for example, see the maps at NASA (2024a,b)). It is noted, however, that in the simulation of MW observations, a constant value of 35 Practical Salinity Unit (PSU) is used for sea surface salinity (Geer *et al.*, 2024). Further insight into the temporal variability of this feature would be gained through experimentation over a full year and when considering the case in the coupled DA system where further ocean parameters are available.

Figure 38(b) shows the case of the large positive departures in the north Atlantic in DJF day-time (see Figure 29(a) and 37) (between 60°W to 0° and 40°N to 75°N). This is the area which is discussed above as being impacted by the CAOs and a potential emissivity issue; this Figure further demonstrates that the CAOs have a significant impact on the area. A periodicity of around 4-6 days is evident in these features, which broadly fits with the origin of CAOs on the trailing edge of the surface low pressure systems of Rossby waves.

3.5 Impact on the Atmospheric Forecast System

As discussed in the methodology (Section 3.1), the sink variable approach allows the SKT to vary within one cycle, but this SKT is not passed to the next cycle and instead the background is reinitialised from the SST provided by external data sources and then converted to SKT. This means that we expect to see very little difference in both the fit to observations and the atmospheric forecast scores, especially considering that the SKT increments are only generated for two satellites. It is expected that the main impact of the SKT increments will be demonstrated once they are included into the coupled atmosphere-ocean system.

Figure 39 shows the difference in the RMSE between having the SKT sink variable active and a baseline of 6.9v and 10.65v GHz being active using the new observation errors (see Section 3.3.1) using own-analysis verification. This Figure shows that there is very little impact on the atmospheric forecast due to the introduction of the sink variable. As discussed in Section 2.5, there is also little impact from the inclusion of 6.9v and 10.65v GHz. When the two changes are combined (i.e. 6.9v and 10.65v GHz are

Figure 37: SKT increments for (a) the tropical and sub-tropical Atlantic between South America and Africa in the period 2022-06-07T00 to 2022-08-31T12 for day-time observations and (b) the north Atlantic between North America and Europe for the period 2021-12-07T00 and 2022-02-28T12 for day-time observations. Both are averaged on a 2.5° grid showing the area (black, dashed box) over which data is taken for Figure 38.
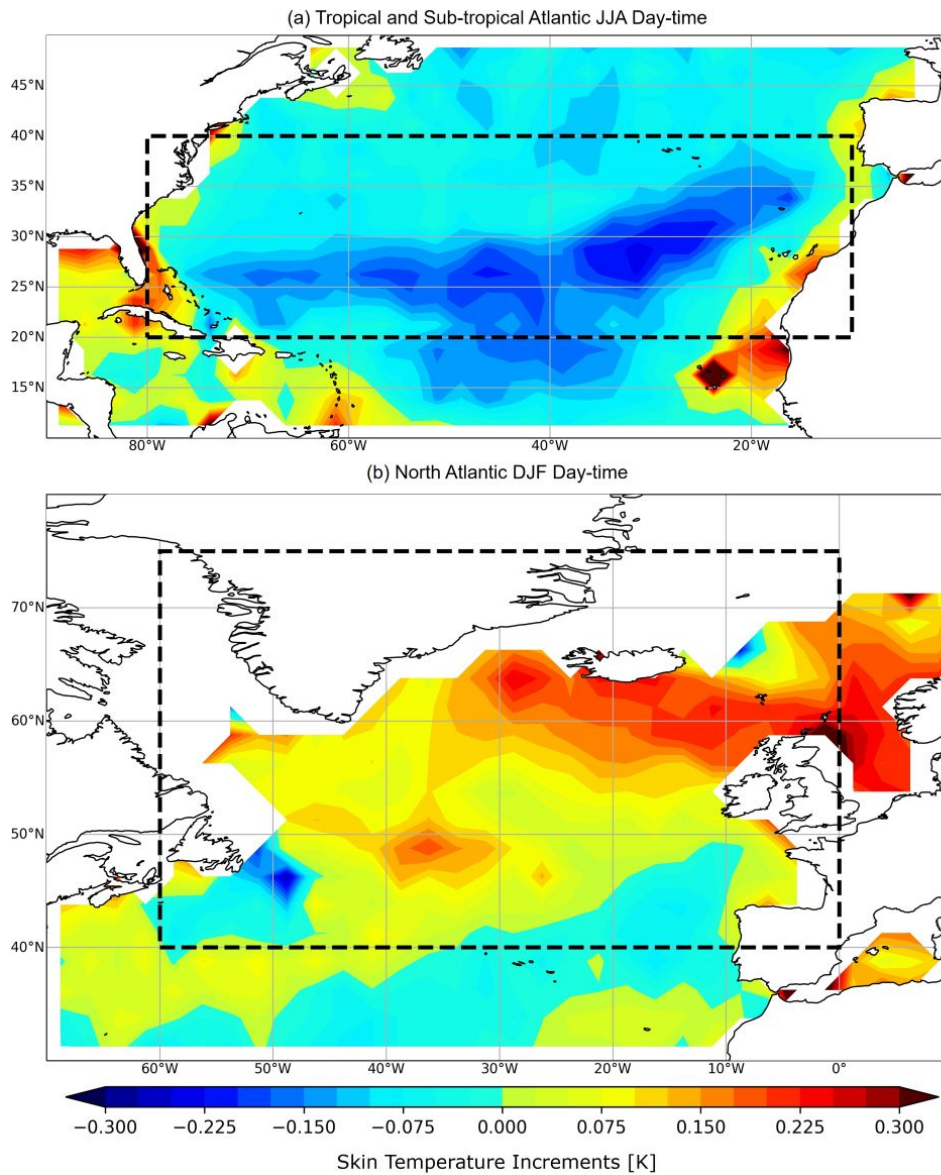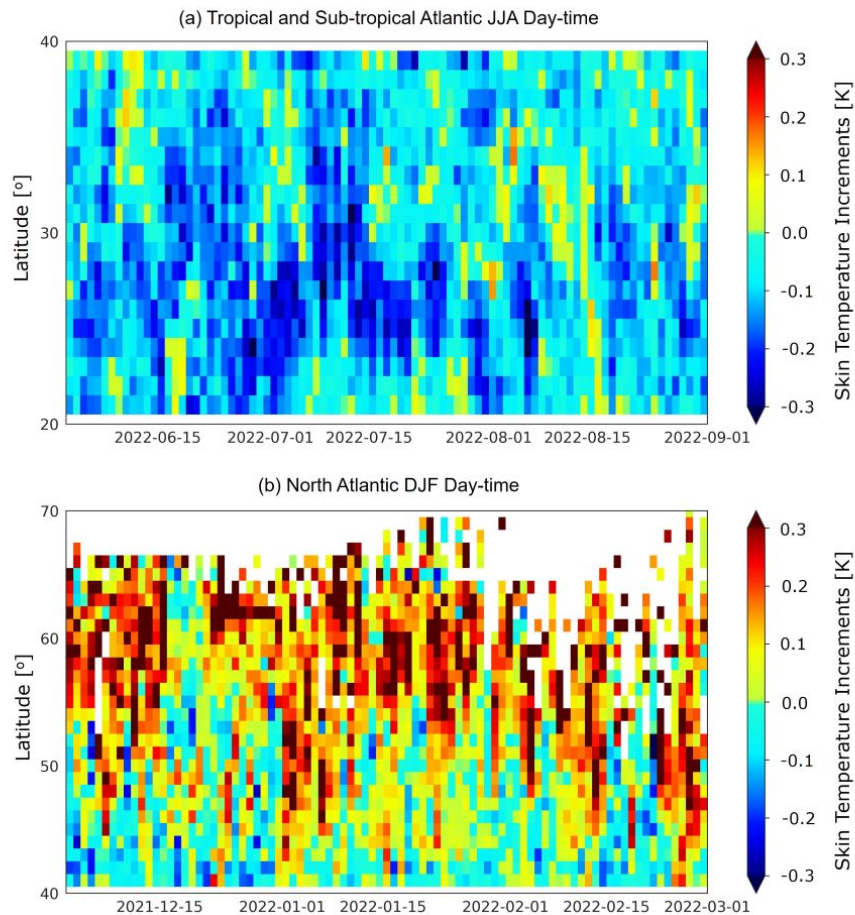
Figure 38: Development of SKT features over time, averaged per latitude for (a) the tropical and subtropical Atlantic between South America and Africa in the period 2022-06-07T00 to 2022-08-31T12 for day-time observations and (b) the north Atlantic between North America and Europe for the period 2021-12-07T00 and 2022-02-28T12 for day-time observations. Both are averaged on a 2.5° grid and per day (rather than per cycle). White areas denote missing data. Figure 37 shows the areas from which these data are taken.
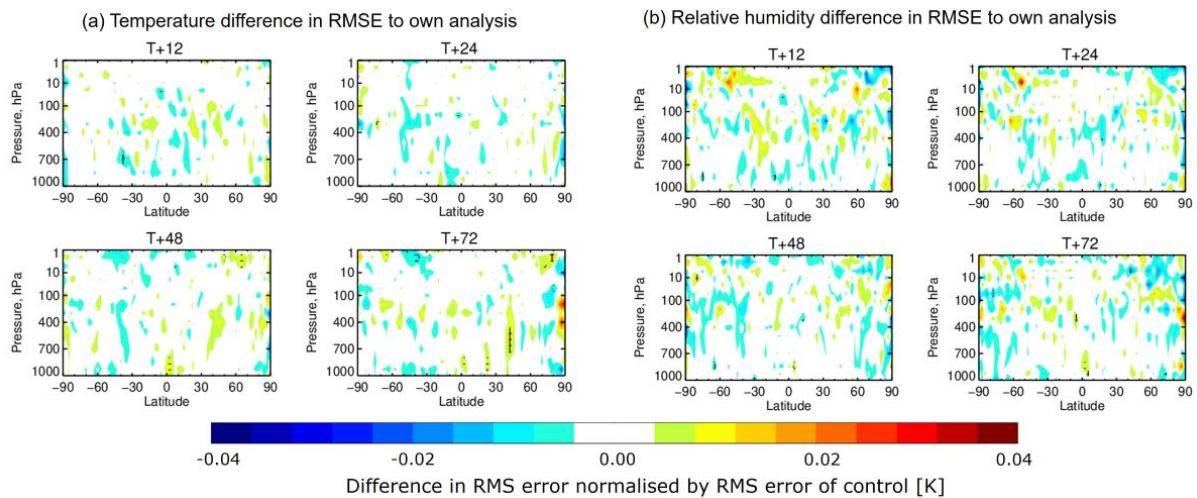
Figure 39: Normalised change in the RMSE of (a) temperature and (b) relative humidity at different forecast times (indicated) between the control experiment where the SKT sink variable is not active but 6.9v and 10.65v GHz are included with the new observation errors and the experiment where the SKT sink variable is turned on. The plots cover a two three month periods: 2021-12-07T00 to 2022-02-28T12 and 2022-07-07T00 to 2022-08-31T12. Own-analysis verification.

added and the SKT sink variable is switched on), a similar pattern as Figure 39 is seen for the temperature and relative humidity forecast scores (not shown). In addition, a similar change is seen in the relative humidity forecast field (shown in Figure 17) when the SKT sink variable is activated, which indicates that this is a real change and not linked to errors in the input SKT that are addressed through the sink variable.

However, although no significant impact on temperature and relative humidity are apparent from activating both 6.9v and 10.65v GHz, an impact on the surface (1000 hPa) winds can be seen from activating these channels when the new observation errors are used (even without the SKT sink variable active). Figure 40 shows this impact geographically for 4 forecast times for the NH summer (JJA) using own-analysis verification. There are large areas over the Pacific and to the east of Africa where the winds over oceans are consistently improved. In addition, statistically significant improvements are apparent in the standard deviation of the fit to wave height information from Jason-3 of 0.4% and an almost statistically significant improvement for Ku-band scatterometers in the tropics (not shown). This demonstrates that inclusion of these surface sensitive channels can have a positive impact on the surface information in the DA system when these new observation errors are included. However, it is noted that these improvements are only seen in the JJA months and there is a degradation in the same areas for the NH winter (DJF) experiments.

The changes when testing 6.9v and 10.65v GHz activation and SKT sink activation together broadly resemble the sum of the changes in the individual experiments (discussed here and in Section 2.5) with no other significant changes (either positive or negative) apparent. Therefore, the combined contribution is not discussed further.

It does not appear that information from the atmosphere has been aliased into the SKT sink variable. As discussed in Section 3.2, the inclusion of these strongly surface sensitive channels (6.9v GHz and 10.65v GHz) helps to constrain the SKT sink variable, which is further aided through the relatively tight observation errors assigned to these channels. The background departures in both cases (with /
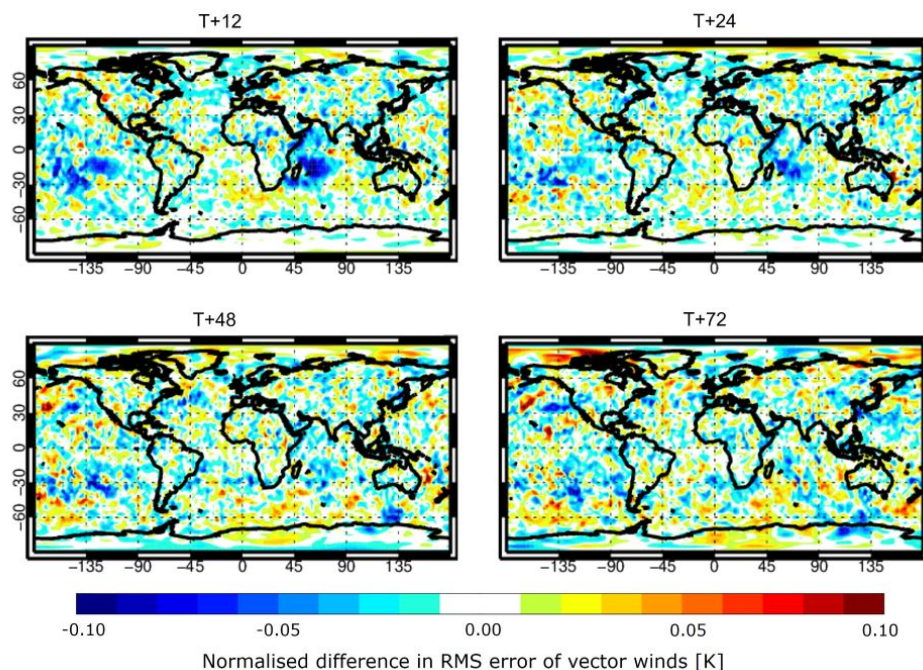
Figure 40: Normalised change in the RMSE of vector winds at the surface (1000 hPa) at different forecast times (indicated) between the control experiment where 6.9v and 10.65v GHz are not included and the experiment where the channels are included with the new observation errors used. The plots cover the period 2022-06-07T00 to 2022-08-31T12. Own-analysis verification.

without the sink variable active) strongly resemble the SKT increments, indicating that these channels are primarily sensitive directly to the surface and are detecting the errors in the input SKT. The only exception is the sensitivity to the CAO / emissivity issue regions discussed in Section 2.5 (particularly for the 10.65 GHz channel), which will be addressed in further work.

4 Conclusions

The aim of this work was to determine the impact of activating the SKT sink variable for MW imagers within the ECMWF-IFS. It was found that to achieve the most meaningful SKT increments, low frequency channels are required which are available on AMSR2 (6.9v and 10.65v GHz) and GMI (10.65v GHz).

The activation of these channels brought their own challenges and channel specific QC was needed. This included updating the coastline screening for the 6.9v GHz channels on AMSR2 to take into account the larger footprint of these channels, screening out sun-glint over oceans which has an impact at these lower frequencies and finally screening out areas over Europe which are affected by reflected RFI from geostationary satellites for the AMSR2 10.65v/h GHz channels. Further work will include assessing the impact of including h-polarised channels with these QC methods implemented.

The SKT sink variable was activated including these low frequency channels and it was found that the increments provide geophysically meaningful results, with the main indicator of this being significant cooling in the Tropical Instability Waves in the Eastern Tropical Pacific region. These are a known deficit

of the input OCEAN5 product and the SKT increments demonstrate that this is a persistent problem during the day and the night over the two seasons tested.

During this work, a few potential areas for improvement were identified. Firstly, and most significantly, areas adjacent to (and downwind) of Cold Air Outbreak (CAO) regions appear to be affected by a combination of these CAOs and potentially the use of incorrect emissivities for the 6.9v and 10.65v GHz channels. These errors propagate through to the SKT increments and therefore, we are now testing an enhanced screening for CAOs which will likely be part of the final package proposed for implementation in cycle 50r1.

In addition, there are some spatial patterns in the SKT increments for which there is currently no explanation. These patterns may be linked to diurnal cycles not being well captured, the validity of the SST at the time of use or possibly due to differences in salinity which are not currently accounted for in the RTTOV code. Studying a longer period may help to isolate the factors which cause these SKT increments.

Overall, the addition of the 6.9v and 10.65v GHz channels has resulted in a neutral impact on the atmospheric analysis and forecast (with small improvements in the fit to upper tropospheric humidity). On top of this, the SKT increments have also resulted in a neutral impact. However, it is intended to implement both of these changes in cycle 50r1 to support the future coupled atmosphere-ocean system.

The assimilation of SKT increments from MW imagers is already being tested in the coupled atmosphere-ocean system (described in McNally *et al.* (2022) and Browne *et al.* (2019)) and will be reported later. In the coupled DA system, the updated SKT values are passed to the 3D-var ocean DA system as SST observations. These, along with observations from in-situ sensors, are then used in the assimilation to find the best state of the ocean which is then provided in the next cycle to the atmospheric component of the system. In terms of the SKT increments, their use in the coupled DA system will allow further analysis beyond that presented here by, for example, allowing comparisons to in-situ SST measurements. This will give more information about the source of the SKT increments and allow a better understanding of the work presented in this report.

Acknowledgements

References

Alsweiss, S., Jelenak, Z. and Chang, P. (2017). Remote Sensing of Sea Surface Temperature using AMSR-2 measurements. *IEEE Journal of Selected Topics in Applied Earth Observations and Remote Sensing*, **PP**, 1–7, doi:10.1109/JSTARS.2017.2737470.

Bai, X., Qin, Z., Lin, Z. and Shen, W. (2022). Effect of Radio Frequency Interference-contaminated AMSR2 signal restoration on soil moisture retrieval. *Remote Sensing*, **14**(19), doi:10.3390/rs14194796, URL https://www.mdpi.com/2072-4292/14/19/4796.

Bauer, P., Lopez, P., Salmond, D. and Geer, A. (2006). Assimilation of cloud and precipitation affected microwave radiances. doi:10.21957/qwdhjxk64, URL https://www.ecmwf.int/node/7998.

Bormann, N., Geer, A. J. and Bauer, P. (2011). Estimates of observation-error characteristics in clear and cloudy regions for microwave imager radiances from Numerical Weather Prediction. *Quarterly Journal of the Royal Meteorological Society*, **137**(661), 2014–2023, doi:https://doi.org/10.1002/qj.833, URL https://rmets.onlinelibrary.wiley.com/doi/abs/10.1002/qj.833.

Browne, P. A., de Rosnay, P., Zuo, H., Bennett, A. and Dawson, A. (2019). Weakly coupled ocean–atmosphere data assimilation in the ECMWF NWP system. *Remote Sensing*, **11**(3), doi:10.3390/rs11030234, URL https://www.mdpi.com/2072-4292/11/3/234.

Bulgin, C. E., Merchant, C. J. and Ferreira, D. (2020). Tendencies, variability and persistence of Sea Surface Temperature anomalies. *Nature: Scientific Reports*, **10**(1), doi:https://doi.org/10.1038/s41598-020-64785-9.

CEOS (2020). Current and future Sea Surface Temperature missions: Towards 2050. URL www.ceos.org.

de Nijs, A. H. A., Parinussa, R. M., de Jeu, R. A. M., Schellekens, J. and Holmes, T. R. H. (2015). A methodology to determine Radio-Frequency Interference in AMSR2 observations. *IEEE Transactions on Geoscience and Remote Sensing*, **53**(9), 5148–5159, doi:10.1109/TGRS.2015.2417653.

de Rosnay, P., Browne, P., de Boisséson, E., Fairbairn, D., Hirahara, Y., Ochi, K., Schepers, D., Weston, P., Zuo, H., Alonso-Balmaseda, M., Balsamo, G., Bonavita, M., Borman, N., Brown, A., Chrust, M., Dahoui, M., Chiara, G., English, S., Geer, A., Healy, S., Hersbach, H., Laloyaux, P., Magnusson, L., Massart, S., McNally, A., Pappenberger, F. and Rabier, F. (2022). Coupled data assimilation at ECMWF: current status, challenges and future developments. *Quarterly Journal of the Royal Meteorological Society*, **148**(747), 2672–2702, doi:https://doi.org/10.1002/qj.4330, URL https://rmets.onlinelibrary.wiley.com/doi/abs/10.1002/qj.4330.

Dee, D. (2004). Variational bias correction of radiance data in the ECMWF system. In *ECMWF Workshop on Assimilation of high spectral resolution sounders in NWP, 28 June - 1 July 2004*, pp. 97–112, ECMWF, ECMWF, Shinfield Park, Reading, URL https://www.ecmwf.int/node/8930.

Deser, C., Alexander, M. A., Xie, S.-P. and Phillips, A. S. (2010). Sea surface temperature variability: Patterns and mechanisms. *Annual Review of Marine Science*, **2**(Volume 2, 2010), 115–143, doi:https://doi.org/10.1146/annurev-marine-120408-151453, URL https://www.annualreviews.org/content/journals/10.1146/annurev-marine-120408-151453.

Dinnat, E., English, S., Prigent, C., Kilic, L., Anguelova, M., Newman, S., Meissner, T., Boutin, J., Stoffelen, A., Yueh, S., Johnson, B., Weng, F. and Jimenez, C. (2023). PARMIO: A reference quality model for ocean surface emissivity and backscatter from the microwave to the infrared. *Bulletin of the American Meteorological Society*, **104**(4), E742 – E748, doi:https://doi.org/10.1175/BAMS-D-23-0023.1, URL https://journals.ametsoc.org/view/journals/bams/104/4/BAMS-D-23-0023.1.xml.

Donlon, C., Galeazzi, C., Midthassel, R., Sallusti, M., Triggianese, M., Fiorelli, B., De Paris, G., Kornienko, A. and Khlystova, I. (2023). The Copernicus Imaging Microwave Radiometer (CIMR): Mission overview and status. In *IGARSS 2023 - 2023 IEEE International Geoscience and Remote Sensing Symposium*, pp. 989–992, doi:10.1109/IGARSS52108.2023.10281934.

Donlon, C. J., Martin, M., Stark, J., Roberts-Jones, J., Fiedler, E. and Wimmer, W. (2012). The Operational Sea Surface Temperature and Sea Ice analysis (OSTIA) system. *Remote Sensing of Environment*, **116**, 140–158, doi:https://doi.org/10.1016/j.rse.2010.10.017, URL https://www.sciencedirect.com/science/article/pii/S0034425711002197, advanced Along Track Scanning Radiometer(AATSR) Special Issue.

Draper, D. and Newell, D. (2015). An assessment of Radio Frequency Interference using the GPM microwave imager. In *2015 IEEE International Geoscience and Remote Sensing Symposium (IGARSS)*, pp. 5170–5173, doi:10.1109/IGARSS.2015.7326998.

Draper, D. W. (2016). Terrestrial and space-based RFI observed by the GPM Microwave Imager (gmi) within NTIA semi-protected passive earth exploration bands at 10.65 and 18.7 ghz. In *2016 Radio Frequency Interference (RFI)*, pp. 26–30, doi:10.1109/{RFI}NT.2016.7833526.

Draper, D. W. and de Matthaeis, P. (2018). Radio Frequency Interference trends for the AMSR-E and AMSR2 radiometers. In *IGARSS 2018 - 2018 IEEE International Geoscience and Remote Sensing Symposium*, pp. 301–304, doi:10.1109/IGARSS.2018.8518061.

ECMWF (2019). The development of an in-house SST analysis. URL https://www.ecmwf.int/system/files/livelink/8563720/8_SST%20Analysis.pdf.

ECMWF (2021). *IFS Documentation CY47R3 - Part II: Data assimilation*. 2, ECMWF, doi:10.21957/t445u8kna, URL https://www.ecmwf.int/node/20196.

ECMWF (2023a). *IFS Documentation CY48R1 - Part IV: Physical Processes*. 4, ECMWF, doi:10.21957/02054f0fbf.

ECMWF (2023b). Model upgrade increases skill and unifies medium-range resolutions — ECMWF. https://www.ecmwf.int/en/about/media-centre/news/2023/model-upgrade-increases-skill-and-unifies-medium-range-resolutions, (Accessed on 01/11/2024).

English, S. J. (2008). The importance of accurate skin temperature in assimilating radiances from satellite sounding instruments. *IEEE Transactions on Geoscience and Remote Sensing*, **46**(2), 403–408, doi:10.1109/TGRS.2007.902413.

Geer, A., Ahlgrimm, M., Bechtold, P., Bonavita, M., Bormann, N., English, S., Fielding, M., Forbes, R., Hogan, R., Hólm, E., Janiskova, M., Lonitz, K., Lopez, P., Matricardi, M., Sandu, I. and Weston, P. (2017). Assimilating observations sensitive to cloud and precipitation. doi:10.21957/sz7cr1dym, URL https://www.ecmwf.int/node/17718.

Geer, A., Lupu, C., Duncan, D., Bormann, N. and English, S. (2024). SURFEM-ocean microwave surface emissivity evaluated. doi:10.21957/0af49d82e2, URL https://www.ecmwf.int/en/elibrary/81550-surfem-ocean-microwave-surface-emissivity-evaluated.

Geer, A. J. (2016). Significance of changes in medium-range forecast scores. *Tellus A: Dynamic Meteorology and Oceanography*, doi:10.3402/tellusa.v68.30229.

Geer, A. J. (2024a). Joint estimation of sea ice and atmospheric state from microwave imagers in operational weather forecasting. *Quarterly Journal of the Royal Meteorological Society*, doi:https://doi.org/10.1002/qj.4797, URL https://rmets.onlinelibrary.wiley.com/doi/abs/10.1002/qj.4797.

Geer, A. J. (2024b). Simultaneous inference of sea ice state and surface emissivity model using machine learning and data assimilation. *Journal of Advances in Modeling Earth Systems*, **16**(7), doi:https://doi.org/10.1029/2023MS004080, URL https://agupubs.onlinelibrary.wiley.com/doi/abs/10.1029/2023MS004080.

Geer, A. J. and Bauer, P. (2011). Observation errors in all-sky data assimilation. *Quarterly Journal of the Royal Meteorological Society*, **137**(661), 2024–2037, doi:https://doi.org/10.1002/qj.830, URL https://rmets.onlinelibrary.wiley.com/doi/abs/10.1002/qj.830.

Geer, A. J., Lonitz, K., Duncan, D. and Bormann, N. (2022). Improved surface treatment for all-sky microwave observations. *Technical Report 894*, ECMWF, doi:10.21957/zi7q6hau, URL https://www.ecmwf.int/en/elibrary/81296-improved-surface-treatment-all-sky-microwave-observations.

Gentemann, C. L., Meissner, T. and Wentz, F. J. (2010). Accuracy of satellite Sea Surface Temperatures at 7 and 11 ghz. *IEEE Transactions on Geoscience and Remote Sensing*, **48**(3), 1009–1018, doi:10.1109/TGRS.2009.2030322.

Good, S., Fiedler, E., Mao, C., Martin, M. J., Maycock, A., Reid, R., Roberts-Jones, J., Searle, T., Waters, J., While, J. and Worsfold, M. (2020). The current configuration of the OSTIA system for operational production of foundation sea surface temperature and ice concentration analyses. *Remote Sensing*, **12**(4), doi:10.3390/rs12040720, URL https://www.mdpi.com/2072-4292/12/4/720.

Ho, C., Slobin, S., Kantak, A. and Asmar, S. (2008). Solar brightness temperature and corresponding antenna nois temperature at microwave frequencies. *Technical report*, The Interplanetary Network, URL https://ipnpr.jpl.nasa.gov/progress_report/42-175/175E.pdf.

Kazumori, M., Geer, A. and English, S. (2014). Effects of all-sky assimilation of GCOM-W1/AMSR2 radiances in the ECMWF system. doi:10.21957/dnrgsorja, URL https://www.ecmwf.int/node/10425.

Kazumori, M., Geer, A. J. and English, S. J. (2016). Effects of all-sky assimilation of GCOM-W/AMSR2 radiances in the ECMWF Numerical Weather Prediction system. *Quarterly Journal of the Royal Meteorological Society*, **142**(695), 721–737, doi:https://doi.org/10.1002/qj.2669, URL https://rmets.onlinelibrary.wiley.com/doi/abs/10.1002/qj.2669.

Kilic, L., Prigent, C., Jimenez, C. and Donlon, C. (2021). Technical note: A sensitivity analysis from 1 to 40 GHz for observing the Arctic ocean with the Copernicus Imaging Microwave Radiometer. *Ocean Science*, **17**(2), 455–461, doi:10.5194/os-17-455-2021, URL https://os.copernicus.org/articles/17/455/2021/.

Kilic, L., Prigent, C., Jimenez, C., Turner, E., Hocking, J., English, S., Meissner, T. and Dinnat, E. (2023). Development of the SURface Fast Emissivity Model for ocean (SURFEM-ocean) based on the PARMIO radiative transfer model. *Earth and Space Science*, **10**(11), e2022EA002785, doi:https://doi.org/10.1029/2022EA002785, URL https://agupubs.onlinelibrary.wiley.com/doi/abs/10.1029/2022EA002785.

Kolstad, E. W., Bracegirdle, T. J. and Seierstad, I. A. (2009). Marine cold-air outbreaks in the north atlantic: temporal distribution and associations with large-scale atmospheric circulation. *Nature: Climate Dynamics*, **33**(2), 187–197, doi:https://doi.org/10.1007/s00382-008-0431-5.

Lawrence, H., Carminati, F., Bell, W., Bormann, N., Newman, S., Atkinson, N., Geer, A., Migliorini, S., Lu, Q. and Chen, K. (2017). An evaluation of FY-3C MWRI and assessment of the long-term quality of FY-3C MWHS-2 at ECMWF and the met office. doi:10.21957/lhuph6fb3, URL https://www.ecmwf.int/node/17206.

Le Vine, D. M. (2017). RFI and remote sensing of the earth from space. *Journal of Astronomical Instrumentation*, **08**(01), 1940001, doi:10.1142/S2251171719400014, URL https://doi.org/10.1142/S2251171719400014.

Lean, P., Geer, A. J. and Lonitz, K. (2017). Assimilation of Global Precipitation Mission (GPM) microwave imager (GMI) in all-sky conditions. *Technical Report 799*, ECMWF, doi:10.21957/8orc7sn33, URL https://www.ecmwf.int/node/17174.

Levy, R. C., Mattoo, S., Munchak, L. A., Remer, L. A., Sayer, A. M., Patadia, F. and Hsu, N. C. (2013). The collection 6 MODIS aerosol products over land and ocean. *Atmospheric Measurement Techniques*, **6**(11), 2989–3034, doi:10.5194/amt-6-2989-2013, URL https://amt.copernicus.org/articles/6/2989/2013/.

Li, Y., Dong, Q., Ren, Y., Kong, F. and Yin, Z. (2019). Effect of Sea Surface Temperature on sea surface brightness temperature measured by L-band microware radiometers. *IOP Conference Series: Earth and Environmental Science*, **310**(2), 022045, doi:10.1088/1755-1315/310/2/022045, URL https://dx.doi.org/10.1088/1755-1315/310/2/022045.

Lonitz, K. and Geer, A. (2015). *New screening of cold-air outbreak regions used in 4D-Var all-sky assimilation*. URL https://www.ecmwf.int/node/10777.

Maeda, T., Taniguchi, Y. and Imaoka, K. (2016). Gcom-w1 AMSR2 level 1R product: Dataset of brightness temperature modified using the antenna pattern matching technique. *IEEE Transactions on Geoscience and Remote Sensing*, **54**(2), 770–782, doi:10.1109/TGRS.2015.2465170.

Mafimbo, A. J. and Reason, C. J. C. (2010). Air-sea interaction over the upwelling region of the somali coast. *Journal of Geophysical Research: Oceans*, **115**(C1), doi:https://doi.org/10.1029/2009JC005439, URL https://agupubs.onlinelibrary.wiley.com/doi/abs/10.1029/2009JC005439.

Massart, S. (2023). Extended control variable (XCV): skin temperature background correction for the assimilation of clear-sky microwave radiances. doi:10.21957/4bbf1919d5.

Massart, S., Bormann, N., Bonavita, M. and Lupu, C. (2020). Skin temperature analysis for the assimilation of clear-sky satellite radiances. doi:10.21957/goe0ads8z, URL https://www.ecmwf.int/en/elibrary/81184-skin-temperature-analysis-assimilation-clear-sky-satellite-radiances.

Massart, S., Bormann, N., Bonavita, M. and Lupu, C. (2021). Multi-sensor analyses of the skin temperature for the assimilation of satellite radiances in the european centre for medium-range weather forecasts (ECMWF) integrated forecasting system (IFS, cycle 47r1). *Geoscientific Model Development*, **14**(9), 5467–5485, doi:10.5194/gmd-14-5467-2021, URL https://gmd.copernicus.org/articles/14/5467/2021/.

McNally, T., Browne, P., Chrust, M., Fairbairn, D., Massart, S., Mogensen, K. and Zuo, H. (2022). Progress on developing a new coupled sea-surface temperature analysis. URL https://www.ecmwf.int/en/newsletter/172/earth-system-science/progress-developing-new-coupled-sea-surface-temperature.

Meissner, T. and Wentz, F. J. (2012). The emissivity of the ocean surface between 6 and 90 GHz over a large range of wind speeds and earth incidence angles. *IEEE Transactions on Geoscience and Remote Sensing*, **50**(8), 3004–3026, doi:10.1109/TGRS.2011.2179662.

Minnett, P., Alvera-Azcárate, A., Chin, T., Corlett, G., Gentemann, C., Karagali, I., Li, X., Marsouin, A., Marullo, S., Maturi, E., Santoleri, R., Saux Picart, S., Steele, M. and Vazquez-Cuervo, J. (2019). Half a century of satellite remote sensing of sea-surface temperature. *Remote Sensing of Environment*, **233**, 111366, doi:https://doi.org/10.1016/j.rse.2019.111366, URL https://www.sciencedirect.com/science/article/pii/S0034425719303852.

Mogensen, K. and Balmaseda, W. (2012). The NEMOVAR ocean data assimilation system as implemented in the ECMWF ocean analysis for system 4. doi:10.21957/x5y9yrtm, URL https://www.ecmwf.int/node/11174.

Murata, H., Kazumori, M., Shibata, A., Seki, M., Imaoka, K. and Kachi, M. (2022). Use of satellite microwave observations in JMA global NWP system and some evidences of RFI in AMSR2 observation. In *A workshop to promote scientific use of spectrum under the URSI in collaboration with ECMWF*.

NASA (2024a). Aquarius maps: Sea surface salinity in the North Atlantic. https://salinity.oceansciences.org/aq-salinity-atlantic.htm, [Accessed 05-04-2024].

NASA (2024b). SMAP maps: RSS salinity. https://salinity.oceansciences.org/smap-salinity.htm, [Accessed 05-04-2024].

Nielsen-Englyst, P., Høyer, J. L., Alerskans, E., Pedersen, L. T. and Donlon, C. (2021). Impact of channel selection on SST retrievals from passive microwave observations. *Remote Sensing of Environment*, **254**, 112252, doi:https://doi.org/10.1016/j.rse.2020.112252, URL https://www.sciencedirect.com/science/article/pii/S0034425720306258.

NTIA (2016). National telecommunications and information administration: United states department of commerce. https://www.ntia.gov/sites/default/files/publications/january_2016_spectrum_wall_chart_0.pdf, [Accessed 11-01-2024].

Pearson, K., Merchant, C., Embury, O. and Donlon, C. (2018). The role of Advanced Microwave Scanning Radiometer 2 channels within an optimal estimation scheme for Sea Surface Temperature. *Remote Sensing*, **10**(1), doi:10.3390/rs10010090, URL https://www.mdpi.com/2072-4292/10/1/90.

Pisano, A., Ciani, D., Marullo, S., Santoleri, R. and Buongiorno Nardelli, B. (2022). A new operational mediterranean diurnal optimally interpolated Sea Surface Temperature product within the copernicus marine service. *Earth System Science Data*, **14**(9), 4111–4128, doi:10.5194/essd-14-4111-2022, URL https://essd.copernicus.org/articles/14/4111/2022/.

Roberts, C. D., Vitart, F. and Balmaseda, M. A. (2021). Hemispheric impact of north atlantic SSTs in subseasonal forecasts. *Geophysical Research Letters*, **48**(4), e2020GL0911446, doi:https://doi.org/10.1029/2020GL091446, URL https://agupubs.onlinelibrary.wiley.com/doi/abs/10.1029/2020GL091446, e2020GL0911446 2020GL091446.

SatBeams (2024). SatBeams. https://www.satbeams.com, [Accessed 26-01-2024].

SatExPat (2024). SatExPat. https://www.en.satexpat.com/sat, [Accessed 26-01-2024].

Scanlon, T., Geer, A. and Bormann, N. (2023). Microwave imagers in the ECMWF-IFS: Adding further observations and improving convective anvils in the observation operator. *Technical Report RR61*, ECMWF, doi:10.21957/8542a37c46.

Shen, W., Lin, Z., Qin, Z. and Bai, X. (2022). Improved estimation of O-B bias and standard deviation by an RFI restoration method for AMSR-2 C-band observations over north america. *Remote Sensing*, **14**(21), doi:10.3390/rs14215558, URL https://www.mdpi.com/2072-4292/14/21/5558.

Shibata, A. (2013). Descriptions of GCOM-W1 AMSR2 level 1R and level 2 algorithms — chapter 4: Sea Surface Temperature algorithm (NDX-120015A).

Tanaka, Y. and Hibiya, T. (2019). Generation mechanism of tropical instability waves in the equatorial pacific ocean. *Journal of Physical Oceanography*, **49**(11), 2901 – 2915, doi:10.1175/JPO-D-19-0094.1, URL https://journals.ametsoc.org/view/journals/phoc/49/11/jpo-d-19-0094.1.xml.

Wang, M. and Bailey, S. W. (2001). Correction of sun glint contamination on the SeaWiFS ocean and atmosphere products. *Appl. Opt.*, **40**(27), 4790–4798, doi:10.1364/AO.40.004790, URL https://opg.optica.org/ao/abstract.cfm?URI=ao-40-27-4790.

Wentz, F., Gentmeann, C. and Hilburn, K. (2005). Three years of ocean products from AMSR-E: evaluation and applications. In *Proceedings. 2005 IEEE International Geoscience and Remote Sensing Symposium, 2005. IGARSS '05.*, Vol. 7, pp. 4929–4932, doi:10.1109/IGARSS.2005.1526780.

Wentz, F. J., Gentemann, C., Smith, D. and Chelton, D. (2000). Satellite measurements of Sea Surface Temperature through clouds. *Science*, **288**(5467), 847–850, doi:10.1126/science.288.5467.847, URL https://www.science.org/doi/abs/10.1126/science.288.5467.847.

Wu, Y., Li, M., Bao, Y. and Petropoulos, G. P. (2020). Cross-validation of Radio-Frequency-Interference signature in satellite microwave radiometer observations over the ocean. *Remote Sensing*, **12**(20), doi:10.3390/rs12203433, URL https://www.mdpi.com/2072-4292/12/20/3433.

Wu, Y., Qian, B., Bao, Y., Li, M., Petropoulos, G., Liu, X. and Li, L. (2019). Detection and analysis of C-band Radio Frequency Interference in AMSR2 data over land. *Remote Sensing*, **11**, 1228, doi:10.3390/rs11101228.

Xue, Q. and Guan, L. (2019). Identification of sun glint contamination in GMI measurements over the global ocean. *IEEE Transactions on Geoscience and Remote Sensing*, **57**(9), 6473–6483, doi:10.1109/TGRS.2019.2906380.

Yang, C., Liu, Z., Bresch, J., Rizvi, S., Huang, X.-Y. and Min, J. (2016). AMSR2 all-sky radiance assimilation and its impact on the analysis and forecast of hurricane sandy with a limited-area data assimilation system. *Tellus A: Dynamic Meteorology and Oceanography*, **68**(1), 30917, doi:10.3402/tellusa.v68.30917, URL https://doi.org/10.3402/tellusa.v68.30917.

Zabolotskikh, E. V., Mitnik, L. M. and Chapron, B. (2015). Radio-Frequency Interference identification over oceans for C- and X-band AMSR2 channels. *IEEE Geoscience and Remote Sensing Letters*, **12**(8), 1705–1709, doi:10.1109/LGRS.2015.2420120.

Zeng, X. and Beljaars, A. (2005). A prognostic scheme of sea surface skin temperature for modeling and data assimilation. *Geophysical Research Letters*, **32**(14), doi:https://doi.org/10.1029/2005GL023030, URL https://agupubs.onlinelibrary.wiley.com/doi/abs/10.1029/2005GL023030.

Zhang, H., Beggs, H., Merchant, C. J., Wang, X. H., Majewski, L., Kiss, A. E., Rodríguez, J., Thorpe, L., Gentemann, C. and Brunke, M. (2018). Comparison of SST diurnal variation models over the tropical warm pool region. *Journal of Geophysical Research: Oceans*, **123**(5), 3467–3488, doi:https://doi.org/10.1029/2017JC013517, URL https://agupubs.onlinelibrary.wiley.com/doi/abs/10.1029/2017JC013517.

Zuo, H., Balmaseda, M. A., Tietsche, S., Mogensen, K. and Mayer, M. (2019). The ECMWF operational ensemble reanalysis–analysis system for ocean and sea ice: a description of the system and assessment. *Ocean Science*, **15**(3), 779–808, doi:10.5194/os-15-779-2019, URL https://os.copernicus.org/articles/15/779/2019/.